

UNIVERSITÉ DE GENÈVE  
Section de Physique  
Département de Physique Nucléaire  
et Corpusculaire

FACULTÉ DES SCIENCES

Professeur Martin Pohl

---

# Measurement of the Cosmic Ray Helium Flux with the AMS-02 Experiment

THÈSE

présentée à la Faculté des Sciences de l'Université de Genève  
pour obtenir le grade de Docteur ès Sciences, mention Physique

par

**Marion Habiby Alaoui**  
de  
Chalon Sur Saône (France)

Thèse N°4912

GENÈVE  
Atelier d'impression ReproMail  
2016



**UNIVERSITÉ  
DE GENÈVE**

FACULTÉ DES SCIENCES

**Doctorat ès sciences  
Mention physique**

Thèse de *Madame Marion HABIBY ALAOU*

intitulée :

**"Measurement of the Cosmic Ray Helium Flux with the AMS-02  
Experiment"**

La Faculté des sciences, sur le préavis de Monsieur M.POHL, professeur ordinaire et directeur de thèse (Département de physique nucléaire et corpusculaire), de Monsieur X.WU, professeur associé (Département de physique nucléaire et corpusculaire) et de Madame B. BERTUCCI, professeure (Università degli Studi di Perugia, Dipartimento di Fisica e Geologia, Perugia, Italia) autorise l'impression de la présente thèse, sans exprimer d'opinion sur les propositions qui y sont énoncées.

Genève, le 21 mars 2016

Thèse - 4912 -

**Le Doyen**

N.B. - La thèse doit porter la déclaration précédente et remplir les conditions énumérées dans les "Informations relatives aux thèses de doctorat à l'Université de Genève".



# RÉSUMÉ DE THÈSE

C'est il y a plus de 100 ans que l'existence des rayons cosmiques a été postulée et depuis, notre connaissance à leur sujet n'a pas cessé de s'accroître et ce de façon exponentielle. Les technologies de détection des particules ont également considérablement évoluées permettant de construire des détecteurs très performants. De nos jours, qu'elles soient localisées sur terre ou dans l'espace, de nombreuses expériences enregistrent des données sur les rayons cosmiques au quotidien nous permettant d'en apprendre toujours plus sur ces particules venant de notre système solaire, de notre galaxie voire même de plus loin. Le spectre des rayons cosmiques s'étend de quelques MeV à des énergies extrêmes pouvant atteindre  $10^{20}$  eV. Les différents types de détecteurs existants à l'heure actuelle nous permettent de le parcourir d'un bout à l'autre.

L'expérience AMS-02, pour *Alpha-Magnetic Spectrometer*, fait parti des détecteurs de très haute qualité qui ont été construits ces dernières années. AMS-02 a été installé sur la Station Spatiale Internationale en mai 2011 et ne cesse d'enregistrer des données depuis. Un tel volume de données nous permet de produire des spectres pour les rayons cosmiques avec une précision jamais atteinte auparavant. Après avoir publié de nombreux résultats sur les électrons, les positrons, les protons et l'hélium récemment, l'utilité d'un tel détecteur ne peut être mise en doute. Avec une telle précision dans ces résultats, AMS-02 peut se concentrer sur les sujets les plus intéressants à l'heure actuelle tel que la recherche de la matière noire à travers l'étude de l'excès de positrons, la recherche de l'antimatière grâce à la détection de l'antihélium, et également permettre de contraindre les modèles de propagation des rayons cosmiques grâce aux rapports de flux entre rayons cosmiques primaires et secondaires.

Le travail réalisé pour cette thèse se focalise sur le spectre d'hélium. L'hélium est le second élément le plus abondant dans les rayons cosmiques, juste après les protons, ce qui nous permet d'être dans de bonnes conditions pour aborder la recherche d'antimatière. En effet, avec un laps de temps suffisamment grand de prise de données il nous est possible, dans un premier temps, de produire un spectre pour l'hélium ayant une précision jamais atteinte précédemment et dans un second temps, d'avoir suffisamment de statistique pour chercher des noyaux d'antihélium et repousser la limite sur le rapport antihélium/hélium.

Le but principal de cette thèse est le calcul du flux d'hélium. Premièrement, nous avons calculé ce flux pour la même quantité de données que celle utilisée pour le résultat publié par la collaboration il y a quelques mois. Ces données représentent 30 mois de détection d'événements par le détecteur que nous avons analysé pour en extraire le nombre de noyaux d'hélium détectés. Nous avons par la suite étudié les différentes composantes nous permettant de calculer le flux tel que le temps d'exposition, l'acceptance effective, les efficacités et les erreurs statistiques et systématiques. La différence entre les deux résultats n'excède pas 2.5% sur tout l'intervalle de rigidité et est parfaitement compatible avec les erreurs systématiques, validant ainsi notre analyse. Dans un second temps, nous avons augmenté le volume de données et ajouté 19 mois supplémentaires. Après avoir calculé le nouveau flux sur les

données étendues nous l'avons comparé au flux publié. Encore une fois, la compatibilité entre les deux flux est très bonne, n'excédant pas 3% au-dessus de 10GV. La différence entre les résultats au-dessous de 10GV, augmentant lorsque la rigidité diminue, est expliquée par les effets de modulations solaires. Nous pouvons déduire de ces résultats que ce n'est pas en augmentant le volume de données que nous réussirons à améliorer le résultat pour le flux d'hélium, mais en réduisant les erreurs systématiques. La seconde partie de ce travail présente une recherche préliminaire de noyaux d'antihélium. Nous avons pu retenir 2 candidats après une simple analyse ce qui nous a permis d'obtenir une limite supérieure pour le rapport antihélium/hélium à  $2.21 \cdot 10^{-7}$  à 95%C.L. pour un intervalle de rigidité allant de 1.7GV à 200GV. Ce résultat améliore celui précédemment obtenu par l'expérience PAMELA permettant ainsi de repousser la limite de ce rapport.

# REMERCIEMENTS

Je voudrais remercier dans un premier temps mon directeur de thèse Pr. Martin Pohl pour m'avoir donné l'opportunité d'étudier un sujet fascinant et de faire parti du groupe AMS de l'Université de Genève. Je voudrais remercier les personnes composants ce groupe et tout particulièrement Pierre Saouter qui m'a aidé depuis le premier jour. Je remercie également Mercedes Paniccia pour ses conseils avisés et Divic Rapin pour ces discussions toujours intéressantes. J'aimerais également remercier toute la collaboration AMS ainsi que mon jury les professeurs Bruna Bertucci et Xin Wu. Pour finir je tiens à remercier tout particulièrement ma mère, mon père et mes frères pour leur soutien, en particulier ces quatre dernières années.



# Contents

<b>RÉSUMÉ DE THÈSE</b>	<b>i</b>
<b>REMERCIEMENTS</b>	<b>iii</b>
<b>INTRODUCTION</b>	<b>1</b>
<b>1 COSMIC RAYS</b>	<b>3</b>
1.1 The Cosmic Rays . . . . .	3
1.1.1 Discovery of Cosmic Rays . . . . .	4
1.1.2 The Energy Spectrum . . . . .	5
1.1.3 Elemental Composition of the GCRs . . . . .	8
1.1.4 Acceleration and Propagation . . . . .	10
1.2 Cosmic Ray Detection . . . . .	11
1.2.1 Direct Detection . . . . .	11
1.2.2 Ground Based Detection . . . . .	14
1.3 Space Based Experiments . . . . .	16
1.3.1 Detectors . . . . .	17
1.3.2 Spatial Environment . . . . .	19
<b>2 THE AMS-02 EXPERIMENT</b>	<b>23</b>
2.1 AMS-02 on the ISS . . . . .	23
2.1.1 Operation in Space . . . . .	25
2.1.2 Data Transmission . . . . .	25
2.2 AMS-02 Subdetectors . . . . .	25
2.2.1 Transition Radiation Detector . . . . .	27
2.2.2 Time of Flight . . . . .	28
2.2.3 Silicon Tracker . . . . .	29
2.2.4 Anti-Coincidence Counters . . . . .	33
2.2.5 Ring Imaging Čerenkov Counter . . . . .	34
2.2.6 Electromagnetic Calorimeter . . . . .	36
2.3 Data Taking . . . . .	36
2.3.1 Trigger . . . . .	37
2.3.2 Data Acquisition System . . . . .	37
2.4 Monte Carlo Simulations . . . . .	38

<b>3</b>	<b>HELIUM ANALYSIS</b>	<b>39</b>
3.1	Sample Selection . . . . .	39
3.1.1	Data Set . . . . .	40
3.1.2	Pre-selection . . . . .	40
3.1.3	ToF Selection . . . . .	40
3.1.4	Tracker Selection . . . . .	42
3.1.5	Charge Selection . . . . .	45
3.2	Exposure Time . . . . .	48
3.3	Efficiencies . . . . .	49
3.3.1	Trigger Efficiency . . . . .	50
3.3.2	ToF Efficiency . . . . .	51
3.3.3	Inner Tracker Efficiency . . . . .	51
3.3.4	External Layers Efficiencies . . . . .	54
3.4	Survival Probability . . . . .	56
3.5	Acceptance . . . . .	60
3.5.1	Geometrical Acceptance . . . . .	61
3.5.2	Folded and Unfolded Acceptances . . . . .	61
3.6	Unfolding Procedure . . . . .	64
3.7	Systematic Errors . . . . .	70
3.7.1	Trigger Efficiency Errors . . . . .	71
3.7.2	Acceptance Errors . . . . .	71
3.7.3	Unfolding Errors . . . . .	73
3.7.4	Rigidity Scale Errors . . . . .	73
3.7.5	Survival Probability Errors . . . . .	74
<b>4</b>	<b>RESULTS ON THE HELIUM FLUX</b>	<b>77</b>
4.1	First Results . . . . .	77
4.1.1	Flux Calculation . . . . .	77
4.1.2	Flux results . . . . .	78
4.2	Comparison with the Collaboration results . . . . .	80
4.3	Extended Analysis and Final Results . . . . .	83
4.3.1	Analysis . . . . .	83
4.3.2	Comparison with the published results . . . . .	87
4.3.3	Interpretation . . . . .	87
<b>5</b>	<b>A FIRST LOOK AT ANTIHELIUM</b>	<b>91</b>
5.1	Status of the Antihelium Search . . . . .	91
5.2	Antihelium Analysis . . . . .	93
5.2.1	Inverse Rigidity Study . . . . .	93
5.2.2	Track Quality Check . . . . .	94
5.2.3	ToF $\beta$ check . . . . .	98
5.3	Antihelium Results . . . . .	101
	<b>CONCLUSION</b>	<b>107</b>

# INTRODUCTION

Cosmic rays have been discovered more than a hundred years ago. Since the first hint of the existence of cosmic radiation up to now, our knowledge about cosmic rays has grown exponentially. At the same time the detection technologies have considerably improved leading us to very high performance detectors. From ground-based to space-based detectors, a lot of experiments are taking data nowadays in order to improve our knowledge about cosmic rays. These different kind of experiments allow to detect the entire spectrum of cosmic rays that goes from few MeV up to extremely high energies around  $10^{20}$  eV where few events have been detected.

The Alpha-Magnetic Spectrometer AMS-02 counts among the high quality detectors and has already proven its usefulness for the past two years publishing significantly improved results on the electron, positron, proton and helium spectra. AMS-02 is taking data since May 2011, which represents a significant amount of statistic allowing the computation of spectra with an precision never reached by any other experiment. Such a precision in the measurements will allow AMS-02 to focus on interesting topics such as the search of dark matter through antimatter excess studies, the search of antimatter through antinuclei detection, and constraining propagation models of cosmic rays through the study of primaries versus secondaries nuclei ratios.

This work focuses on helium spectrum. First of all, helium is the second most abundant nucleus in cosmic rays which opens an interesting path to the antimatter search. Indeed, with a sufficient time range for the data taking we can on one hand produce a spectrum with a precision never obtained in the past, and on the other hand, we can have sufficient statistics to search for antihelium and improve the limit on the antihelium/helium ratio.

The main purpose of this work is to compute the helium flux. First of all, the calculation of the flux is made for the same data set, i.e. time range, than the one used for the publication [1]. This data set contains the first 30 months of data taking. The second step consists in extending this data set by adding the 19 following months. By extending the data set we are able to see the impact of an increase in the statistic on the result. We compare these two results to the publication result. Finally, we take a first look at the antihelium study and find a preliminary upper limit for the antihelium over helium ratio.

This thesis is divided into five Chapters. The first two are an introduction to cosmic rays and the AMS-02 detector. The last three Chapters are dedicated to the analysis performed for this work. The first Chapter introduces cosmic rays. The first part recounts the story of the discovery of cosmic rays and the following discoveries that lead us to the knowledge we have today. Then, we introduce two important measurements, the energy spectrum and the elemental composition. An overview of the acceleration and the propagation of the cosmic rays follows. After that, we introduce the detection of the cosmic ray particles and the different methods that exist and are used when building a cosmic ray

detector with some examples of existing detectors. Finally, we focus on the space-based experiments giving some examples and describing the spatial environment.

The second Chapter focuses on the AMS-02 detector. First, we describe the different aspects of the operation of AMS-02 on the International Space Station (ISS). Then, we give more details on the six subdetectors that compose AMS-02, highlighting the fact that each one of them gives valuable information on the particles that cross the detector through different detection processes. Such a diversity and redundancies constitute the strength of this experiment. At the end of the Chapter, we introduce the data taking process.

The third Chapter gives the details of the analysis for this work. First, by defining precisely the different steps of the selection of helium nuclei. Then, the different terms used to compute the flux are detailed one by one. We start with the exposure time. We introduce the efficiencies according to our selection process. Then, the acceptance computation is detailed as well as the unfolding procedure, which is an important step in the case of a power law spectrum. Finally, we give an overview of the sources of systematic errors.

The fourth Chapter introduces the results. First, the result for the same data set then the publication is given. After that, we extend the data set and give the new result for the helium spectrum. For these two steps, the analysis process remains identical. Both of the results are compared to the published spectrum.

The last Chapter is dedicated to a first look at antihelium. We describe the simple analysis used to search for antihelium and explain the different steps followed. Interpreting conservatively the few selected candidates as potentially due to background, we give a limit on the antihelium over helium ratio.



# Chapter 1

## COSMIC RAYS

The cosmic ray study is a vast domain that brings together two fields of expertise in physics: astrophysics and particle physics. Cosmic rays are streams of photons, electrons, positrons and fully ionized nuclei of high energy that travel through the galaxy toward Earth where they are detected. From their discovery in the early 1900's until the present days, the knowledge about the cosmic rays have been expanding very fast and the more we learn about them the more we expand the field. The subject of this thesis being the helium spectrum, we will focus in this Chapter only on the charged cosmic rays. Indeed, among the cosmic rays we detect also photons and neutrinos, their studies are different from the studies of charges particles because of their different type of interactions. They constitute a fascinating field of astroparticles but will not be mentioned here.

The first Section of this Chapter is dedicated to general knowledge about the cosmic rays. We will start with a quick historic. Then we will introduce the cosmic ray energy spectrum that provide important information about the cosmic rays. The abundance of the elements in the detected nuclei will be tackled since it brings also important knowledge about the interactions of cosmic rays with the interstellar medium among other things. Finally, the acceleration and propagation of cosmic rays will be briefly mentioned. The second Section will be an overview of the different principles that exist for the detection of cosmic rays. First we will discuss about the direct detections. Then we will focus on the indirect detections with ground based experiments that allow to measure particles of very high energy by their interactions with the atmosphere. The third Section will be dedicated to space-based experiments. We will review several of the detectors that have been sent into space in the past few years and talk about the spatial environment in particular the influence of the Earth's magnetic field on charged cosmic ray particles.

### 1.1 The Cosmic Rays

The discovery of cosmic rays was a turning point in the beginning of the 20<sup>th</sup> century on the comprehension of our Universe. Indeed, they provide important information about high energy processes occurring in our galaxy and beyond. Their energy spectrum and their composition are the two measurements that bring a significant amount of knowledge. From the energy spectrum we can determine the production mechanism the cosmic rays originate from, how they are accelerated and

propagate. For example, the discovery of the *knee*, which is a change in the slope of the spectrum, rose new questions about the acceleration of the cosmic rays. From the elemental composition, by comparison with the Sun composition, we highlighted the production of secondaries and the way primaries interact with the interstellar medium. We will go in more details in the following.

### 1.1.1 Discovery of Cosmic Rays

The first hint of the existence of an extraterrestrial source of radiation was found by Hess [2] in 1911/1912 during a balloon flight when he measured the radiation level as a function of the altitude. His results were confirmed two years later in 1914 by Kohlhörster [3]. We can see the two measurements in Figure 1.1. This discovery opened the path to the cosmic rays research.

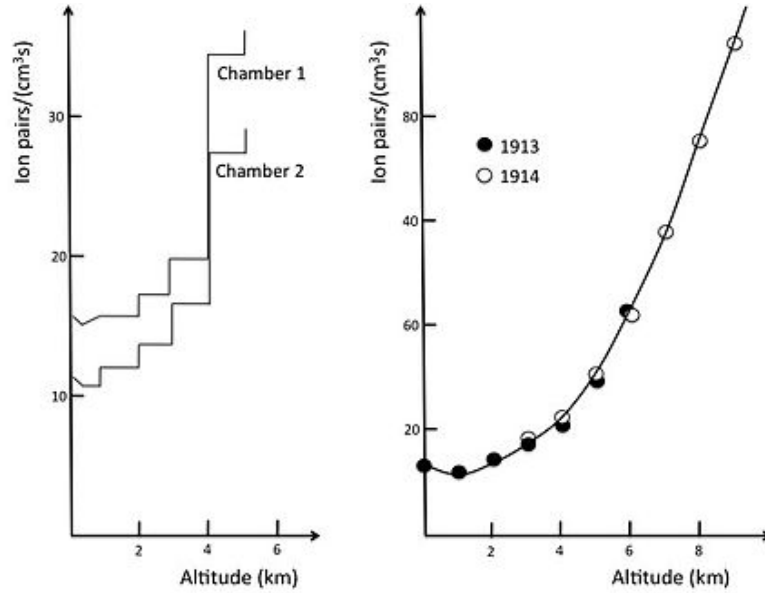


Figure 1.1 – Increase of the ionization with the altitude measured by Hess (left) and by Kohlhörster (right) [4].

Few years later, in 1927, a demonstration of the dependence of cosmic rays intensity with the geomagnetic latitude was made by Clay [5] proving clearly their charged particles nature. Following this, in 1930, Störmer [6] computed the trajectories of the charged particles through the Earth's magnetic field which lead to an important characteristic of the charged cosmic rays approaching our planet : the geomagnetic cutoff (see later). Since then, the discoveries about the propagation of the cosmic rays through first the Earth's magnetic field, then through the galactic magnetic field and through the interstellar medium never stopped. In 1949, Fermi [7] postulated a possible mechanism that accelerated cosmic ray particles to very high energy. This Fermi mechanism is one of the few mechanisms known these days to describe the acceleration of cosmic rays (more details in a later Section).

In parallel, the particle physics domain took a step forward thanks the cosmic ray study and the discovery of new elementary particles. For example, the muon in 1937 by Anderson and Neddermeyer [8] in a cloud chamber, or the pion in 1947 by Lattes, Occhialini, Powell and Muirhead [9] or the

antiproton observed in primary cosmic rays in 1979 by Golden [10]. More discoveries followed. Nowadays, we are still discovering more and more on the cosmic rays, especially about their propagation toward Earth, their composition, etc. But one subject that remains in question is how there are accelerated. Several hypothesis exist as we will see later.

### 1.1.2 The Energy Spectrum

The measurement that gives important information about the cosmic rays in general is the energy spectrum which gives the number of events per unit of surface, solid angle, time and energy. The observed spectrum of the sum of all charged particles extends in a wide energy range from  $10^6$  eV up to  $10^{20}$  eV. Figure 1.2 represents the energy spectrum with data compiled from several experiments.

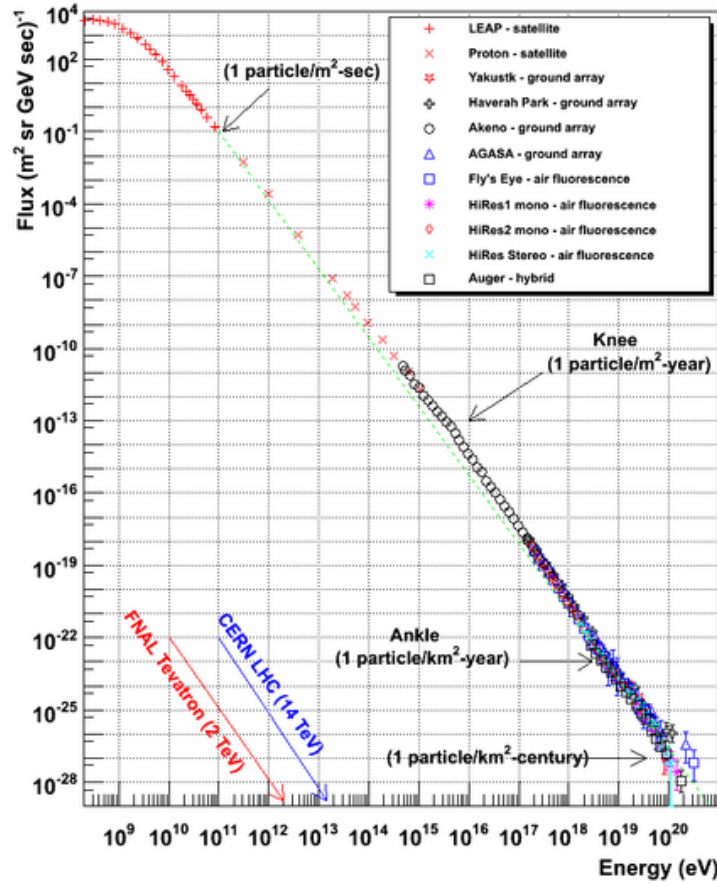


Figure 1.2 – Cosmic ray spectrum summed over all charged particles from various experiments data (credit W.F.Hanlon).

The spectrum shape follows a power law with the flux decreasing strongly with increasing energy. We can see two important features in this spectrum. The first one around  $10^{15}$  eV, called the *knee*, introduces a change in the slope and the spectrum becomes steeper. It results in a change in the

spectral index that becomes lower, from approximately  $-2.7$  to approximately  $-3$ . This change in the slope might not be visible from Figure 1.3 that is why one usually multiplies the flux by a power of

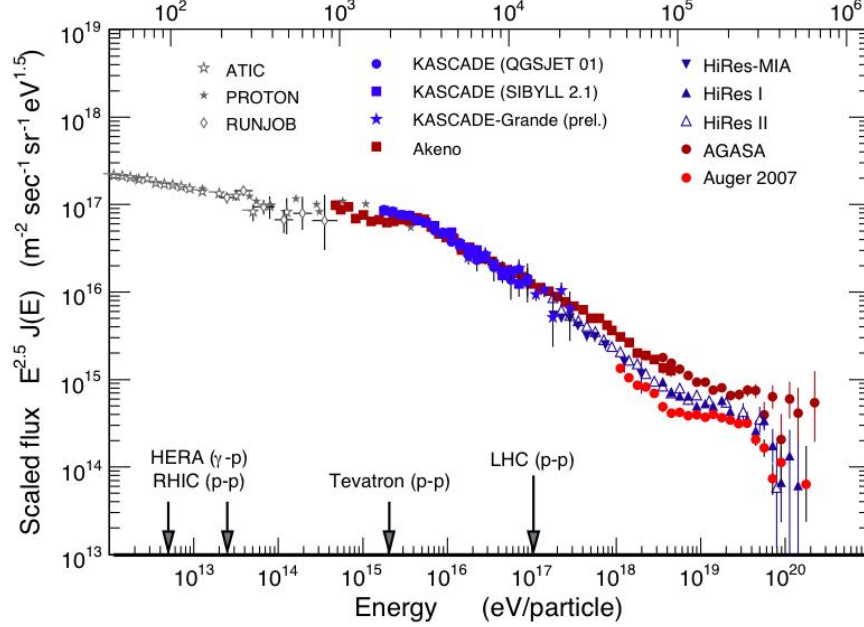


Figure 1.3 – Cosmic ray spectrum summed over all charged particles from various experiments data multiplied by  $E^{2.5}$  (credit R.Engel).

the energy near the one of the spectrum. Figure 1.3 shows a compilation of the different cosmic ray data with the flux multiplied by a factor  $E^{2.5}$ . From this last Figure we can see clearly the spectrum becoming steeper above few  $10^{15}$  eV. We can also observe the second feature in the spectrum where it flattens around few  $10^{18}$  eV. This feature is called the *ankle* [11] and the hypothesis is made that its results in a change of the cosmic ray sources as we will see later. Finally, a threshold exists at  $6 \cdot 10^{19}$  it is the Greisen-Zatsepin-Kuzmin (GZK) cutoff [12, 13] which we will detail later.

From the different features that appear all along the large energy range, a differentiation has been made between several types of cosmic rays. Indeed, we usually classify the cosmic rays in three categories. At low energy, the contribution to the cosmic ray spectrum comes mostly from the Sun, the particles are called Solar Energetic Particles (SEP). At intermediate energies, up to  $10^{15}$  eV, the particles are called galactic cosmic rays. They come from accelerating sources inside our galaxy. At very high energy, above  $10^{19}$  eV, the main hypothesis is that the observed cosmic rays should come from extragalactic sources, there are called the Ultra High Energy Cosmic Rays (UHECRs). However, the statistic is extremely low for these kind of events.

### The Low Energy Part

At low energies around few hundred of MeV, the number of cosmic ray particles decreases. This effect is due to the interaction of these charged particles with the Sun's and the Earth's magnetic fields. These two magnetic fields prevent galactic charged particles to reach the Earth which results

in a reduced flux of galactic charged particles. This effect is called solar modulation of the cosmic rays [14] and it is anti-correlated with the solar cycle. Indeed, when the solar cycle is at its maximum resulting in more frequent solar ejections, the plasma released by the Sun impacts the number of particles capable of reaching Earth which results in a lower flux of cosmic rays. This modulation provides a useful verification of the basic transport equation of the cosmic rays.

In the mean time, between few MeV and hundred of MeV, the Sun plays an important role providing accelerated charged particles through its magnetic activity. These particles are called Solar Energetic Particles (SEP) [15]. They were discovered because of the increase in the cosmic ray intensity on July 25, 1946 that Forbush linked to a solar flare. SEP are accelerated both in flares and at coronal shock waves. The Sun's effect on the cosmic ray spectrum results in a change in the flux values at very low energies over time. The flux is higher when the solar magnetic activity cycle is at its maximum when the coronal mass ejections and flares are around 50 times more frequent than at its minimum.

### Galactic Cosmic Rays

Galactic cosmic rays are the most abundant type of cosmic rays after few GeV. They originate from different sources within our galaxy, the most probable sources being Supernova Remnants (SNR) [16]. The range of energy of the GCRs is quite large but has a limitation at low energies due to the solar modulations and at very high energies due to the GZK cutoff. As we have seen previously, the spectrum shape is a power law so the number of detected GCRs decreases with increasing energy which results in a very low number of very high energy particles detectable. The first structure that appears along the spectrum shows a change in the spectral index leading to a steeper spectrum above few  $10^{15}$  eV, it is called the *knee*. The galactic charged particles are affected by the galactic magnetic field through Lorentz force and can leak from the galaxy. Due to the equilibrium between the centrifugal force and Lorentz force we have :

$$p = Ze\rho B \quad (1.1)$$

with  $p$  the momentum of the particle,  $Ze$  the charge of the particle,  $\rho$  the bending radius and  $B$  the magnetic field. If we take  $B = 10^{-10}$  T for the galactic magnetic field [17] and  $\rho = 5$  pc above which particles start to leak from the galaxy, the maximum momentum is  $p_{max} \approx 10^{15}$  eV/c for a singly charged particle. Therefore, particles with an energy higher than  $10^{15}$  eV start to leak from the galaxy resulting in a steeper spectrum above this energy. One important thing to notice is that the maximum momentum depends on the charge of the particle which means that the position of the *knee* is different from one element to another. There are other possible explanations for the position of this structure :  $10^{15}$  eV is the approximate maximum energy that a supernova explosion can provide and there could be a change in the interactions cross-section for the charged particles above this energy.

At higher energies, a second structure is visible around  $10^{18}$  eV. It is called the *ankle* and around these very high energies the spectrum tends to flatten. The second change in the spectrum slope is generally assumed to be due to additional particles coming from extragalactic sources [18]. The galactic cosmic rays and the extragalactic cosmic rays should both contribute to the energy spectrum increasing the detected flux. However, this assumption has not been proven yet.

### Ultra High Energy Cosmic Rays

Ultra High Energy Cosmic Rays are assumed to originate from extragalactic sources but for now, no direct proof has been found. However, at the very end of the galactic cosmic ray spectrum

Greisen, Zatsepin and Kuzmin postulated the presence of a cutoff known as the GZK. This cutoff would be due to the fact that particles with energy exceeding around  $10^{19}$  eV would interact with the cosmic blackbody radiation losing a large fraction of their energy. At and above this energy, resonances appear which largely amplify the proton- $\gamma$  cross-section meaning that almost all the particle will interact with the cosmic microwave background photons. Indeed, the calculation has been made that the threshold energy for the photoproduction of pions with a blackbody photon of temperature 2.7K would be  $6 \cdot 10^{19}$  eV. Therefore, it would be unlikely to detect a primary particle above this energy. The GZK cutoff theory has been observed recently by two experiments Auger and HiRes [19, 20], Figure 1.4 shows the latest results from these two experiments. Nevertheless, in contradiction with what as

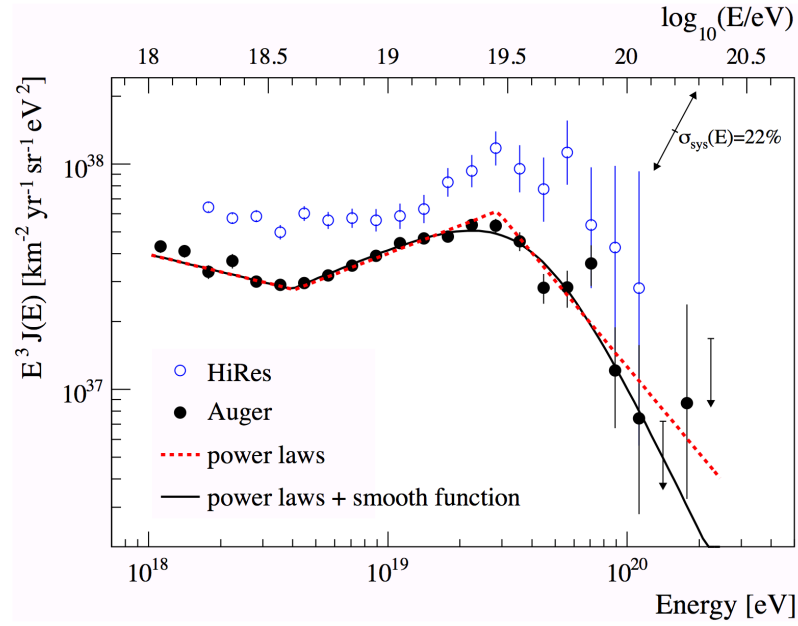


Figure 1.4 – *HiRes and Auger results on UHECRs [19].*

been said previously about the GZK cutoff, several events have been observed with energies above  $10^{20}$  eV. The apparently observed GZK cutoff in the latest measurement could result in the change in the slope of the cosmic ray spectrum or in the presence of extragalactic sources. In conclusion, the question of the existence of extragalactic cosmic rays is still opened.

### 1.1.3 Elemental Composition of the GCRs

The galactic cosmic ray composition knowledge is fundamental to understand their origin and how they propagate. Figure 1.5 show the relative abundance of the cosmic rays compared to the solar system normalized to Silicon ( $Z=14$ ). Protons are the most abundant, they represent almost 85% of the total cosmic rays detected, helium is the second most abundant element with around 12%. All the other elements with charge greater than 3 represents only 3% of the particles and to that electrons and positrons are added. The chemical composition detected contains the same elements for the galactic cosmic rays than for the Sun but shows differences for what concerns their abundances. Indeed, if we

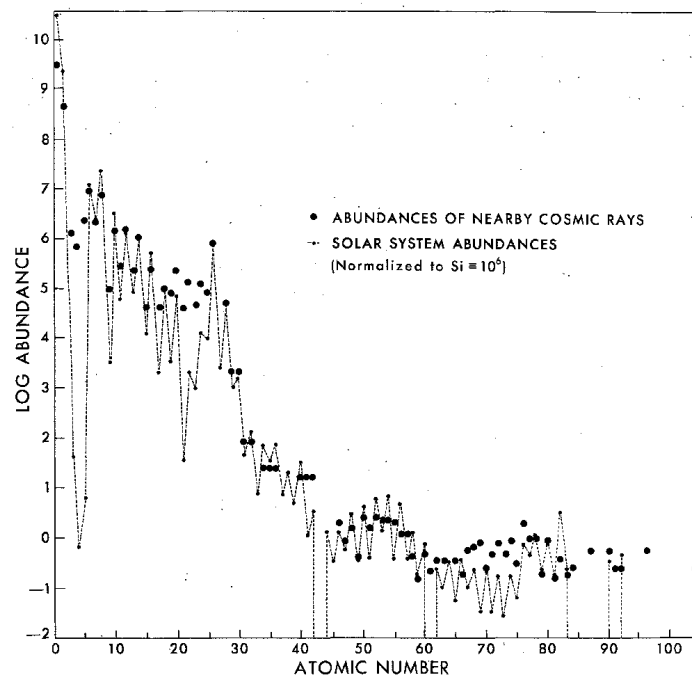


Figure 1.5 – *Cosmic ray abundance at the top of the atmosphere compared to the solar system abundance, normalized to Silicon (from Price, 1973a).*

take a look closer to the abundances of light nuclei, in Figure 1.6, several elements are more abundant

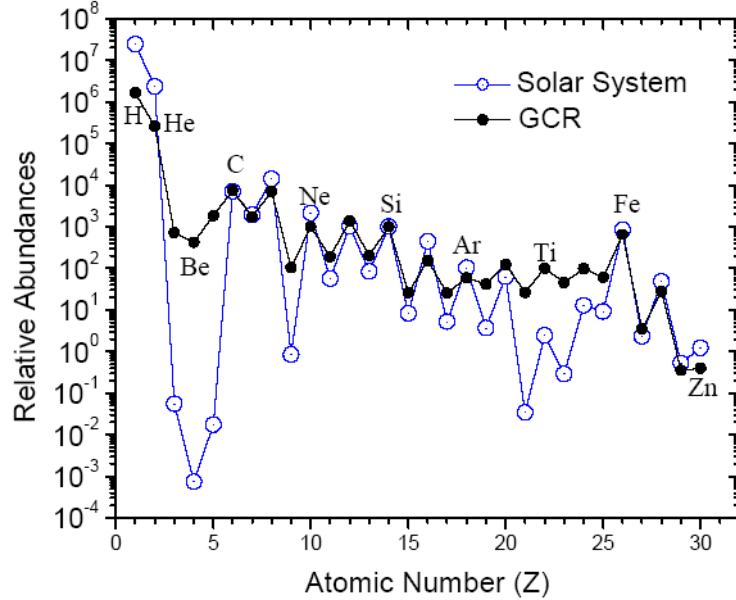


Figure 1.6 – Cosmic ray abundance compared to the solar system abundance, normalized to Silicon (credit ACE).

in the cosmic rays than in the Sun. The first set of elements are Lithium, Beryllium and Boron ( $Z=3-5$ ), the second group is composed of the 5 elements below Iron ( $Z=21-25$ ). This is explained by the fragmentation or spallation of the relatively abundant elements such as Carbon ( $Z=6$ ) and Oxygen ( $Z=8$ ) or Iron ( $Z=26$ ) in the interstellar medium before reaching Earth leading to an excess in the abundance of the elements they produce. These resulting elements from fragmentation and spallation are called secondary cosmic rays in opposition to the primary cosmic rays that originate directly from their sources.

From Figure 1.5 we can also understand the production of the galactic cosmic rays. The first two elements, proton and helium, are the most abundant and were produced by the primordial nucleosynthesis, with thermonuclear reactions in the first few minutes after the Big Bang. The rest of the elements are produced by stellar nucleosynthesis. The second step we see contains elements from Lithium to Iron, and are created by hydrogen and helium burning. After this we have the third step which contains heavy elements that are produced by neutron capture which is why they are less abundant.

#### 1.1.4 Acceleration and Propagation

Today, the sources of the galactic cosmic rays is one of the major unsolved question in the cosmic ray field. Several assumptions have been made about the sources but they must be extremely energetic to accelerate the particles to the very high energies we detect them. Supernova Remnants (SNRs) constitute the most conceivable candidates for the production of galactic cosmic rays. Other



sources have been suggested such as quasars, Active Galactic Nuclei (AGN), accreting black holes or pulsars. Several acceleration mechanisms models are explored but it is not clear yet how galactic cosmic rays are accelerated at their sources and along their path through the galaxy. We are going to give an overview of two different type of acceleration mechanisms.

Considering SNRs as the main contributor for galactic cosmic rays production, particles would be accelerated through diffusive shock acceleration. When a massive star implodes, a part of its mass is ejected into the interstellar medium which results in a shock front. By taking a shock front with velocity  $v_{shock}$  and the ejected gas with velocity  $v_{gas}$ , if we consider a particle with velocity  $v_{part}$ , the gain in energy would be of :

$$\frac{\Delta E}{E} \approx \frac{2(v_{shock} - v_{gas})}{v_{part}} \quad (1.2)$$

Similarly, by taking a particle trapped between two shock fronts with the inner front having a much higher velocity, one obtains a gain in energy of about :

$$\frac{\Delta E}{E} \approx 2 \frac{v_{shock}}{v_{part}} \quad (1.3)$$

Due to the linearity in the velocity of these shock acceleration mechanisms, they are often referred as first order Fermi mechanism.

The second mechanism usually used to explain acceleration of galactic cosmic rays is the second order Fermi mechanism, more generally called Fermi mechanism. This mechanism occurs when a galactic particle interacts with magnetic clouds. The gain in energy from this acceleration process is quadratic in the cloud velocity  $v_{cloud}$  through :

$$\frac{\Delta E}{E} \approx 2 \frac{v_{cloud}^2}{v_{part}^2} \quad (1.4)$$

However, to be efficient and to accelerate properly the incoming particle, this mechanism needs an minimum injection energy. In most models the two acceleration mechanisms are coupled to explain the acceleration of galactic cosmic rays at the observed energies.

## 1.2 Cosmic Ray Detection

The measurement of cosmic rays is made with several types of detectors, based on different detection principles. Located on the ground or in the atmosphere, or even in space as we will see in the next section, the detectors will be dedicated to different energy ranges. We can distinguish two different types of cosmic rays detection : the direct detection which uses the interaction of the charged particles through different processes, balloon-borne and space based experiments use it, and the indirect detection through the interaction of the primary cosmic rays with the atmosphere, used in the ground based detectors. The same detection principle are used whether for direct or indirect measurement.

### 1.2.1 Direct Detection

Six different detection principles exist for charged particle detection : the ionisation, the electron-hole creation, the excitation, the bremsstrahlung process, the Čerenkov radiation and the

transition radiation. The dominant process is the energy loss through ionisation and excitation described by the Bethe-Bloch Equation [21] :

$$-\frac{dE}{dx} = Kz^2 \frac{Z}{A} \cdot \frac{1}{\beta^2} \left\{ \frac{1}{2} \ln \frac{2m_e c^2 \beta^2 \gamma^2 T_{max}}{I^2} - \beta^2 - \frac{\delta}{2} \right\} \quad (1.5)$$

where  $K = 4\pi N_A r_e^2 m_e c^2 \approx 0.307 \text{ MeV}/(\text{g}/\text{cm}^2)$ ,  $N_A$  Avogadro's number,  $r_e$  the classical electron radius,  $m_e c^2$  the electron rest energy,  $z$  the charge of the incident particle,  $Z$  the target charge,  $A$  the target mass,  $\beta$  the velocity of the incident particle,  $\gamma$  the Lorentz factor,  $T_{max}$  the maximum energy transfer to an electron,  $I$  the average ionization energy of the target and  $\delta$  the density correction. Figure 1.7 shows this energy loss for different materials. The energy loss follows a  $1/\beta$  decrease at low

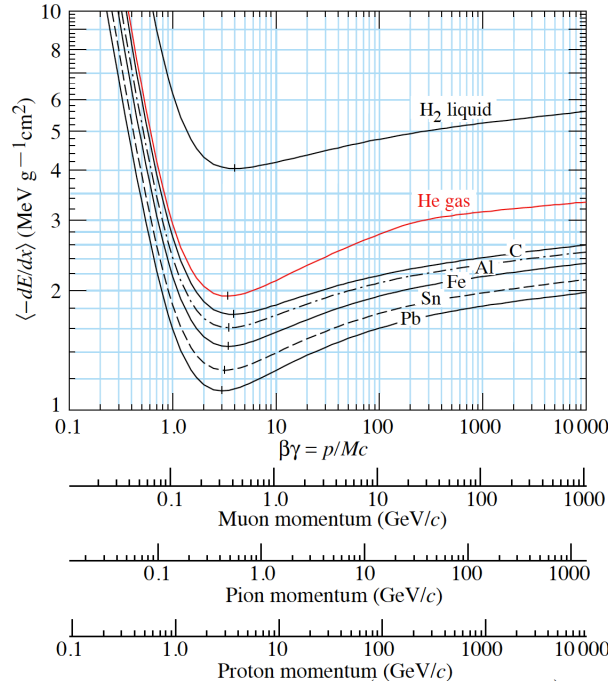


Figure 1.7 – Mean energy loss rate in various materials [21].

energy until reaching the minimum of ionization at  $\beta\gamma$ . Then the energy loss increases logarithmically until reaching the so called Fermi plateau. The ionization process is often used in gaseous detectors and semiconductor detectors through electron-hole pairs production and the excitation process in the scintillating detectors. The bremsstrahlung process occurs at high energies. It is an energy loss through electromagnetic radiation and is most of the time used in the calorimeters because it creates electromagnetic showers in addition to the electron-positron pair production. Finally, the Čerenkov radiation results in a light emission when the velocity of the particle is greater than the speed of light in the medium.

All of the detection principles are used in different type of detectors. Usually, to build a cosmic ray detector, several of these detectors are used in order to provide complementary or redundant characteristic measurements. For example, the AMS-02 experiment is using all of the principles mentioned

previously since it has a transition radiation detector (gaseous detector), a time-of-flight (scintillating detector), a Silicon tracker (semiconductor detector), a ring imaging Čerenkov counter and a electromagnetic calorimeter. The direct detection is used for space based experiment as well as for ballon-borne experiments. We will describe the space based experiments in the next Section.

The ballon-borne experiments are cosmic ray detectors carried by a large volume balloon that goes up to the stratosphere. These experiments are usually short duration flight from few hours to several days. The complexity of the on-board detector can vary from an experiment to an other and can be simple as well as very elaborate. As an example, the BESS-PolarII experiment [22] was launched from Antartica in December 2007 and recorded 24.5 days of observation. Figure 1.8 show the launch of the



Figure 1.8 – *Launch of the BESS-PolarII balloon in Antartica (credit Nasa).*

balloon. The main purpose of this experiment was the measurement of low energy antiprotons and search for primordial antimatter. BESS-PolarII had a complex on-board detector as we can see from the Figure 1.9 regrouping detectors using different detection principles.

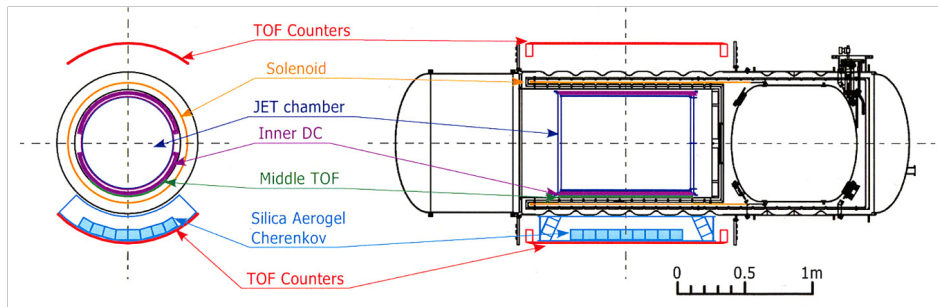


Figure 1.9 – *Schematic view of the BESS-PolarII detector [22].*

### 1.2.2 Ground Based Detection

At very high energy, due to the extremely low flux of galactic cosmic rays, direct measurement is almost impossible because it requires either a very long detection time or a very large detection area. However, such a duration and surface of an experiment is possible on the ground. The ground based experiment does not detect the primary particles directly since they are interacting at the top of the atmosphere producing *extensive air showers*. When a galactic cosmic ray particle interacts with a nucleus of the air it will produce many new particles. First, the number of particles increase rapidly on their way down to the ground, but since they loose energy at a certain point, called the shower maximum, they will not interact anymore and the number of created secondary particles will decrease. The number of secondary particles created depends on the incident energy of the primary cosmic ray. The shower extends in a disk around the incident axis allowing to often reconstruct the trajectory of the incoming primary cosmic ray. Figure 1.10 show a schematic view of the development of an air

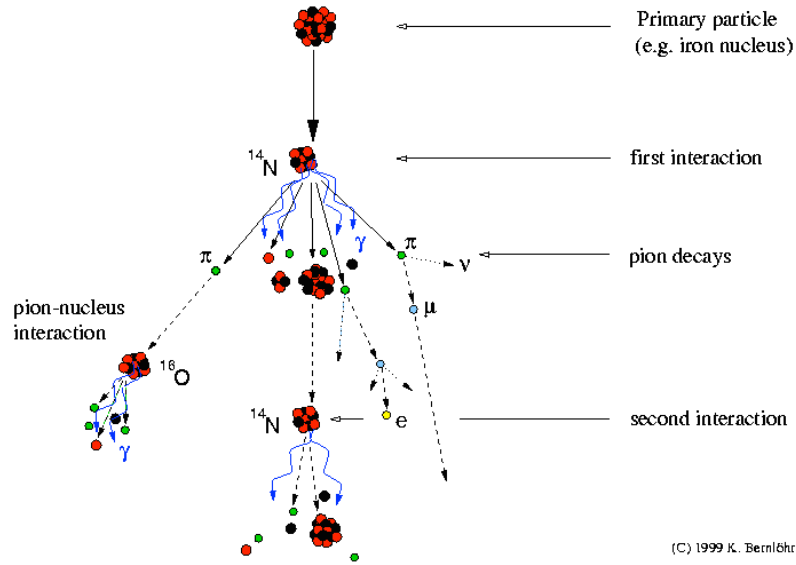


Figure 1.10 – Schematic view of an air shower (credit K.Bernlöhr).

shower.

Air showers results in several different kind of secondaries particles from nuclei to leptons and photons. Therefore, different detector types exists, an overview of them can be seen in the figure Figure 1.11. For relatively low energy, about few TeV, Čerenkov light produced by the shower can be detected by light-sensitive devices. The principle of the Čerenkov telescopes is to measure the cone of light emitted by the shower which is beamed around the incident direction of the primary particle, referred as the Čerenkov light pool. An example of an experiment using this detection principle is the H.E.S.S. [23] that uses a stereoscopic telescope system with several telescopes arranged in form of a square of 120m side length. Figure 1.12 show a schematic view of the H.E.S.S. experiment principle.

Primary incident cosmic ray particles with sufficient energies can generate secondary particles that will reach the ground. It is then possible to detect directly these produced secondary particles through more classical detection principles. The Pierre Auger Observatory [24] is capable to detect primary cosmic rays of very high energy that interact at the top of the atmosphere by measuring the char-

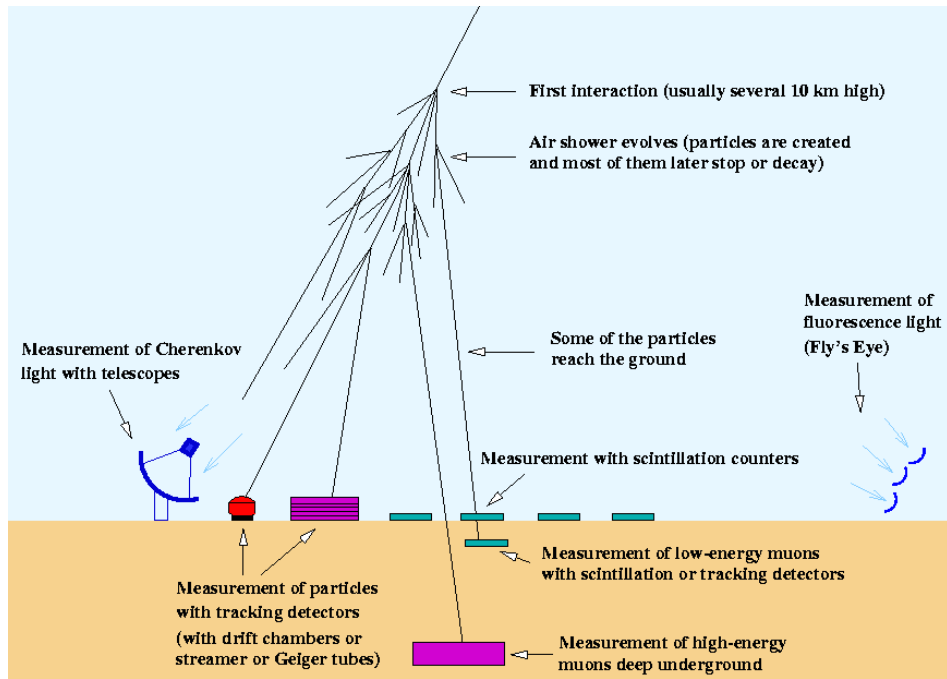


Figure 1.11 – Schematic view of an air shower with the different detector types associated (credit K.Bernlöhr).

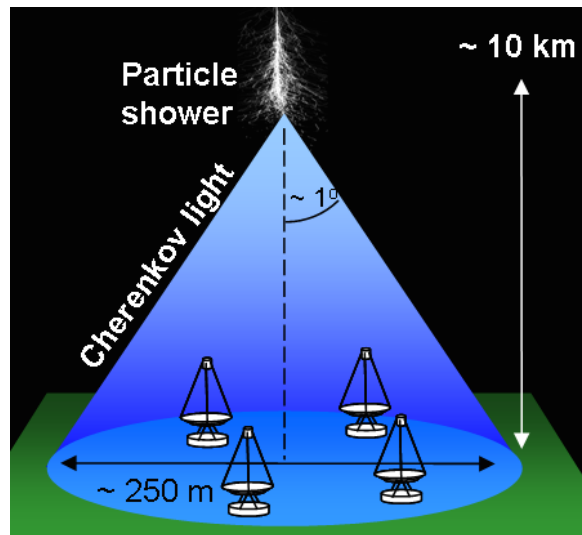


Figure 1.12 – Schematic view of H.E.S.S. experiment [23].

acteristics of the air showers by two methods. Indeed, the experiment couples together two kind of detectors : tanks of pure water (using Čerenkov radiation detection principle) spread on a  $3 \cdot 10^3 \text{ km}^2$  area, and fluorescence detectors that measure the fluorescent light coming from the interaction of the particles of the air showers and the molecules of the atmosphere. The fluorescence detectors are able to determine the total energy of the air shower but only during clear moonless night while the water tank detectors are able to detect only a fraction of the total energy but at any time. Figure 1.13 shows

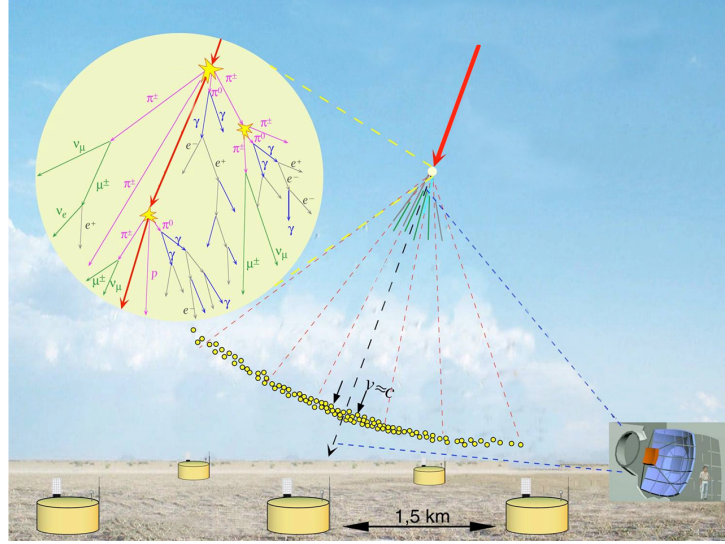


Figure 1.13 – *Schematic view of the detection principle of the Pierre Auger Observatory (credit Pierre Auger Observatory).*

a schematic view of the detection principle of the experiment.

The last detection principle is used for ultra high energy cosmic rays. The concept is to detect nitrogen fluorescence light excited by the ionization trail of the shower. These detectors are mostly known as Fly's Eye detectors. They consist in a collection of light sensors usually coupled with mirrors to detect the fluorescent light. The High Resolution Fly's Eye Cosmic Ray Detector (HiRes) experiment [25] used this techniques to detect cosmic rays with energies up to  $10^{20} \text{ eV}$ .

### 1.3 Space Based Experiments

Galactic cosmic rays with intermediary energies, from GeV to TeV, are detected in space before they interact with the atmosphere, therefore, it is possible to measure directly the incident primary particles. The space based experiments are usually on-board of satellites or space stations orbiting around Earth. The altitudes and types of orbit can be different from one experiment to an other. The space based experiments require a large time range of data taking to make an improvement in the measurements of galactic cosmic ray spectrum. The PAMELA experiment [26] paved the way of the long duration space flight by staying in orbit more than 9.5 years. Considering the positive results of the first launched experiments in space and with the continuous improvement of the detectors, the space based experiment field is rapidly expanding.

We are going to see in more details what kind of experiments are currently taking data in space. The spatial environment is an important point to consider. The Earth's and the Sun's magnetic fields play a preponderant role in the detection of the charged particles. We are going to introduce the influence of the near Earth environment on the primary galactic cosmic rays.

### 1.3.1 Detectors

The experiments sent into space are usually composed of a collection of detectors based on different detection principles (see 1.2.1). Indeed, these different detectors provides usually complementary information. These configurations make the space based detectors very complex experiments. Two kinds of detectors can be defined : the calorimetric detectors which provide a measurement of the energy per nucleus and the magnetic spectrometers which provide a measurement of the rigidity. They must operate properly in a hostile environment where, if a problem occurs, nothing can be done in general.

We are going to detail three of the currently data taking experiments in space : PAMELA, AMS-02 and DAMPE.

#### PAMELA

The PAMELA experiment (a Payload for Antimatter Matter Exploration and Light-nuclei Astrophysic) [26] is a cosmic ray detector on-board of the Russian Resurs-DK1 satellite launched June 15, 2006. It is continuously taking data in a quasi-polar  $70^\circ$  inclination orbit at an average altitude of 580km since 2010 (before the altitude was varying between 350km and 600km). The detector is composed of a spectrometer containing a 6 planes tracking system surrounded by a permanent magnet, a 3 planes time-of-flight system, a calorimeter on the bottom and a neutron detector. Figure 1.14 shows a schematic view of the detector. PAMELA is dedicated to investigate the antiparticle component of the cosmic rays, but results on the nuclei spectrum and composition of the galactic cosmic rays on a large energy range have also been published [27], it is also dedicated to low energy effects such as solar modulation.

#### AMS-02

The AMS-02 (Alpha-Magnetic Spectrometer) experiment [28] is on-board of the International Space Station and taking data since May 19, 2011. The ISS describes a nearly circular orbit at an average altitude of 400km. The composition of the detector is more complex than for the PAMELA experiment since to the tracking system, the time-of-flight system and the calorimeter are added a transition radiation detector and a ring imaging Čerenkov counter. A detailed description of the detector is given in the next Chapter. AMS-02 first results have been published relating measurement on the electron and positron fluxes, on the positron excess, and on the proton and helium spectrum.

#### DAMPE

DAMPE (DARk Matter Particle Explorer) [29] is the last detector sent to space, it was launched on December 17, 2015. It describes a sun-synchronous orbit at an altitude of 500km. It is composed

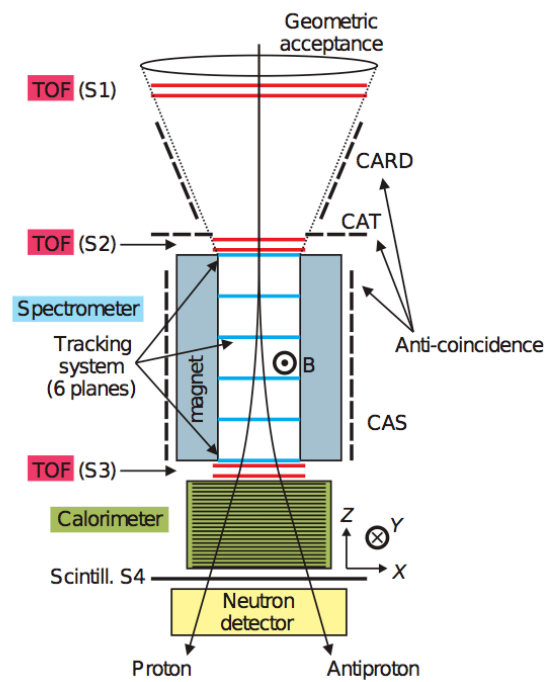


Figure 1.14 – Schematic view of the PAMELA detector [26].



of a plastic scintillator detector, a silicon-tungsten tracker consisting in 6 tracking double layers, a BGO (Bismuth Germanium Oxide) calorimeter and a neutron detector at the bottom of the detector. Figure 1.15 shows the schematic view of the detector. The purpose of DAMPE is to detect electrons,

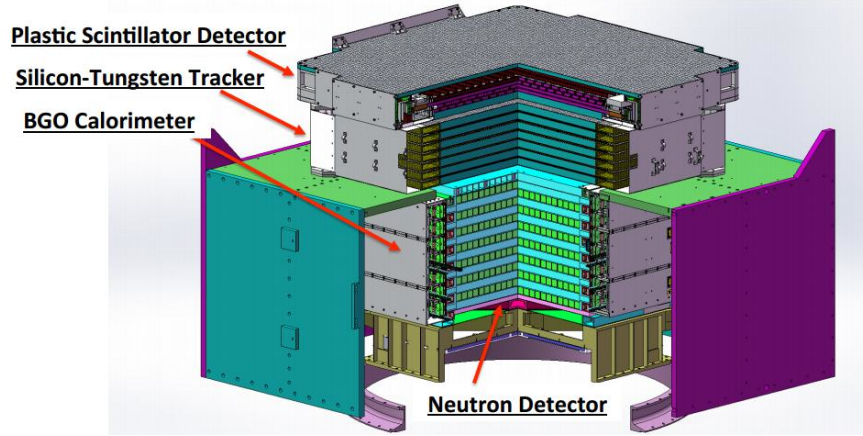


Figure 1.15 – Schematic view of the DAMPE detector [29].

charged cosmic ray nuclei as well as gamma rays at higher energy with a high energy resolution than the previous detectors.

### 1.3.2 Spatial Environment

Magnetic fields play a role at all scales : galactic, stellar, planetary. Charged particles interact with magnetic field through the Lorentz force explaining why charged cosmic ray particles path is influenced by the galactic magnetic field, though, this field is very low. Earth owns also a magnetic field that is influencing the path of the charged cosmic rays reaching the atmosphere, but its magnitude is grater than the magnitude of the galactic field providing stronger effects on the particles. This field can be approximate by a magnetic dipole, however, this dipole is tilted by an angle of about  $11.5^\circ$  with respect to the Earth's rotational axis, see Figure 1.16. Due to the magnetic field, charged cosmic ray particle trajectories are bend. There exists two main effects that need to be carefully taken into account : the geomagnetic cutoff and the South Atlantic Anomaly.

#### The Geomagnetic Cutoff

By traveling along the magnetic field lines, the charged cosmic ray particles can reach the atmosphere at the Earth's poles. At the equator the Lorentz force is at its maximum prohibiting particles with a certain energy to reach a certain altitude at a certain angle. This effect called the geomagnetic cutoff depends on the geomagnetic latitude. For a detector crossing several geomagnetic latitudes, this effect is important.

The geomagnetic cutoff corresponds to the minimum energy needed by a charged particle trying to

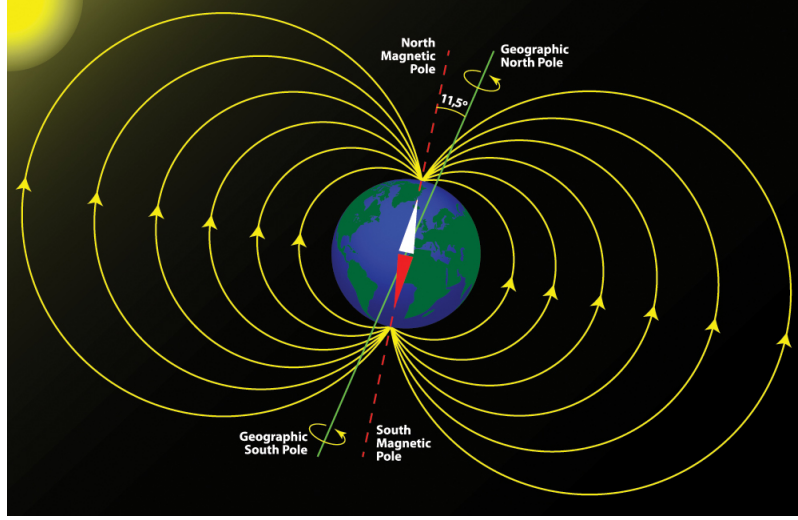


Figure 1.16 – *The Earth's magnetic dipole (credit Milagli via Shutterstock).*

reach a certain altitude [30]. The Störmer equation is an approximation using a pure dipolar field :

$$R_{cut} = \frac{M \cos^4 \Theta_M}{r^2 [1 + \sqrt{1 - \sin \epsilon \sin \xi \cos^3 \Theta_M}]^2} \quad (1.6)$$

with  $M$  the magnitude of the dipole moment in  $\text{G}\cdot\text{cm}^3$ ,  $r$  the distance from the dipole center in cm. For the two angles  $\epsilon$  and  $\xi$  we have to construct a hemisphere with as center the point where the particle arrives on the dipole and the plane of this hemisphere is the tangent plane at this point;  $\epsilon$  is then the angle from the zenith direction and  $\xi$  is the azimuthal angle measured clockwise from the direction to the north magnetic pole. This equation is used in the majority of the calculation, however, a more complex description of the Earth's magnetic field is used in the IGRF models (International Geomagnetic Reference Field) [31].

### The South Atlantic Anomaly

Secondaries particles produced when primaries particles interact with the atmosphere can be trapped by the Earth's magnetic field due to their energy. These trapped particles go back and forth along the magnetic field lines under the effect of *magnetic mirroring* accumulating along the line. These accumulated particles represent the Van Allen radiation belts, see Figure 1.17.

The South Atlantic Anomaly (SAA) [32] results in a large area in the south atlantic ocean, near southern Brazil, where the radiation is way more intense than everywhere else. This is due to the crossing of the inner Van Allen radiation belt with the Earth's atmosphere. Indeed, since the Earth's magnetic dipole is tilted with respect to its rotational axis, the radiation belt gets closer to the atmosphere providing the radiation excess.

In this Chapter an overview of the cosmic rays has been provided. The choice has been made

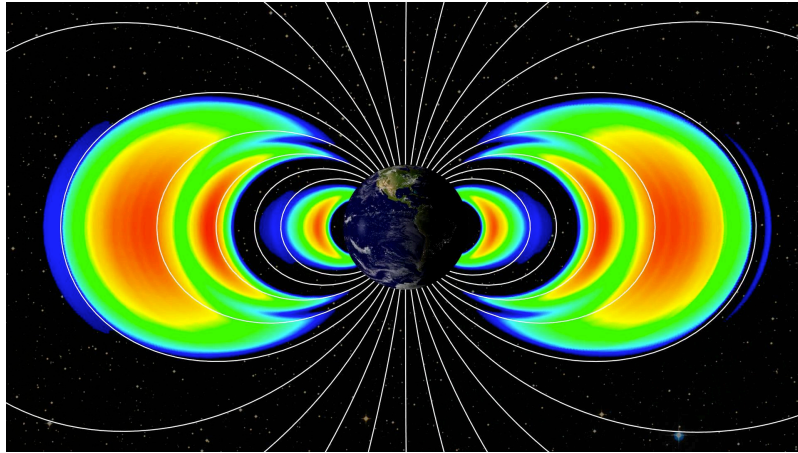


Figure 1.17 – *An arctic view of the Van Allen radiation belts (credit Nasa).*

to focus on charged galactic cosmic ray particles and on space based experiments as this thesis will provide a Helium spectrum analysis with the AMS-02 experiment. The detailed discussions on the interaction of charged particles used in the detector and on the interaction of the charged particles through the Earth's magnetic field will be useful for the following analysis.



## Chapter 2

# THE AMS-02 EXPERIMENT

This Chapter is dedicated to the description of the AMS-02 experiment. The Alpha-Magnetic Spectrometer is a space-based galactic cosmic ray detector on board of the International Space Station (ISS). After a successful launch in May 2011 and its installation on the ISS, the detector is operating nominally and taking data since then. The detector will last for the entire lifetime of the ISS, from 10 to 20 years. Due to its long duration and its location in space, the AMS-02 experiment has no direct competition yet. It has already published measurements on several cosmic ray fluxes such as Electron and Positron [33], Proton [34] and Helium [1] with a precision never reached in the past. The construction of AMS-02 started in 1999 right after a test flight of the reduced qualification model AMS-01 [35]. This test experiment was on-board of the space shuttle Discovery during the flight STS-91 in June, 1998. This test was a complete success in terms of technical challenges but also the scientific results [36] obtained permitted to conclude that such an experiment was necessary for the cosmic ray study.

In the first Section of this Chapter, we are going to describe how AMS-02 is operating in space and what needs to be considered when working with a space-based experiment. Then we will provide an overview of the detector. Indeed, AMS-02 is composed of several subdetectors : the Transition Radiation Detector (TRD), the Time of Flight (ToF), the Silicon Tracker, the Anti-Coincidence Counters (ACC), the Ring Imaging Čerenkov Counter (RICH) and the Electromagnetic Calorimeter (ECAL). To that is added a permanent magnet that is around the Silicon Tracker. All these different aspects of the detector will be described in the second Section. Then, we will introduce how AMS-02 is taking and managing the data. We will describe the functioning of the Trigger and how the events are detected and stored. Finally, we will discuss the Monte Carlo (MC) simulations made by the collaboration.

### 2.1 AMS-02 on the ISS

AMS-02 has been launched in space on-board of the space shuttle Endeavour for the mission STS-134 from Cap Canaveral, Florida (USA) on May 16<sup>th</sup>, 2011. The installation of the detector took three days and started operating on May 19<sup>th</sup>, 2011. We can see the exact location of the detector as an external payload of the ISS in Figure 2.1. The ISS is orbiting around Earth with a nearly circular orbit with an inclination of 51.6° at an average altitude of 400km and makes 15.54 orbits per day

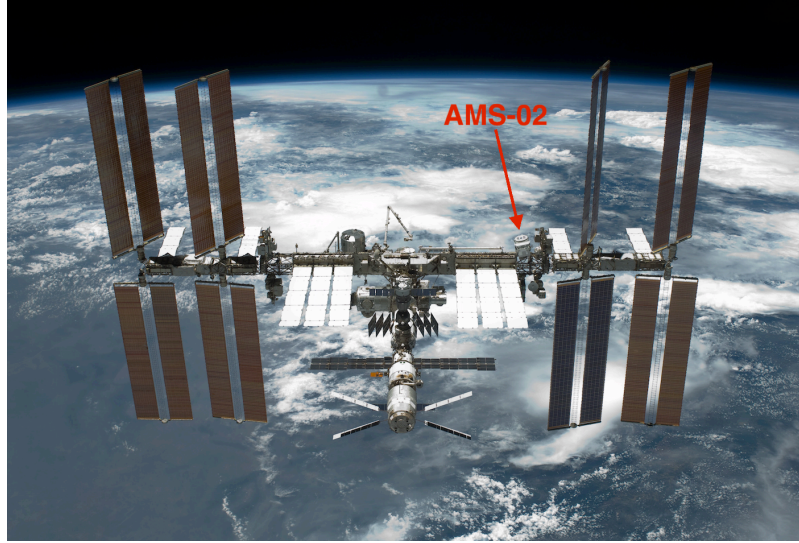


Figure 2.1 – *AMS-02 location on the ISS (credits NASA).*

which represents a period of 93 minutes per orbit. Figure 2.2 shows several orbital tracks followed by

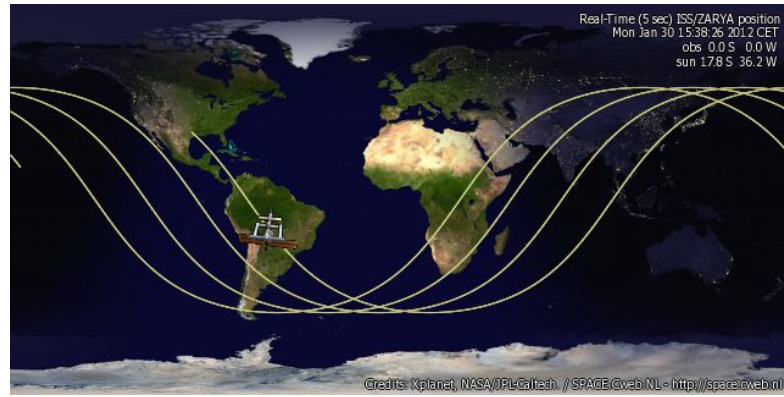


Figure 2.2 – *Example of few ISS orbits path (credits NASA/JPL).*

the ISS for illustrating.

Once AMS-02 had been installed on the ISS it started taking data only three hours later. Data are continuously taken since then. Operating and making sure that data are always transmitted to Earth requires an important control system. To this end, we have the AMS Payload Operation Control Center (POCC) and the Sciences Operation Center (SOC) both located at CERN (Geneva, Switzerland).

### 2.1.1 Operation in Space

There are three different electrical interfaces between AMS-02 and the ISS : the Power Interface, the High Rate Data Link (HRDL) and the Low Rate Data Link (LRDL) [37]. The first one provides the power from the ISS to the detector. On-board of the ISS the power is delivered by the solar array panels. A maximum power of 2500W is dedicated to the detector. The two other electrical interfaces are used for data transmission, we will see them in more details thereafter.

Since the detector is located in space, the operating conditions are quite hard especially for what concerns the temperature. Due to the orbit of Earth around the Sun, the ISS thermal conditions are always changing going from very low temperatures to very high temperatures. These conditions constitute one of the most challenging task for AMS-02 to operate in nominal conditions since the response of the subdetectors depends strongly on the temperature. That is why all the part of the detector needs to be constantly checked for their temperatures. To do so, AMS-02 contains around 1100 temperature sensors and 298 heaters that can be used when the temperature is critical. All of this is monitored continuously from the AMS POCC.

### 2.1.2 Data Transmission

As seen previously, two electrical interfaces linking AMS-02 to the ISS are dedicated to data transmission. The first one, the HRDL, is used to send data from the four JMDC (see section 2.3.2), which are the main computers on-board AMS-02, to the ISS at an average rate of 10Mbits/s. Then, these data are sent to one of the Tracking and Data Relay Satellites (TDRS) that relay them to the White Sands Ground Terminal in New Mexico (USA). After that, the data are transmitted to Payload Operation and Integration Center (POIC) at Marshall Space Flight Center (MSFC). A copy of the data is then transmitted to the POCC. The second electrical interface dedicated to data transfer, the LRDL, is used to directly transmit monitoring data at an average rate of 30KBits/s but also to receive operation commands from the POCC by using the reversed path at an average rate of 1KBits/s.

Two kind of data are transmitted from the AMS-02 : the science data (SCI) and the housekeeping data (HK). The SCI data contain all the information from every subdetectors attached to any event detected. The HK data contains information related to the monitoring data. Both of these data are transmitted from the detector through the HRDL but since a Ku-band transmission is used it can suffer from some delays. Only the HK data are transferred using S-band to allow a real-time monitoring of the detector.

In addition, a laptop is available on-board the ISS to store up to two month of data to bridge transmission gaps and avoid loss. Whenever it is needed the data from the laptop are sent to the ground.

## 2.2 AMS-02 Subdetectors

AMS-02 is measuring three characteristics of each particles passing through it : the charge, the energy and the momentum vector. This is made possible by the different subdetectors from which it is composed. Moreover, each characteristic is measured redundantly. There are six subdetectors that we are going to see in details : the Transition Radiation Detector (TRD), the Time of Flight (ToF), the Silicon Tracker (tracker), the Anti-Coincidence Counters (ACC), the Ring Imaging Čerenkov Counter

(RICH) and the Electromagnetic Calorimeter (ECAL). A cut view of AMS-02 with the different sub-detectors can be seen in Figure 2.3. All of these six subdetectors can measure the charge of any

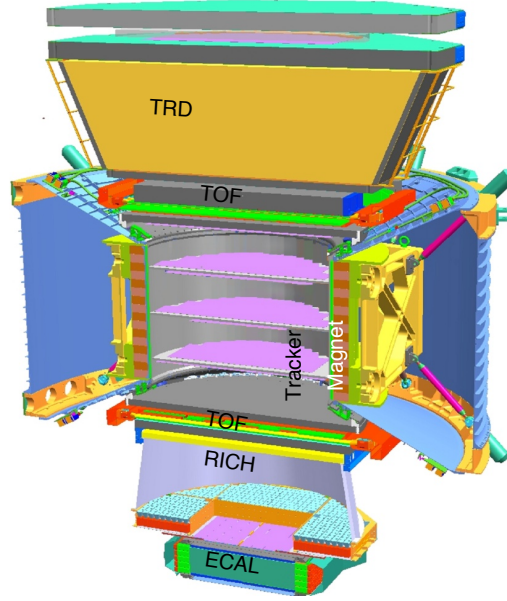


Figure 2.3 – *Cut view of AMS-02 [28].*

particle going through them. For the energy, the ToF, the RICH and the ECAL can measure it. The momentum can be measured by the Tracker due to the permanent magnet that surrounds the seven Inner Tracker planes.

AMS-02 was a technical challenge to build due to weight and power restrictions. It is composed of 15 subsystems among them are the six subdetectors named previously that we are going to define in detail. All of them were built all over the world in the different Universities that compose the AMS-02 collaboration and brought back to CERN for assembly, testing and space qualification testing. The detector was then flown to the Kennedy Space Center (USA) for final testing and to be prepared for the launch. It took a total of 11 years to build from 1999 to 2010. The configuration changed by substituting the superconducting magnet to a permanent one to allow a much longer stay on the ISS and also by moving one layer to the top and adding a plane to the Silicon Tracker on top of ECAL to increase the level arm. A more complex view of the detector can be seen in the Figure 2.4 also showing structures. The final configuration of the detector has a volume of  $64\text{m}^3$  for a total weight of 8.4t.



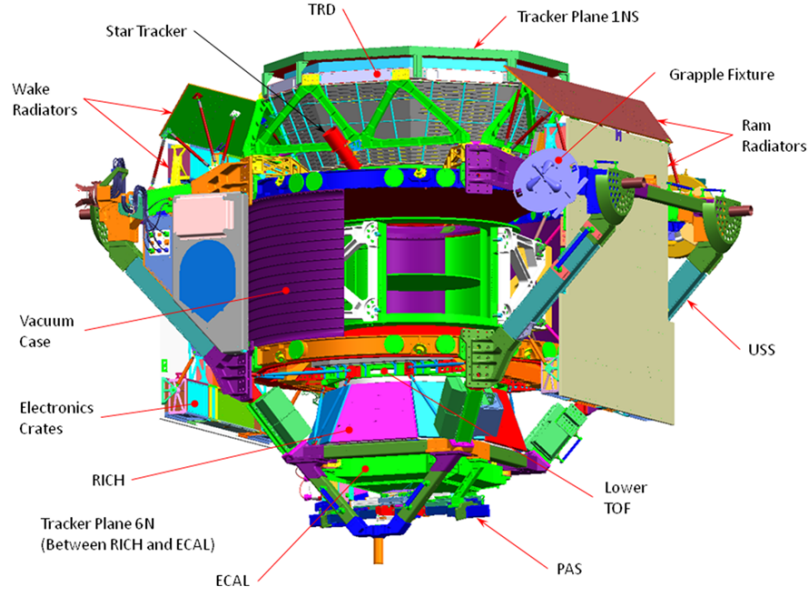


Figure 2.4 – Schematic view of AMS-02 [38].

### 2.2.1 Transition Radiation Detector

The TRD [39] is located on the top of AMS-02 between the external plane 1 of the tracker and the two first layers of the ToF. Its purpose is to distinguish between particles of the same charge and same energy but different masses, typically between electrons and positrons and protons or other nuclei. This subdetector principle is based on the detection of the transition radiation (TR) photon emitted when a charged particle crosses a boundary between two media with different dielectric constants, see Figure 2.5. Here, the two media are a fleece radiator and vacuum Straw tube proportional

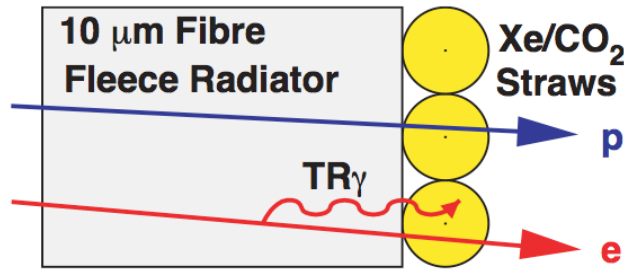


Figure 2.5 – Functioning principle of the TRD [39].

wire chambers filled with Xe/CO<sub>2</sub> gas detect the emitted X-rays. The TR emission depends on the mass, that is why we are able to distinguish between positrons and protons. The proton rejection for

the on-flight data at 90% positron efficiency is greater than  $10^2$  for rigidities below 600GV. The AMS-02 TRD is made of 328 modules composed of a 20mm fleece radiator of polyethylene/polypropylene followed by 16 6mm diameter straw tubes filled with Xe-CO<sub>2</sub> (20%-80%) gas mixture. Those modules are arranged in 20 layers with a diameter of 2m. To provide a 3D tracking the 4 first and the 4 last layers are oriented along the x-axis and the 12 layers in-between are oriented perpendicularly. Figure 2.6 shows the TRD before its integration.

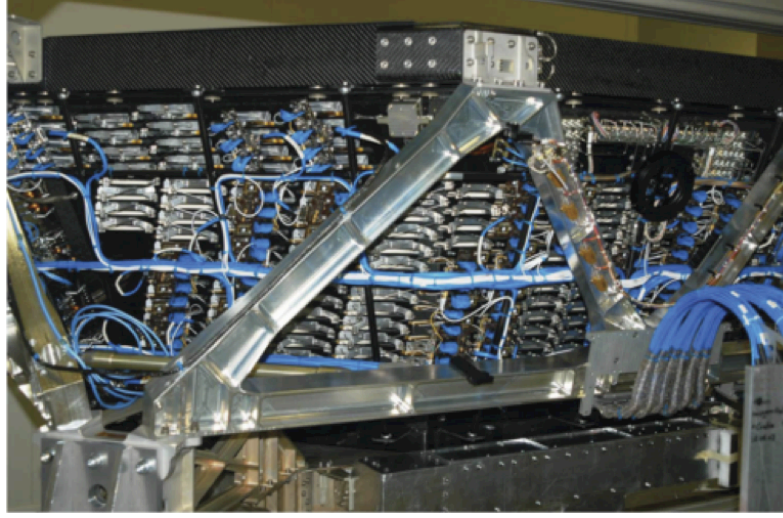


Figure 2.6 – *The TRD before its integration [28].*

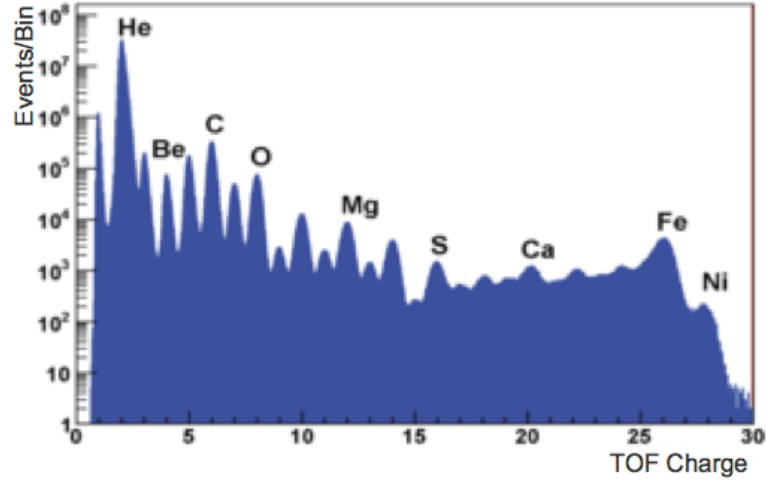
The TRD has its own thermal control system and also a complex gas control system to be sure that it keeps functioning nominally. The gas circuit contains two vessels : one of 5kg of CO<sub>2</sub> and one of 49kg of Xe. The leak rates measured in space permits a lifetime of the TRD gas circuit of approximately 20 years.

The presence of such an reliable and performant subdetector in AMS-02 is one of the major improvement that has been made with respect to previous cosmic ray detectors.

### 2.2.2 Time of Flight

The ToF system [40] is essential to AMS-02 since it provides the fast trigger to readout the electronics. It also measures the velocity ( $\beta$ ) and the charge of the particles crossing the detector. The ToF system uses plastic scintillator counters. The signal is measured by photo-multiplier tubes (PMTs) at the extremities of the scintillator paddles with a time resolution of approximately 80ps for  $Z = 2$  particles and 48ps for  $Z = 6$  particles. The charge is measured with the energy loss principle  $dE/dx$  providing a sufficient resolution to distinguish between nuclei up to the Nickel ( $Z = 28$ ) [41], see Figure 2.7. In this distribution the proton peak is suppressed by event selection.

The ToF is composed of four layers arranged in two planes. The first plane is located between the TRD and the plane 2 of the Tracker, the second plane is located between the last Inner Tracker plane and the RICH, they are both outside the magnet. These two planes are respectively named the Upper and Lower ToF, we can see in Figure 2.8 the two planes before their integration. To provide 3D tracking

Figure 2.7 – *ToF charge distribution [28].*

the two layers that constitute a plane are perpendicularly oriented. Each layer is composed of eight (or ten for the layer 3) 12cm wide plastic scintillator (polyvinyltoluene) paddles that overlap. Each paddle extremity is connected to either three or two PMTs (the Hamamatsu R5948 fine mesh model) through plexiglass light guides. The paddles and light guides are surrounded by a thin reflecting mylar foil then wrapped in a thick carbon fiber rigid shell.

Due to its fast response to a detected signal, the ToF is used to trigger the particles passing through AMS-02 and remains one of the most important system of the detector.

### 2.2.3 Silicon Tracker

The Silicon Tracker of AMS-02 [42] is a tracking system that, coupled with the permanent magnet surrounding its inner part, provides a measurement of the rigidity  $R=p/Z$  and also its sign allowing to distinguish between particles and antiparticles. To that is added a measurement of the charge due to the energy deposition in the silicon sensors. The position of a particle passing through the detector is measured by the nine layers of the Tracker. To provide 3D tracking the silicon sensors have double sided readout in orthogonal directions. The resolution of the detected position is about  $10\mu\text{m}$  for the bending direction ( $Y$ ), and about  $30\mu\text{m}$  in the non-bending direction ( $X$ ). The rigidity is measured by the curvature of the particle track that bends under the influence of the magnetic field provided by the permanent magnet through the well known Equation  $R = B \cdot \rho$  with  $B$  the magnetic field strength and  $\rho$  the curvature radius. The charge is reconstructed from the deposited energy through the Bethe-Block equation and provides a precise measurement. From the Bethe-Block equation we know that the deposited energy will be proportional to the charge of a particle through  $dE/dx \propto Z^2$ . For the silicon sensors the deposited energy comes from ionization of the sensor material. Due to the two sided sensors, the charge determination is very performant, this can be seen in the Figure 2.9. This excellent performance requires extensive calibration to equalize sensor response and provide a charge estimator independent of momentum, angle and position [43]. The charge peaks are clearly separated up to Silicon ( $Z = 14$ ) after that the separation power is lower but the Iron ( $Z = 26$ )



Figure 2.8 – *The two planes of the ToF before its integration [38].*

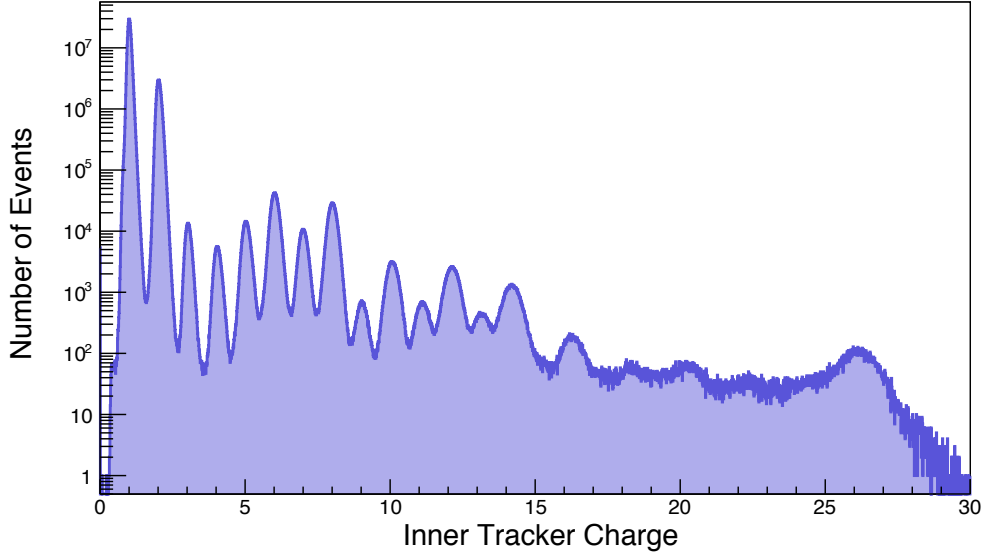


Figure 2.9 – Tracker charge distribution (from this analysis).

is still visible. Moreover, the contamination from neighboring charges is less than  $10^{-4}$  for charges below  $Z = 8$  at a 99% selection efficiency [?].

The Tracker is composed of six planes with nine layers. The two external planes support only one layer each and are located respectively above the TRD and between the RICH and the ECAL. The Inner part of the Tracker located inside the permanent magnet contains one layer on the upper plane but two layers on each of the three other planes. A schematic view of the configuration of the Tracker layers can be seen in Figure 2.10. Each layer is made of 16 to 26 ladders composed of double sided silicon sensors for a total of 192 ladders for 2264 sensors. The Silicon sensors are double sided micro-strip detectors composed of a  $300\mu\text{m}$  thick n-doped silicon bulk. At the top of the bulk there are  $\text{p}^+$ -doped strips and on the bottom of the bulk there are perpendicular  $\text{n}^+$ -doped strips with  $\text{p}^+$ -doped strips in-between to ensure strip insulation. A voltage is applied on the  $\text{n}^+$ -side and the sensors work at full depletion. A schematic view of the functioning of the sensors is shown in the Figure 2.11.

The Tracker has its own thermal control system, the TTCS (Tracker Thermal Control System) [44], to keep the Tracker temperature around  $10^\circ\text{C}$  at any time. It contains 142 temperature sensors and four pressure sensors added to 32 heaters to maintains an optimal temperature within  $1^\circ\text{C}$ . This system allows a good temperature stability over time for the planes inside the magnet bare.

The role of the permanent magnet surrounding the inner part of the tracker is to bend the direction of the track of a particle passing through it in order to get the associated rigidity. This magnet has been reutilized from the AMS-01 test flight. It is made of 64 sectors arranged in a cylindrical shape that delivers a dipole magnetic field of  $0.15\text{T}$  at the center. We defined the  $x$ -axis as the one along the magnetic field lines so the  $y$ -axis is the bending direction. By adding the two external layers, the level arm is increased and the curvature of the track can be measured with a Maximum Detectable Rigidity (MDR) up to  $3.2\text{TV}$  for Helium nuclei. This MDR sets the limit beyond which the rigidity cannot be measure with less than a 100% error.

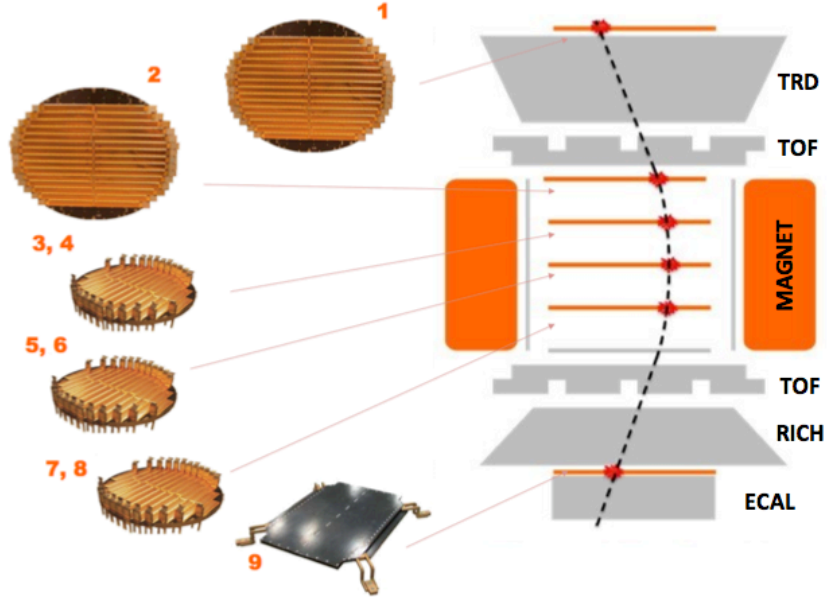


Figure 2.10 – *Schematic view of the Silicon Tracker with all the layers [38].*

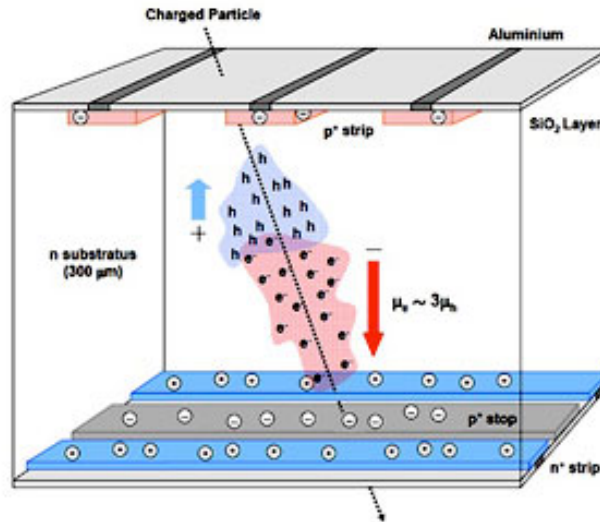


Figure 2.11 – *Schematic view of the silicon sensors of the Tracker [42].*



Temperature excursions of the outermost layers require dynamic alignment. Two methods have been developed to achieve an alignment accuracy compatible with the tracker resolution at any time during an orbit. The stability of the alignment of the nine layers has been checked over time and as an example the first layer shows an alignment stability of  $3\mu\text{m}$  over 5 months [45].

#### 2.2.4 Anti-Coincidence Counters

The ACC system [46] provides a rejection of particles that enter the detector from the side. The purpose of AMS-02 is to measure redundant information of a particle passing through it with almost all the subdetectors available, which means such a particle must cross the detector from the top to the bottom and not come from random directions. A schematic view of the functioning of the ACC system can be seen in Figure 2.12. The ACC measured efficiency is known to be better than

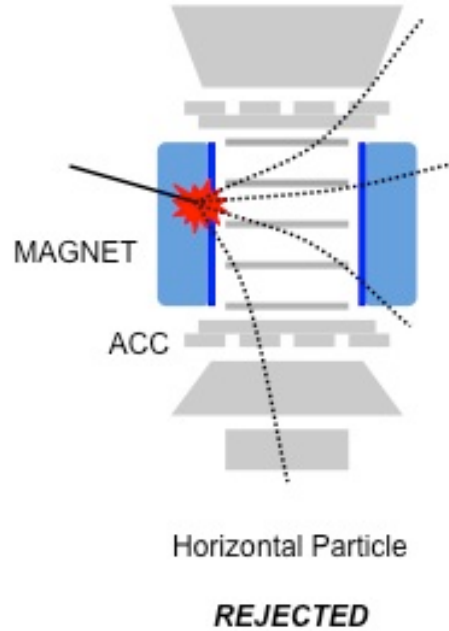


Figure 2.12 – *Functioning principle of the ACC [38].*

0.9999.

The ACC system is made of 16 scintillating paddles arranged cylindrically on the inner side of the metal case containing the inner part of the Tracker. In order to collect the emitted light, each scintillating paddle has embedded by wave-length shifter light guides connected to PMTs. There are 16 PMTs in total, eight on the top and eight on the bottom of the system. The ACC configuration system can be seen in Figure 2.13.

The ACC veto rejects particles entering the detector with the wrong direction but can also reject events that produce interactions in the detector, which will result in detecting light in several scintillating paddles. That is why this subdetector is mainly used in the trigger decisions.

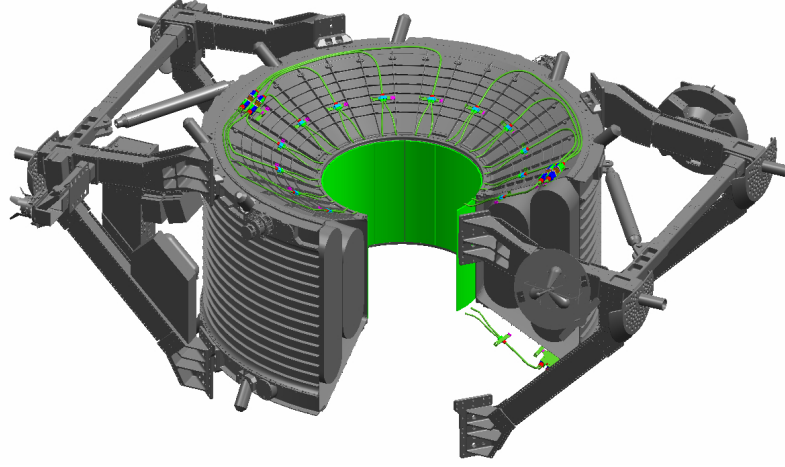


Figure 2.13 – Schematic view of the ACC system in green [47].

### 2.2.5 Ring Imaging Čerenkov Counter

The RICH [48] principle is based on the detection of the Čerenkov light emitted by a particle traversing it. Indeed, when a particle passes through a medium with its speed greater than the speed of light in this medium, a Čerenkov cone is created along the trajectory of this particle. With the opening angle of the cone ( $\theta$ ) the velocity ( $\beta$ ) of the particle can be extracted through the Equation :

$$\beta = 1 / \cos \theta n(\omega) \quad (2.1)$$

with  $n(\omega)$  the refraction index. Moreover, from the number of emitted photons ( $N_\gamma$ ) we can determine the charge of the particle ( $Z$ ) using the Equation :

$$\frac{dN_\gamma^2}{d\omega dx} = \alpha Z^2 \sin^2 \theta \quad (2.2)$$

where  $\alpha = 1/137$  the fine structure constant. The measurement of the  $\beta$  can be easily linked to the mass as well providing a precise measurement of it. The RICH velocity resolution is  $\Delta\beta/\beta = 1.4 \cdot 10^{-3}$  for  $Z = 1$  and goes to  $\Delta\beta/\beta \approx 10^{-4}$  for higher charged nuclei [49]. Plus, it provides charge identification up to Iron ( $Z = 26$ ).

The RICH, located between the Lower ToF and the ECAL, is made of 3 different parts : a radiator plane, a conical mirror and a photon detection plane. This configuration can be seen in the Figure 2.14. The radiator plane is made of two regions: a center part composed of a 0.5cm thick square of sodium fluoride (NaF) with a high refractive index ( $n \approx 1.33$ ) and a surrounded part composed of a 2.5cm thick silica aerogel with a lower refractive index ( $n \approx 1.05$ ). The photon detection plane has a rectangular hole in the middle ( $64 \times 64 \text{ cm}^2$ ) to match the ECAL acceptance and avoid a too large amount of material before the last subdetector. It is composed of 680 PMTs coupled to pyramidal light guides to increase the efficiency of light collection.



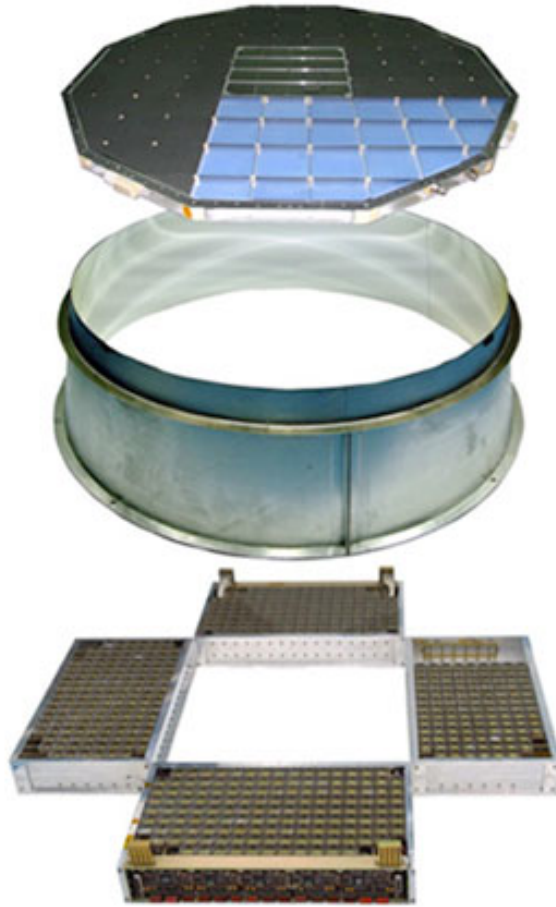


Figure 2.14 – Exploded view of the RICH showing the radiation plane (top), the conical mirror (middle) and the PMT array (bottom) [38].

### 2.2.6 Electromagnetic Calorimeter

The ECAL [50] is used, as the TRD, to measure energy and direction of electromagnetic showers and to distinguish from hadronic ones. This separation is made possible by the 3D reconstruction of electromagnetic showers that develop inside the calorimeter. When leptons enter the ECAL they interact with the lead material by producing electromagnetic showers resulting in a succession of bremsstrahlung photons and electron-positron pairs that are detected by this energy deposition. The total calorimeter thickness corresponds to 17 radiation length which means that the showers produced by electrons and photons are fully contained in the calorimeter and the deposited energy is directly proportional to the energy of the entering particle. The resolution of the energy measurement was extracted from beam test data and has been parametrized by :

$$\frac{\sigma(E)}{E} = \frac{(11.9 \pm 0.4)\%}{\sqrt{E(\text{GeV})}} + (2.8 \pm 0.1)\% \quad (2.3)$$

The ECAL also allows a proton rejection at 90%  $e^+$  efficiency of the order of  $10^4$ .

The ECAL is made of nine super-layers. Each super-layer is 18.5mm thick and is composed of a succession of 1mm thick lead foils and layers of 1mm diameter scintillating fibers glued together epoxy resin. These scintillating fibers are connected to PMTs for a total of 1296 read-out elements and 324 PMTs. To provide a 3D tracking the fibers run alternatively along the  $x$ -axis and along the  $y$ -axis. A final configuration of the ECAL is shown in Figure 2.15 before its integration.

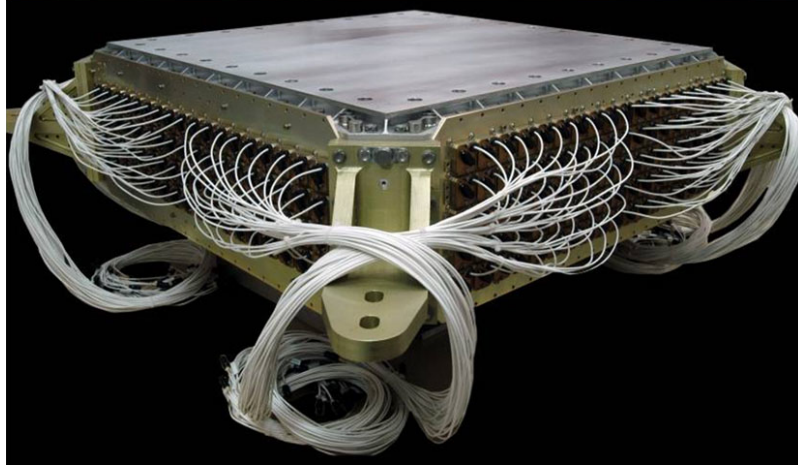


Figure 2.15 – View of the ECAL before its integration (credit Nasa).

## 2.3 Data Taking

Now that we have seen all the details concerning the different part that constitute AMS-02, we can describe how the data acquisition is organized and how the data are stored. One of the most important challenges that the detector faced was the data acquisition and the organization in collecting them from the many subsystems. In a first place we introduce the event definition : an event

represents a particle triggered by the detector for which all the information coming from the different subdetectors are stored. The data are structured in a certain amount of events named a run, each run represent a collection of events for more or less an acquisition time of 23 minutes such that there are four runs per orbit. A calibration of several subdetector is performed every two runs. A total of 227 300 channels are read-out by the electronics of the detector which leads to a raw data rate over 7Gbit/s [37]. The electronics must reduced this event size to the allocated downlink data rate of 2MBit/s. In the following we are going to describe the different triggers that exists for AMS-02 and the Data Acquisition system (DAQ) that collects all the signals from the subdetectors and sorts them into usable data events.

### 2.3.1 Trigger

When a particle passes through detector, the decision of keeping the information related to this particle needs to be taken quickly. The different kind of triggers of the AMS-02 are here to evaluate quickly the particle characteristics and to take the decision to start the data acquisition or not. These triggers use combined information from ToF, ACC and ECAL [51]. The ToF and ACC signals are combined in an AND or OR gate depending on which trigger is used. For the ECAL, an AND or OR gate is used between the different crate signals. In total, there are three different triggers : the Fast Trigger, the Level1 trigger and the Level3 trigger. These three different triggers represent three different stages of a complex tree architecture which means that to validate a trigger the precedent one must be validated as well. For data acquisition, only the Fast and the Level1 triggers are used.

The Fast trigger (FT) is the first trigger activated and results in a fast decision whether to activate the Level1 trigger or not. It only uses information from the ToF and the ECAL. The time required for the FT decision is 40ns. There are three kind of FT:

- the FTC that uses two types of charged particle signals from the ToF that correspond to different combination of ToF paddles;
- the FTZ that uses large  $Z$  particle signals from ToF, which means it concerns slow and heavy particles;
- the FTE that uses the energy signal from the ECAL and concerns neutral particles detected in the ECAL.

The Level1 trigger follows the FT and requires  $1\mu\text{s}$  decision time. There are six different sub-triggers that uses different signals and will generate the Level1 trigger.

### 2.3.2 Data Acquisition System

The DAQ system [43] is activated after a particle has been triggered by one of the previously seen triggers. Its main purpose is to collect signals from the different subdetectors, reduce the additional dead time and also reduce the size of the collected data.

The DAQ architecture adopts a tree-like structure. Each subdetector has a dedicated Front End electronics (FE) that regroups all its read-out channels. Connected to these FE there are the Data Reduction (DR) nodes that collect the signals from all the channels, there are a total of 264 xDR nodes (x stands for the subdetector considered : U is for the TRD, S for the ToF and the ACC, E for the ECAL, T for the Tracker, R for the RICH). The xDR are then connected to 28 JINF. At the same

time eight SDR collect the data from the triggers as well as two JLV1 nodes. At the end, the data are collected by four JINJ nodes from the JINF, the SDR and the LVL1 nodes. In order to minimize the dead-time, the event information is buffered at each level of the tree architecture. For redundancy, the nodes and links are replicated at each level. The architecture can be seen in Figure 2.16.

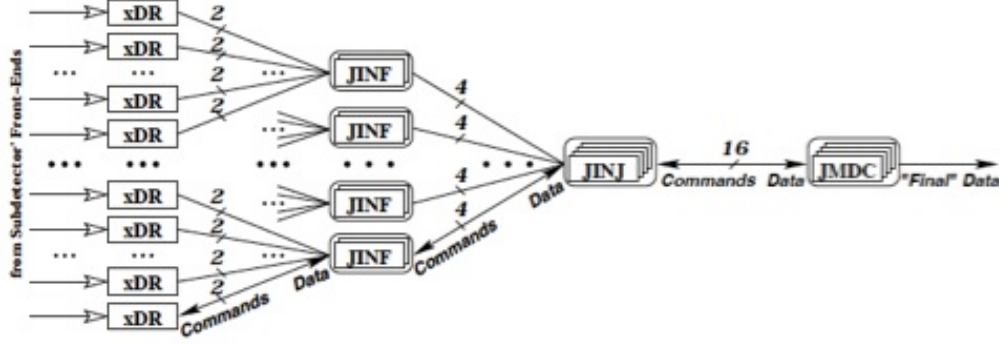


Figure 2.16 – Schematic representation of the architecture of the DAQ system [38].

The main computers on-board AMS-02 are the four JMDCs. As seen in the beginning of this chapter these are the ones that transfer data to the ground. Once the data are buffered in the JINJ, they are collected by the JMDC to be sent. The JMDCs provides also monitoring of the whole detector. Commands can be received from the ground.

## 2.4 Monte Carlo Simulations

As for many experiments, Monte Carlo (MC) simulations has been made for AMS-02. Indeed, such simulations are needed to understand better the detector and the in-flight data. The AMS-02 MC simulation is based on a precise definition of the detector taking into account, in the most detailed way possible, the composition of the detector for the geometrical dimensions as much as material composition. The standard GEANT package [52] is used to simulate the interaction processes that occur in the material of the detector.

The particles simulated by the MC are generated on a square of a 3.9m side located above the detector. The charge of nuclei is selected as well as the momentum range. One important thing to notice is that the generated spectrum is flat with momentum so does not reproduced a power law spectrum. To change the shape of the generated spectrum reweighting must be used.

These MC simulations are constantly produced by the AMS-02 collaboration for a large choice of nuclei and momentum ranges and improved by cross-checking with in-flight data to provide the best version possible.

## Chapter 3

# HELIUM ANALYSIS

In this chapter, we will go through the details of the helium analysis performed for this work which leads us to compute a helium flux that will be compared to one of the most precise measurement ever reached with a space based experiment [1]. A very precise definition of what has been done in this analysis will be provided.

In order to end up with a relevant measurement of a flux, several ingredients must be computed using the following Equation :

$$\phi_{He} = \frac{N_{He}}{\Delta T \cdot A_{geometrical} \cdot \epsilon_{detector} \cdot \Delta R} \quad (3.1)$$

with  $N_{He}$  the number of detected helium nuclei,  $\Delta T$  the exposure time,  $A_{geometrical}$  the geometrical acceptance of the detector,  $\epsilon_{detector}$  the efficiency of the detector and  $\Delta R$  the rigidity range.

The first thing to do is the selection of a good sample of helium events, the definition of such events will be described in the first section. The second section will introduce the calculation of the exposure time which is a key point of any flux measurement. The third section will give all the details about the Efficiencies. We will then describe the study of the survival probability in the external layers of the tracker in the forth section. In the fifth section we will talk about the acceptance of our detector. The sixth section will focus on the unfolding procedure, such a procedure as an important impact when studying a power law spectrum such as the cosmic ray spectrum. The last section will be on the different systematic errors studied for this analysis.

### 3.1 Sample Selection

The selection process of well reconstructed helium nuclei starts with raw data that results from triggered events. These raw events go through a series of cuts in order to select the good ones. Then the charge of each of the selected tracks is checked to select helium nuclei with charge  $Z = 2$ . This process is made by analysing event by event in a loop and checking different information that is relevant to determine the quality of their reconstruction. In this analysis only the silicon tracker (tracker) and the time of flight (ToF) are going to be used to select both the quality of the tracks and their charge.

### 3.1.1 Data Set

For this analysis we decided to use the same data set that the one used by the collaboration for the helium spectrum publication. The data extends from run 1305853512 up to run 1385483969 which represents 30 months of data taking. The reconstruction version of the data is the B950 pass6. The Monte Carlo (MC) simulation used for this analysis is the B1036  $^4\text{He}$  production. As seen in Section 2.4, the generated rigidity spectrum is flat and extends from 1GV to 8000GV. The simulation is layer 1 and layer 9 focused and the ms scaling is of 15%.

### 3.1.2 Pre-selection

The first set of cuts, which we call pre-selection, consists in more general cuts which do not depend on the type of analysis that is performed. This selection is focused on the operational status of the detector and what we need to check to be sure that we are in a good operational configuration. The first thing to check is the number of the run. The collaboration provides a list of what is called *badruns*. Those *badruns* were determined by bad operating conditions of one or several of the different subdetectors. We cut out of the analysis the runs before 1306967023 and between 1307125541 and 1307218054, which correspond to runs from the first days when the detector went operational in space. We also cut out the run 1321198167 that corresponds to a bad operating conditions for ECAL.

Now we can enter the event by event loop. The first requirement is to have at least one DAQ event which means that the Data Acquisition System was operational for this event and stored all the information from the different subdetectors related to it.

As seen in the previous chapter, we have different kind of triggers with AMS-02. The next step in the pre-selection consists in selecting events with one LVL1 trigger with a physics tag which will insure the selection of a physical event. After that, we require at least one reconstructed particle.

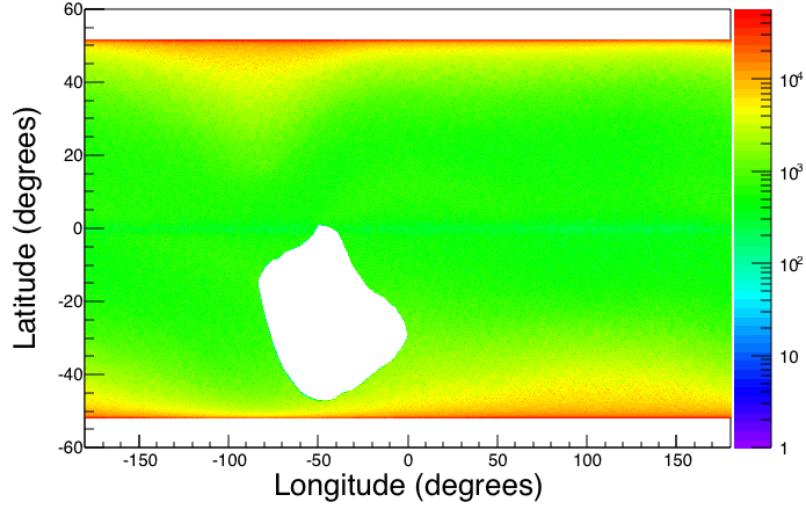
In order to be more efficient and precise with the selection, we are going to use a reconstructed object provided by the collaboration that allows us to switch from an event by event loop to a time based loop (second by second). This process makes easier the selection on the ISS conditions. First of all, we want to be sure that the JMDC lifetime is sufficient so we ask it to be greater than 0.5. Then we cut on the AMS zenith angle and accept only seconds when this angle is lower than 40 degrees. The next cut concerns the quality of the second which is determined by the collaboration. Moreover, the seconds when the detector was inside the South Atlantic Anomaly are cut out, the SAA boundaries being geographically determined as shown in the Figure 3.1. The last selection is on the difference between the two alignments the collaboration provides for the external layers, allowing only  $35\mu\text{m}$  maximum of difference for the Layer 1 and  $45\mu\text{m}$  for the Layer 9 in the bending direction.

After this step we have selected approximately  $4.4 \cdot 10^9$  events. We can now move to a specified selection for the different subdetectors used in this analysis namely the ToF and the tracker.

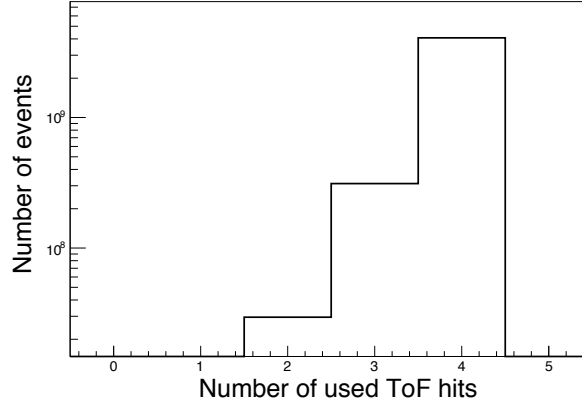
### 3.1.3 ToF Selection

As seen in the previous chapter, the time of flight counters are providing us a precise measurement of the  $\beta$  of the particle as well as an estimation of the charge. Consequently, we must select events that will be well reconstructed from the point of view of the ToF.

First, we require only one cluster on each of the four planes of the ToF. One cluster in each plane will

Figure 3.1 – *Coordinates of the preselected events.*

ensure to have enough charge measurements to separate the Upper ToF charge estimator from the Lower ToF charge estimator. The *only one* condition rules out all event that could contain several particles at the same time in AMS-02 or the interactions of a particle with the material of the detector. In Figure 3.2 the number of used hit for the ToF events is shown, we can see that we cut only about

Figure 3.2 – *Number of used hit for ToF events.*

6% of the total statistic.

The next cut concerns the  $\beta$  measurement. We want it to be  $\beta > 0.3$ . The main reason of such a cut is to avoid up-going particles, i.e. particles that come from the bottom of the detector. Such particles are usually secondaries coming from Earth or primaries that interact with the ISS. The 0.3 limit is here to reject bad reconstructed  $\beta$  events and very low energy particles. The Figure 3.3 show the

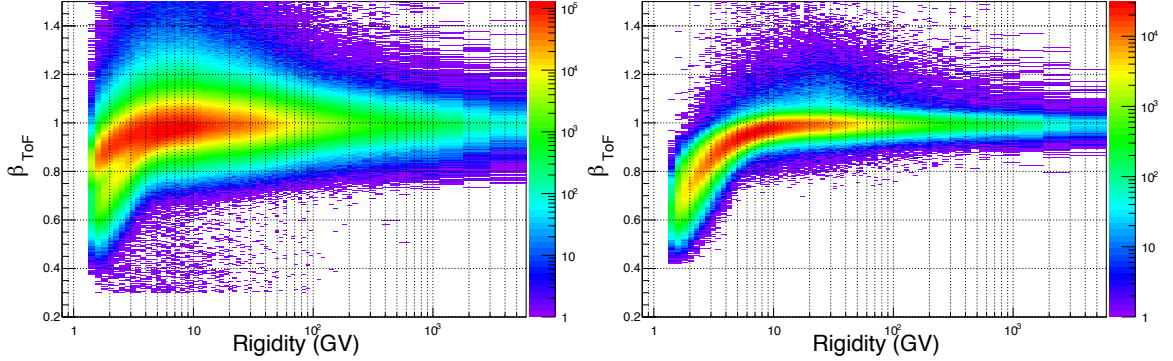


Figure 3.3 –  $\beta_{\text{ToF}}$  distribution versus the rigidity for both all charges together (left) and helium only (right).

distribution of the  $\beta$  of the selected events with respect to the rigidity from the tracker both without any charge selected and with the charge  $Z = 2$  selected.

To be sure that no selected cluster is a result of another particle or any interaction, we require that less than or equal to four ToF clusters being in a time window of 10ns around the general event time for the upper ToF and 4ns for the lower ToF. Since to compute the  $\beta$  the time is needed, we need to be sure that all the clusters used to reconstruct the track correspond to the currently studied particle. The last cut concerns the way the event is reconstructed by the ToF and which detectors are used to reconstruct the track. Only the tracker and the ToF are requested to reconstruct the ToF object.

After the ToF selection we have approximately  $3.2 \cdot 10^9$  events left. The next step consists in using the last subdetector relevant for this analysis which is the tracker.

### 3.1.4 Tracker Selection

As well as for the ToF, the tracker provides accurate measurements of both the rigidity and the charge, therefore, the selection will concern both of them. We must make a distinction between the inner tracker, made of the layers 2 to 8 and the external layers, the layer 1(L1) and the layer 9(L9). The separation of these entities is important for the two measured characteristics. Every event is going to pass through a series of five cuts that will ensure the selection of a well reconstructed track. The first cut concern the inner tracker pattern of the hits. We require to have at least one hit on the Y side (bending plane) on each plane of the inner tracker, which means that we will have one hit on the layer 2, at least one hit on either the layer 3 or 4, one hit on either the layer 5 or 6 and one hit on either the layer 7 or 8. We required a hit on the Y side because we want to be sure to have enough points along the track to have a good reconstruction and consequently a good estimation of the rigidity.

The next cut concerns the quality of the reconstruction of the charge. We ask at least three hits with both X and Y side among the already selected hits. Adding the X side will ensure to have a precise measurement of the charge, this side having a larger dynamic range than the other. These X and Y side hits must be out of geometrical regions known for a bad reconstruction of the charge. We can see



the distribution of the number of  $X$  and  $Y$  side hits in Figure 3.4.

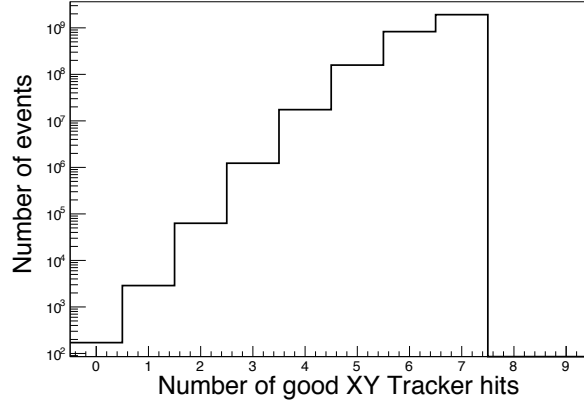


Figure 3.4 – *Number of  $X$  and  $Y$  sided hits with good status for the charge reconstruction.*

Then we select the external pattern. For this analysis, we require a full span pattern, which means that the track must have a hit on both L1 and L9. As previously, these hits must include both  $X$  and  $Y$  sides to have, at the same time, the best possible reconstruction for the track and for the charge. Other analysis from the collaboration are performed in a inner+L1 pattern, meaning that only a hit on the L1 is required, this allows to have more statistics, but the Maximum Detectable Rigidity (MDR) is lower than for the full span pattern. Thus, the choice of a full span pattern enables to reach higher rigidities for the helium flux.

As seen in the first chapter, when studying near Earth spatial environment an important effect to take into account is the geomagnetic cutoff. Based on the rigidity of the event, we need to determine whether the particle is a primary or a secondary cosmic ray. To this end, we cut all the events with a rigidity below the maximum rigidity cutoff calculated by the reconstruction. This maximum rigidity cutoff is computed from a backtracing of the event and uses the International Geomagnetic Reference Field (IGRF, the 11<sup>th</sup> generation) to model the field in which the particle evolves. A field of view of 40sr is applied here. Figure 3.5 shows the distribution of the maximum rigidity cutoff. As expected it never excesses 50GV.

The last characteristic checked is related to the quality of the reconstructed track. For every event, the track is fitted with several algorithms in different patterns, including or not the external layers. The choice has been made to cut events that have a  $\chi^2 > 10$  of the fitted track for the  $Y$  projection for both inner only pattern and full span pattern. Figure 3.6 shows the distribution of the  $\chi^2$  for the two patterns, before the cut.

After this series of cuts we end up with reconstructed tracks of a good quality. In terms of the charge, the selection made on the hits of the track will ensure a good quality of the measurement. Let's now move to the last selection, the charge selection.

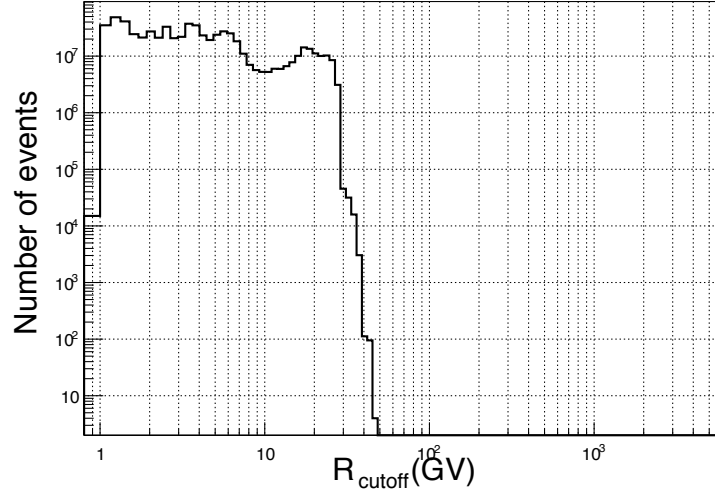


Figure 3.5 – *Distribution of the maximum rigidity cutoff.*

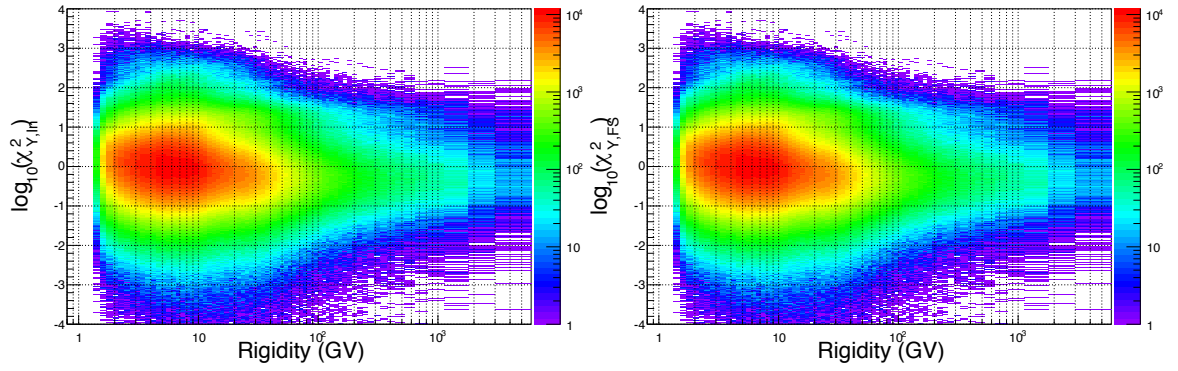


Figure 3.6 –  $\chi^2$  distribution for the  $Y$  side with respect to the rigidity, for both inner only (left) and full span (right) patterns.

### 3.1.5 Charge Selection

The selection of the charge is what comes at the end of the analysis steps when the quality selections has been made, when we know that we have relevant information about the rigidity, the  $\beta$  and the charge. The more estimators we have for the charge, the more redundant will be the measurement and the more reliable will be the selection. Therefore, five charge estimators are used in this analysis namely inner tracker, upper ToF, lower ToF, L1 and L9.

The inner tracker estimator is the one with the best resolution. It is defined as the truncated mean of all charge measurements, combined from calibrated measurement on all planes and sides [43]. When looking at Figure 3.7 one can see that the separation between the peaks of every charge is well defined,

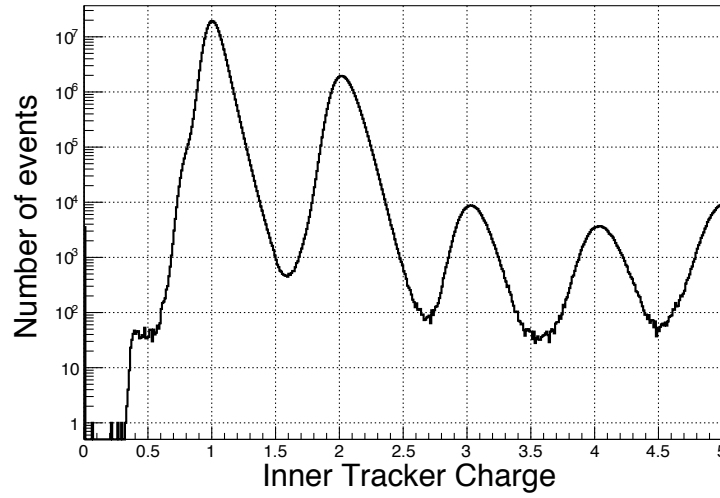


Figure 3.7 – *Inner tracker charge distribution.*

this means that we will have very few contamination from the neighboring charges. The energy deposition distribution in the silicon sensors is described by a Landau that we need to convolute with a Gaussian when looking at the ADC signals from which the charge is directly calculated. The selection range is  $1.7 < Q_{InnerTracker} < 2.5$ . It is asymmetric because of the tail of the Landau distribution towards high values. We can have such a narrow range due to the good definition of the peak, most of the helium events will be located in the range and the contamination will be very low.

The ToF has been separated in two charge estimators, the upper ToF that regroups the two upper layers, and the lower ToF that regroups the two lower layers. The charge is estimated as the mean of the two charge estimations coming from each layer. From the Figures 3.8 one can conclude that the distribution of the charge is not as good as for the inner tracker. Therefore we can have more contamination from neighboring charges, especially from the proton ( $Z = 1$ ). To avoid such an effect, but to keep as many helium candidates as possible, we applied the following cuts :  $Q_{upperToF} > 1.25$  and  $Q_{lowerToF} > 1.25$ .

For what concerns the external layers, the distributions of the charge for L1 and for L9 are shown in Figure 3.9. Since only one charge measurement is used for each estimator the distribution is not as precise as the inner tracker one. Consequently, a wider selection range is used and events are selected only if  $1.6 < Q_{L1} < 2.9$  and if  $1.6 < Q_{L9} < 2.9$ .

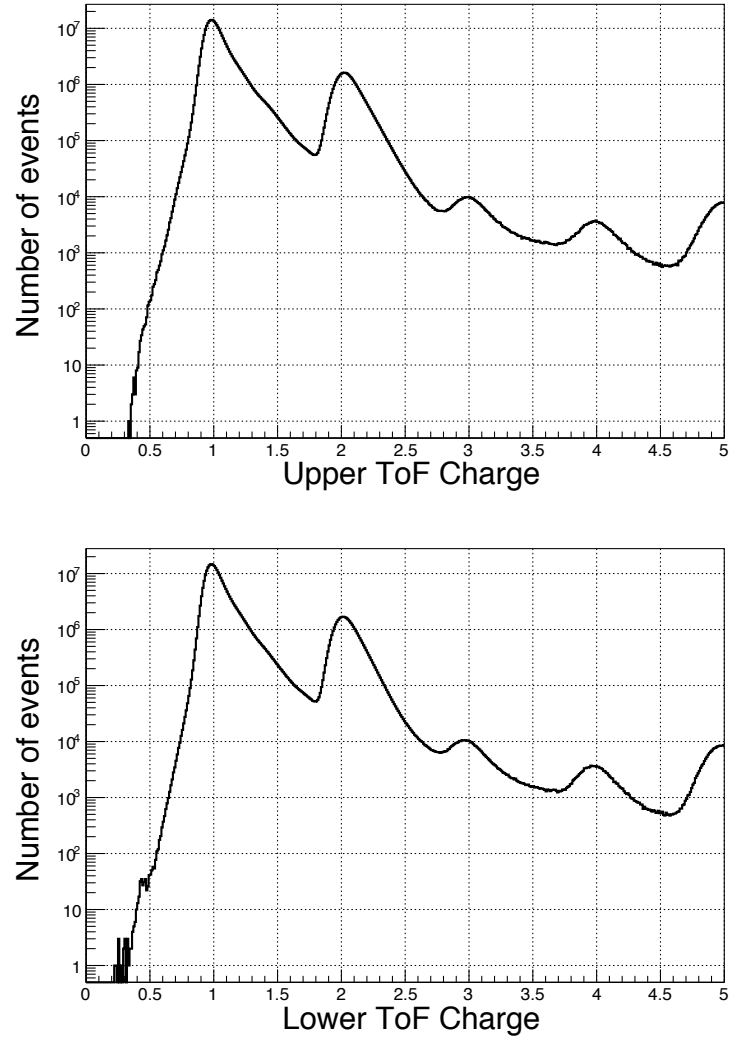


Figure 3.8 – *Upper ToF (up) and lower ToF (down) charge distributions.*

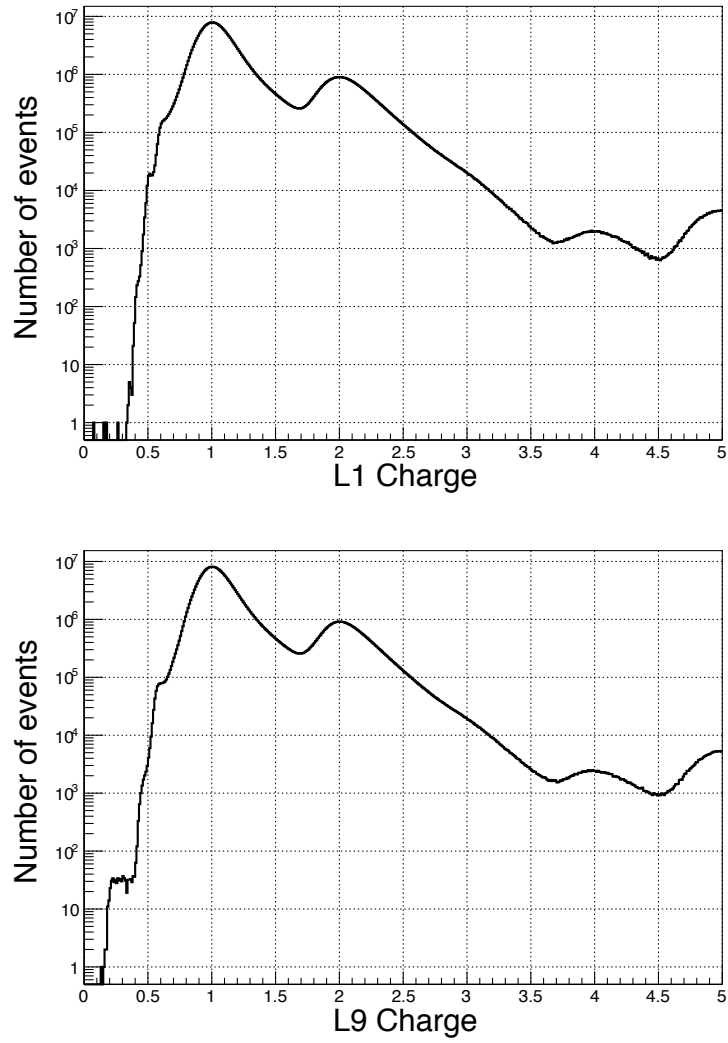


Figure 3.9 – *L1 (up) and L9 (down) charge distribution.*

All these charge selections are defined in order to, on one hand, minimize the contamination coming mostly from proton ( $Z = 1$ ) but also a little bit from lithium ( $Z = 3$ ), on the other hand, maximize the statistics. Moreover, the efficiency of such a charge selection will be introduced when talking about the efficiencies of both the ToF and the tracker in one of the next sections. The higher the efficiency of the selection, the lower is the influence of its systematics on the final result.

At the end of this step we are almost sure that the events selected are helium nuclei. The final statistics of helium is  $3.6 \cdot 10^7$  events. Figure 3.10 represents the number of selected events with

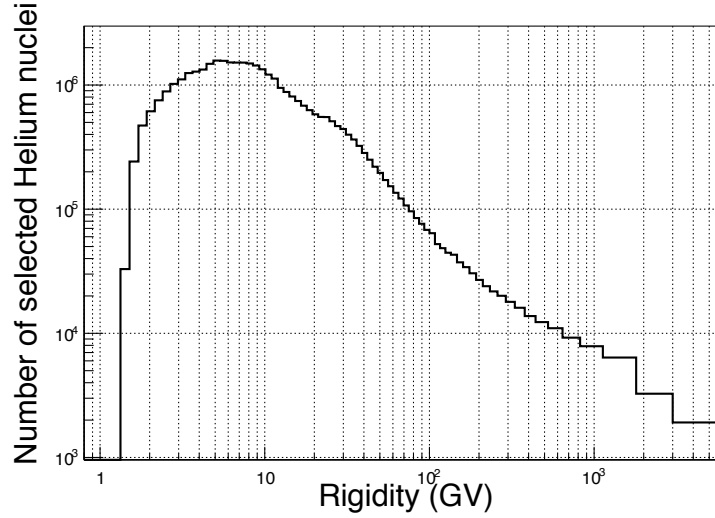


Figure 3.10 – *Number of events selected at the end of the analysis with charge  $Z = 2$ .*

respect to the tracker rigidity. The binning is the same as the one used by the AMS-02 collaboration in the published papers for proton and helium fluxes. It is a changing binning width adapted to the resolution of the rigidity measurement. There are 74 bins from  $R = 0.8\text{GV}$  to  $R = 3\text{TV}$ .

The number of events per rigidity bin is the first element needed to compute the helium flux. Now we can move on to the next steps which will bring the other required ingredients.

### 3.2 Exposure Time

The first and one of the most important element to compute when trying to measure a flux is the exposure time. It represents the time range, in seconds, when the detector is collecting data and operating properly. Given that the flux will be measured in rigidity, the exposure time will be computed in rigidity as well.

In AMS analysis, detector position, altitude and operational conditions are recorded on a second-to-second time scale. But first, let's define what kind of seconds are going to be selected to compute the exposure time. In order to be consistent with what has been done with the selection referred in the previous Chapter, the same pre-selection is applied. However we do not want to cut on the DAQ, the trigger or the number of reconstructed particles.

As well as for the selection of events, the geomagnetic rigidity cutoff must be taken into account here. For instance, in the lowest rigidity bins if, during a certain period of time, it is impossible for the detector to see any primary helium nuclei given its orientation in the Earth geomagnetic field, this period cannot be added to the exposure time. To do so, the maximum rigidity cutoff previously used is applied to cut the non wanted seconds, with the same field of view (i.e. 40sr) to be consistent with the selected events.

Figure 3.11 represents the exposure time in bins of rigidity. The rise that appears from the low-

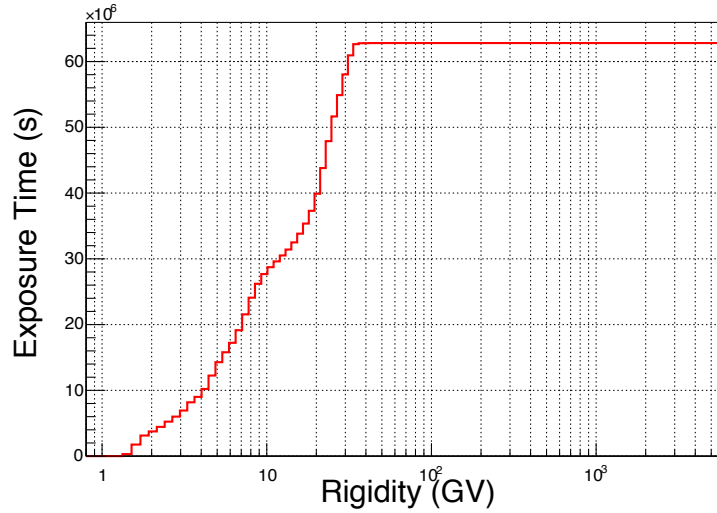


Figure 3.11 – *Exposure time with respect to the rigidity.*

est rigidities to around 20GV represents the effects of the geomagnetic cutoff. It is exactly what we expect because primary particles coming toward Earth with such a low rigidity will most of the time be trapped in the geomagnetic field around Earth as explained in more details in the first chapter.

Once the exposure time is computed, we can go through the rest of the steps moving on to the efficiencies and the acceptance of the detector.

### 3.3 Efficiencies

When trying to compute a flux from any detector one needs to take into consideration an important factor: the efficiency of such a detector and of the cuts applied. Indeed, we need to be sure that all the cuts applied to select helium nuclei do not introduce any important bias. In this section, we are going to introduce five different efficiencies related to the selection process : the trigger efficiency, the ToF efficiency, the inner tracker efficiency and the external layers efficiencies. However, these calculated efficiencies will not be used directly to compute the flux because we will include them into the acceptance. Instead, we will use them to get the acceptance corrected from the difference between data and MC efficiency results through the ratio  $\frac{\epsilon_{data}}{\epsilon_{MC}}$ . These differences will also induce systematic errors. All of this will be detailed in the next sections.

In a general way, an efficiency is computed with two quantities namely the total number of events passing through a detector and the number of events selected at the end of the selection process. The efficiency is then calculated with the following Equation :

$$\epsilon_{detector} = \frac{N_{selected}}{N_{total}} \quad (3.2)$$

Nevertheless, even though this equation appears to be simple, for this analysis calculating the efficiencies can be slightly more complicated and we must be careful especially about the samples we use for the different subdetectors.

### 3.3.1 Trigger Efficiency

As seen previously, the trigger used for this analysis is the Level1 trigger from data acquisition. Inefficiencies of the trigger are measured using a pre-scaled sample of unbiased trigger events. Thereby, the trigger efficiency is computed as follows :

$$\epsilon_{Trig} = \frac{N_{phy}}{N_{phy} + 100 \cdot N_{unbToF}} \quad (3.3)$$

This "100" factor is here because those ToF unbiased events are pre-scaled to  $\frac{1}{100}$ .

The trigger efficiency can be seen in Figure 3.12. The efficiency starts to go down around 2GV but

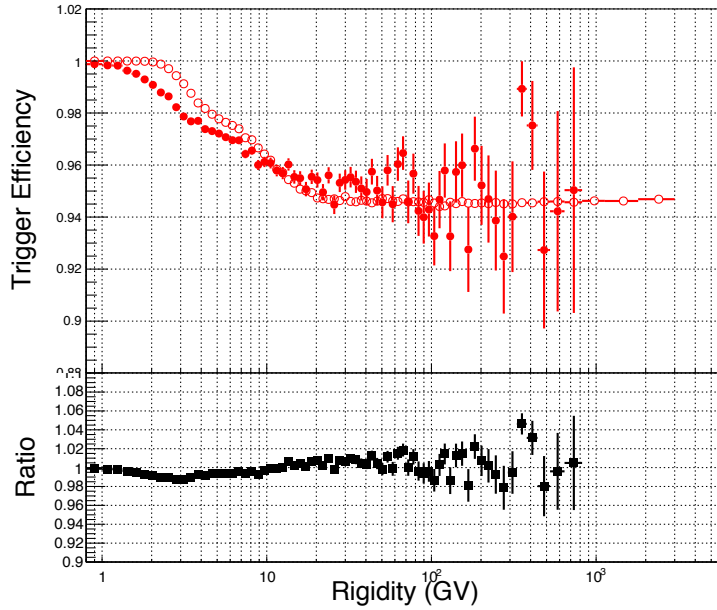


Figure 3.12 – *Trigger efficiencies for data (full circle) and MC (open circle) samples plus the ratio of the two.*

becomes flat again after 20GV both for the data and MC. However, the efficiencies stay high and the



are compatible between data and MC within a few % for the whole rigidity range.

### 3.3.2 ToF Efficiency

The ToF efficiency resumes the four cuts related to the ToF selection as well as the charge selection by both the upper ToF and the lower ToF estimators. The equation 3.1 is used. The sample needs to be unbiased from a ToF point of view. Therefore the selected particles for this sample include only the pre-selection cuts and the tracker selection cuts. The charge is selected with the unbiased inner tracker and external layers only.

Figure 3.13 represents the efficiencies of the cumulative successive cuts for the data and for the MC

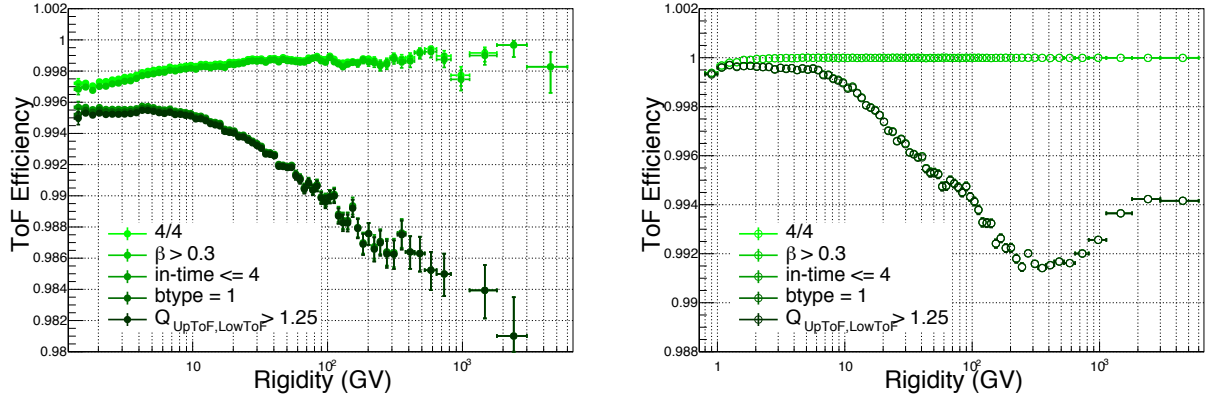


Figure 3.13 – Efficiencies of the ToF successive cumulative cuts for both data (left) and MC (right) samples.

samples. Based on the value of the efficiencies, we can conclude that none of the cuts have a significant impact on the ToF efficiency. However, we can see that the cut that introduces slightly more bias in rigidity is the requirement of in-time clusters for both data and MC. This inefficiency increases with the rigidity which can be understood because the higher is the rigidity, the more background we get in the detector that can lead to more clusters in the ToF layers which will not be in-time. Nevertheless, the effect is quite small since the efficiency never goes below 0.98. At the end, the efficiency for the ToF is close to 1 and doesn't depend strongly on the rigidity as we can see on Figure 3.14. Once again, the data and the MC results are very compatible within less than 1% up to the highest rigidities.

### 3.3.3 Inner Tracker Efficiency

In the same way than for the ToF, the inner tracker efficiency characterizes the cuts as well as the charge selection with the inner tracker. The sample here needs to be unbiased from a tracker point of view which must be carefully taken into account especially because the efficiency is given as a function of rigidity.

Since the tracker cannot be used to determine the rigidity of an event, other detectors must be

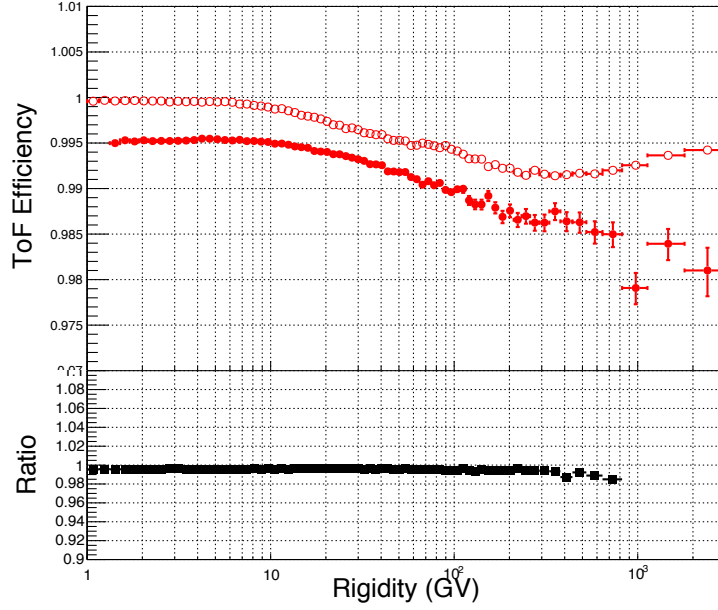


Figure 3.14 – ToF efficiencies for data (full circle) and MC (open circle) samples plus the ratio of the two.

considered. The first that can be used is the ToF since  $\beta$  allows to measure the rigidity:

$$R_\beta = \frac{m_{He}}{2\sqrt{\frac{1}{\beta^2} - 1}} \quad (3.4)$$

with the mass of helium taken as the mass of  $^4\text{He}$ :  $m_{He} = 3.727\text{GeV}$ . The problem with this method is that the  $\beta$  resolution does not allow to reconstruct high rigidities that way and we can deduce from Figure 3.15 that after few GV it cannot be used anymore. We set the limit at 5.9GV.

For intermediary rigidities the best estimator is the geomagnetic cutoff. Indeed, in between few GV and around 20GV, given the shape of the flux, a particle will have a rigidity close to the geomagnetic cutoff. Thereby the maximum cutoff rigidity is used to estimate the true rigidity of the events. Figure 3.16 shows the comparison of this rigidity and the tracker one that justifies the use of it until 19.5GV. Above 19.5GV, it becomes complicated to estimate the rigidity without the tracker. In theory, the ECAL could estimate the rigidity. But this estimator must be carefully considered and we are only going to use it as a check for the higher rigidities compared to the extrapolation of the previous estimators. Thus, the results from the rigidity calculated with the ECAL are shown but will never be used for the parametrization of the efficiencies. The parametrization is extrapolated above 19.5GV. On an other hand, for the MC sample the rigidity from the ToF  $\beta$  is used until 5.9GV but after that only the generated rigidity can be used. If we take a look at the efficiencies of the successive selection cuts in Figure 3.17, we can see that they show no dramatic dependence with the rigidity for both data and MC. However, the cut on the  $\chi^2_{Y,inner}$  seems to be the one that is the most inefficient, especially at low rigidity which is understandable since the tracks are the more curved. The final efficiency

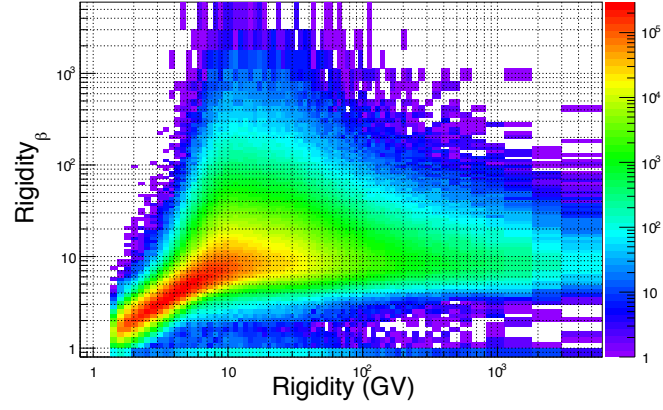


Figure 3.15 – *Distribution of the rigidity computed from the  $\beta$  with respect to the tracker rigidity.*

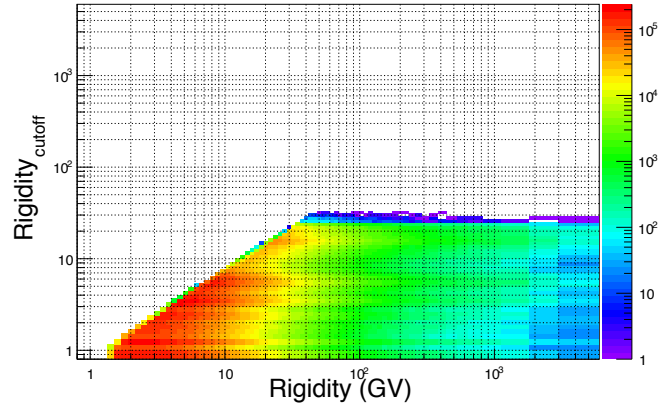


Figure 3.16 – *Distribution of the maximum cutoff rigidity with respect to the tracker rigidity.*

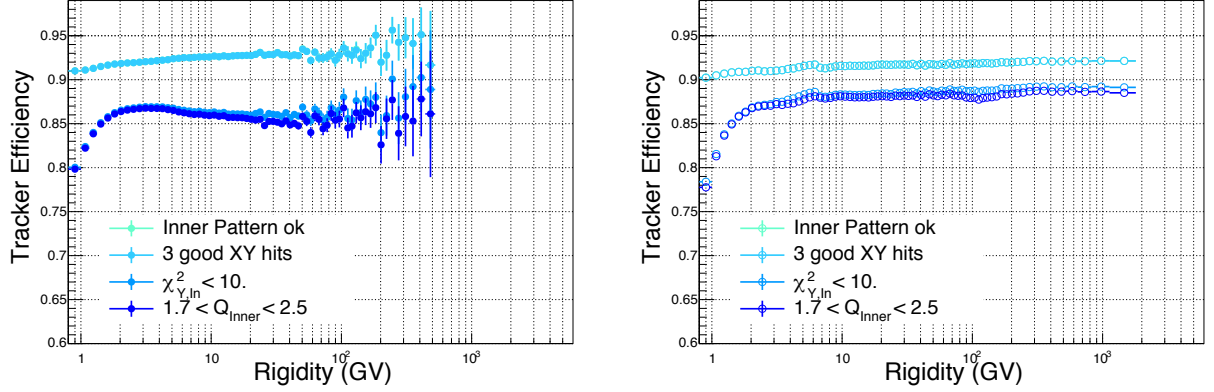


Figure 3.17 – *Efficiencies of the inner tracker successive cumulative cuts for both data (left) and MC (right) samples.*

can be seen in Figure 3.18 for the data sample and the MC sample. First of all, we cannot see any demarcation between the three different rigidity estimators. In the range where the ECAL rigidity is used the efficiency extends well the results from the other ranges. Once again we have a very good agreement between the data and MC within a few %.

### 3.3.4 External Layers Efficiencies

Since we choose to study the full span pattern for the flux, we need to produce the external layers efficiencies that we will go through separately for L1 and for L9. For the two of them, the sample will be selected with all the selection cuts from the pre-selection, the ToF selection and the tracker selection but for the last one, the cuts concerning the external layers are removed. To this selection, we add the condition that the extrapolated inner tracker track must be contained in the geometry of the L1 for the calculation of the L1 efficiency, or in the geometry of the L9 for the calculation of the L9 efficiency.

For the L1, the efficiency of the four selection cuts is computed namely the presence of a  $X$  and  $Y$  sided hit on the L1, if this selected hit has a good reconstructed charge, if the  $\chi^2_Y$  of the full span pattern reconstructed track is  $\leq 10$  and if the charge of L1 is in the range defined previously in the charge selection section. It is important to notice that the rigidity used for this efficiency is the one reconstructed from an inner+L9 pattern, thus we have an unbiased measurement. Figure 3.19 shows the cumulative successive cuts efficiencies. From this figure, we can observe that the  $XY$  hit requirement in the L1 is the most inefficient cut which is perfectly normal when considering Figure 3.5. The two other cuts that show a drop in the efficiency are the requirement of a good status of the charge of the hit and the charge selection. The final efficiency is presented in the Figure 3.20 for the data and the MC samples. Even if the efficiencies are quite low, both data and MC results are compatible within 4%.

An almost identical selection is applied for the L9 efficiency sample : we require the presence of a  $X$  and  $Y$  sided hit on the L9 as well as its location in a good reconstructed charge region, a  $\chi^2_Y \leq 10$  for the full span pattern reconstructed track and a L9 charge inside the charge selection range. In a same

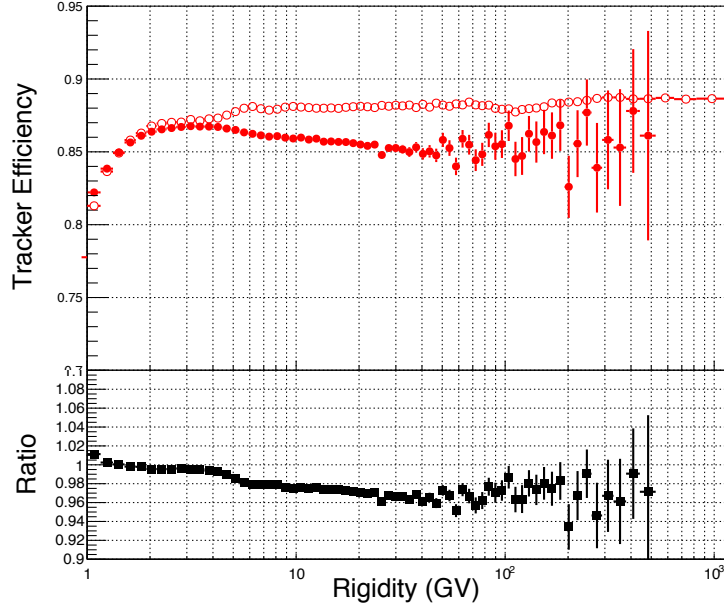


Figure 3.18 – Inner tracker efficiencies for data (full circle) and MC (open circle) samples plus the ratio of the two.

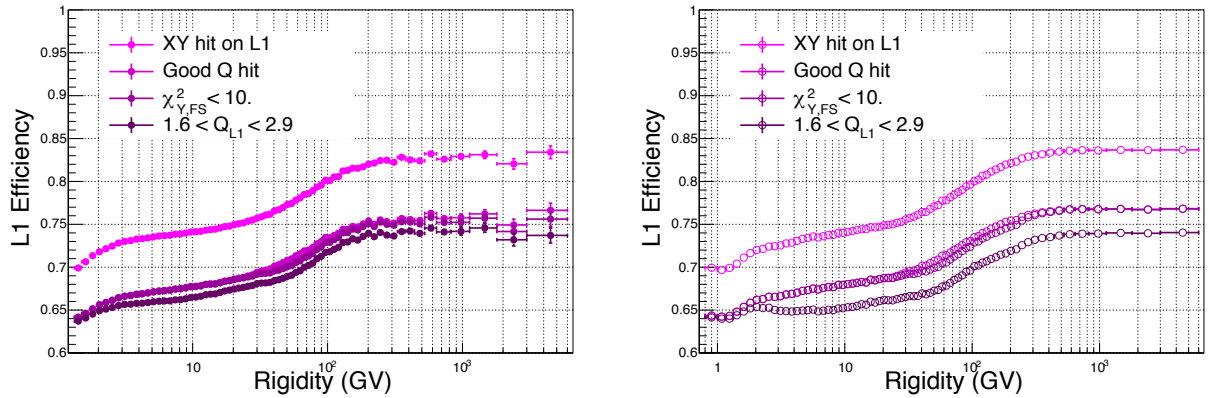


Figure 3.19 – Efficiencies of the L1 successive cumulative cuts for both data (left) and MC (right) samples.

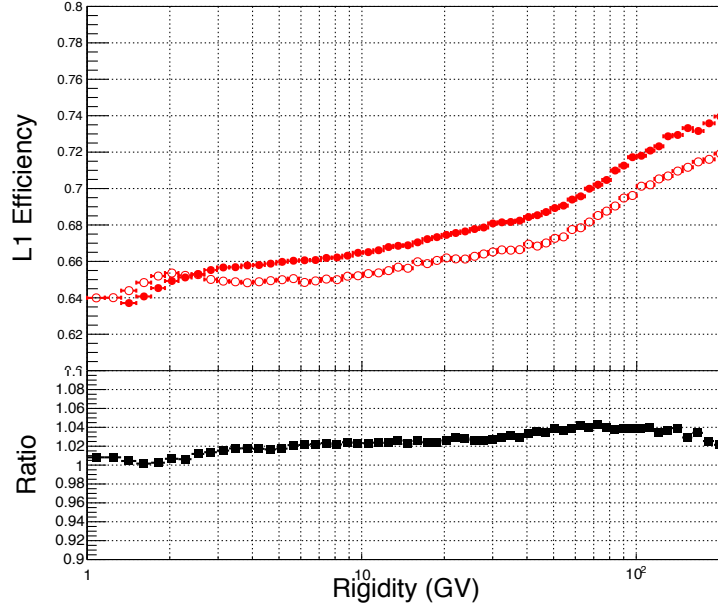


Figure 3.20 –  $L1$  efficiencies for data (full circle) and MC (open circle) samples plus the ratio of the two.

way than for the L1, the rigidity must be unbiased from the L9 which means that the rigidity used is the one from the inner+L1 pattern. The different cumulative successive selection efficiencies can be seen in Figure 3.21 and the final L9 efficiency is presented in Figure 3.22 for the both data and MC samples. We can observe the same behavior than for the L1 efficiencies. However, the compatibility between data and MC is slightly better: within approximately 2%.

All the different efficiencies for the different steps of the selection are now computed but as said previously, we will not use them directly as an efficiency factor to correct the flux but rather use the comparison between the results for the data and for the MC to correct the acceptance as calculated by the later. This method will be seen in details in the further sections.

### 3.4 Survival Probability

One thing to consider when talking about the external layers is the probability of an helium nucleus to survive through the substantial amount of material contained between the L1 and the L2, and between the L8 and the L9. The way we compute the efficiencies of the two external layers, this is already taken into account. However, the way the MC deals with the amount of material and the interactions that can happen in it needs to be checked for this selection. In that way, we produce what we call the survival probability for both the L1 and the L9 which is the probability that a helium particle will survive between L1 and L2 or between L8 and L9. This check will be describe in the

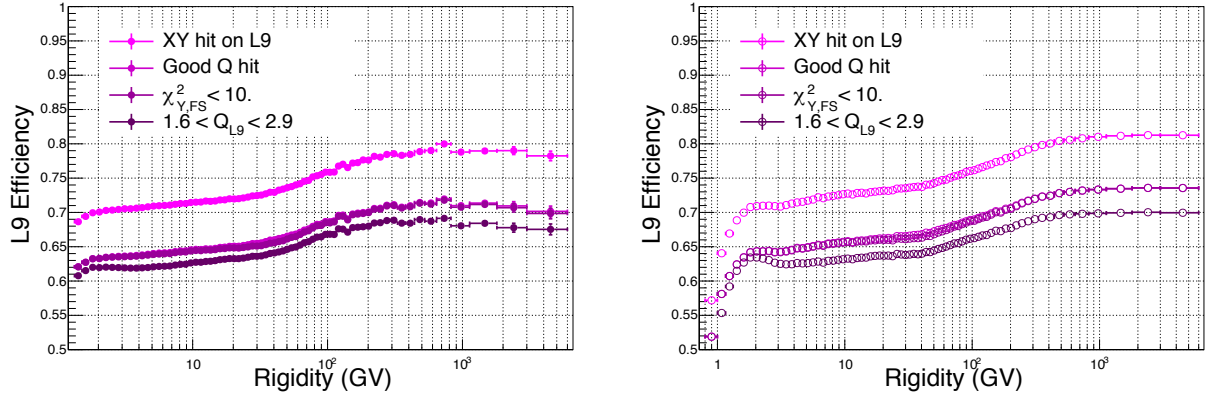


Figure 3.21 – Efficiencies of the  $L9$  successive cumulative cuts for both data (left) and MC (right) samples.

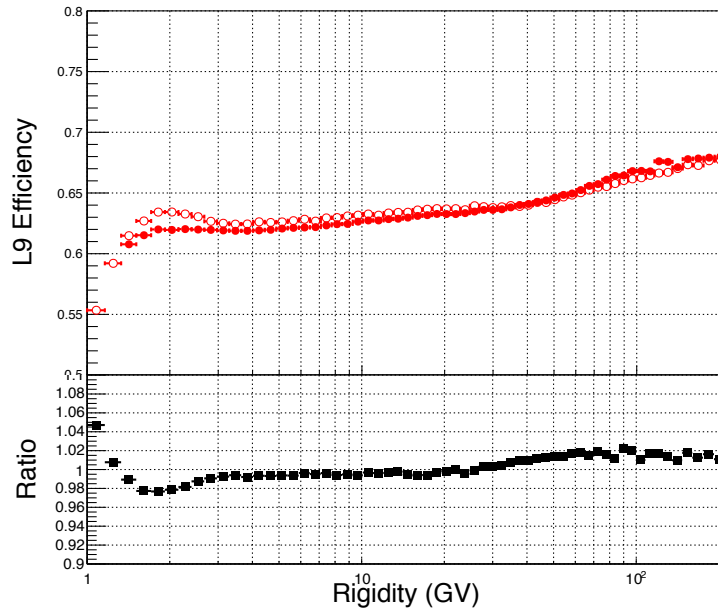


Figure 3.22 –  $L9$  efficiencies for data (full circle) and MC (open circle) samples plus the ratio of the two.

following lines and will be use as a systematic errors, computed in the last Section.

### L9 Survival Probability

The first survival probability we are going to compute is the one for the L9 because it is the easiest to get. The idea here is to check how many selected helium nuclei will still be helium nuclei after passing through the amount of material located between the L8 and the L9. The selected sample contains events with a inner+L1 pattern with extrapolation from inner tracker track inside the L9, which complete the pre-selection as well as the ToF and tracker selection but without any cut that includes the L9. The rigidity used is the one for the inner+L1 pattern. In order to have the cleanest sample possible we add the condition that the track goes through the ECAL geometry and that  $1.5 < Q_{ECAL} < 2.5$  if  $R \leq 4\text{GV}$  or  $1.5 < Q_{ECAL} < 3.2$  if  $R \geq 4\text{GV}$ . This selection on the ECAL charge ensures to have a helium event before and after the L9. The interval of charge selection depends on the rigidity because if we take a look at the distribution of the ECAL charge with respect to the rigidity on Figure 3.23 we can clearly see a strong dependence at low rigidity. Now that our

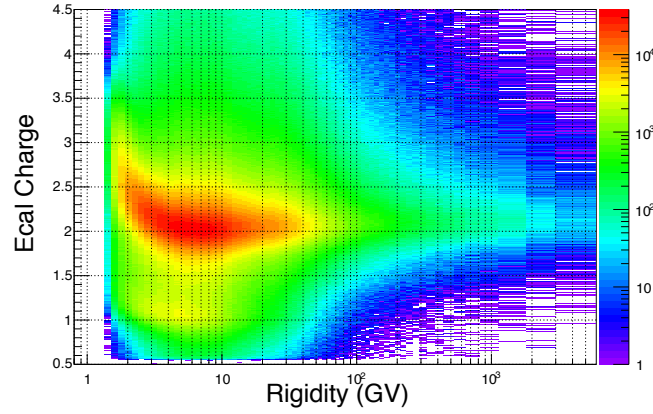


Figure 3.23 – *Charge distribution of ECAL with respect to the rigidity.*

sample is made we can compute the survival probability for the L9. For this, we use the Equation (3.1) where the number of selected events are those that have a charge  $Z = 2$  for the hit in the L9. Figure 3.24 shows the calculated survival probability for the L9 for both data and MC samples. The data and the MC results are compatible within 1% below 200GV.

### L1 Survival Probability

For the L1 survival probability, things are completely different. In principle one could do the same thing as for L9. But the charge resolution of L1 alone (Figure 3.8) is not sufficient to define a pure sample of the events. Indeed, we want to see how many helium nuclei remain after passing through the amount of material in between the L1 and the L2. To do so the selected sample needs to be only up-going particles that come from the bottom of the detector. To get such particles and to be sure we have enough statistic we must select a period of time when the detector was in a special



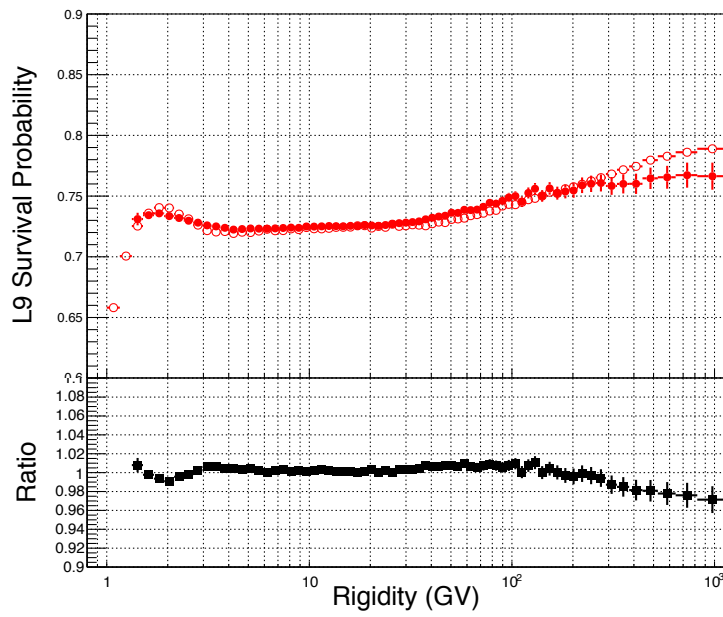


Figure 3.24 – *L9* survival probability for data (full circle) and MC (open circle) samples plus the ratio of the two.

orientation. For that we change the condition on the zenith angle  $\theta$  and require  $80^\circ < \theta < 100^\circ$ . Except for this, all the pre-selection is the same. For the ToF and Tracker selection only two things change : since we have up-going particles we require  $\beta < 0$  and there is no need for a geomagnetic cutoff restriction anymore. Once again, to avoid any bias all the cuts concerning the L1 are suppressed and the rigidity used is the one for the inner+L9 pattern. At the end, we use the Equation 3.1 to compute the L1 survival probability where the selected events are the ones that have a charge  $Z = 2$  for the L1 hit. Given the configuration of the detector, for the data the statistic is very low. For MC, a special production has been done to model up-going particle. Figure 3.25 presents the survival probability

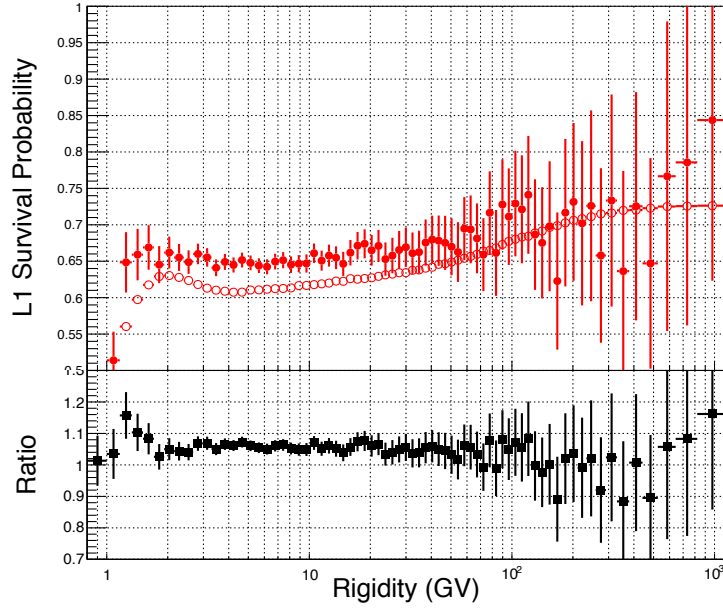


Figure 3.25 – *L1 survival probability for data (full circle) and MC (open circle) samples plus the ratio of the two.*

for L1 for both data and MC samples.

These survival probabilities will not be used directly like the efficiencies to correct the acceptance because these effects are already taken into account by the external layers efficiencies. The main goal of this study is to check the results from data and MC and to see if there is any difference between the ratio of the two for the L1 and for the L9. From this difference, we derive a systematic error. This will be performed in more details in the last section.

### 3.5 Acceptance

The acceptance of an experiment is the total efficiency including the geometry of the detector, it is calculated in  $m^2.sr$ . It can be purely geometric, in that case we refer to it as geometrical accep-

tance, or it can include all the efficiencies of the detector and in that case we refer to it as effective acceptance. The geometrical acceptance can only be computed from the MC. As mentioned previously, the acceptance that we use for the computation of the flux is the one including the efficiencies of all the selection cuts. Since the MC results are not strictly identical to the data results we need to correct this acceptance by the ratios between data and MC efficiencies determined above.

In this section we introduce the geometrical acceptance before talking about the effective acceptance that is used in the flux calculation. We will see that since we use the MC to compute the acceptance, we can express it with respect to the generated rigidity or the reconstructed rigidity. We also define the correction factors to apply to this acceptance in order to take into account the differences between the data and the MC efficiencies.

### 3.5.1 Geometrical Acceptance

The geometrical acceptance is a purely geometrical calculation that is why it is supposed to be completely rigidity independent. The following Equation is used to compute it :

$$a_{\text{geometrical}} = 3.9^2 \pi \frac{N_{\text{selected}}}{N_{\text{generated}}} \quad (3.5)$$

with  $N_{\text{selected}}$  the number of events that pass through the fiducial volume of the detector used for this analysis and  $N_{\text{generated}}$  the number of events generated by the MC. The  $3.9^2 \pi$  factor stands for the geometrical term that comes from the generated MC. The events are all generated in a square of 3.9m side length above the detector, as seen in the previous chapter.

To be sure that the events selected pass through the whole fiducial volume used for this analysis and since the only detectors that we include are the ToF and the tracker, and the pattern is the full span including the two external layers, we request the tracks to be inside every layers of the tracker. The ToF layers being located between L1 and L2 and between L8 and L9, the previous requirement is sufficient. The track used to fulfill the conditions is the one generated by the MC.

Figure 3.26 shows the geometrical acceptance obtained for the full span pattern as a function of the generated rigidity. As expected, it is independent with the rigidity and stays around  $0.045\text{m}^2\cdot\text{sr}$ .

### 3.5.2 Folded and Unfolded Acceptances

The second way of computing the acceptance is to correct the geometrical acceptance by adding the efficiency of the selection. This acceptance can be expressed either as a function of the generated rigidity, which we refer to as *unfolded acceptance*, or as a function of the reconstructed rigidity, which we refer to as *folded acceptance*. The folded acceptance integrates a problem well known when dealing with power law flux types : the bin-to-bin migration of the events that occurs especially at low and high rigidities. We will see in more details how to correct it in the next Section.

First of all, to compute these acceptances we are using Equation 3.4. Here the number of selected events go through all the steps of the selection that we described in the first section, the same way we selected the number of helium nuclei to compute the flux.

The next step is to correct for the slight differences we have observed between the data and the MC. For that, we use the ratios  $\frac{\epsilon_{\text{data}}}{\epsilon_{\text{MC}}}$  for the efficiencies of the ToF, the inner tracker, the L1 and the L9. The idea here is to parametrize such ratios and to use them to compute a correction factor which will be used to correct the acceptances. Figures 3.27, 3.28, 3.29 and 3.30 show these four ratios with their

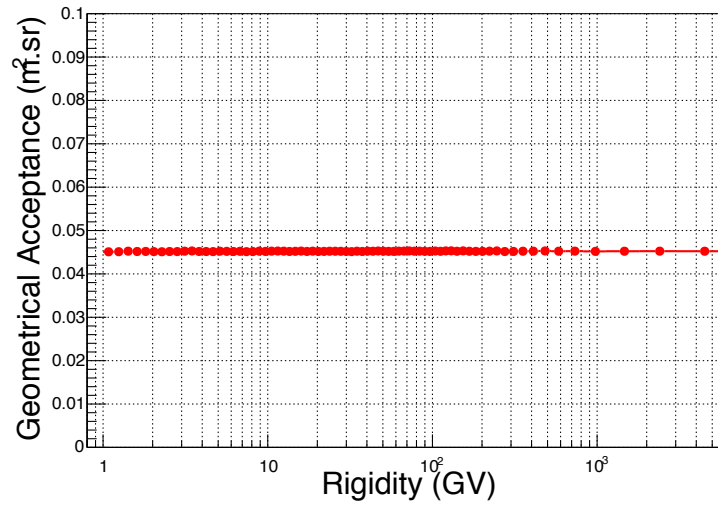


Figure 3.26 – *Geometrical acceptance for the full span pattern in generated rigidity.*

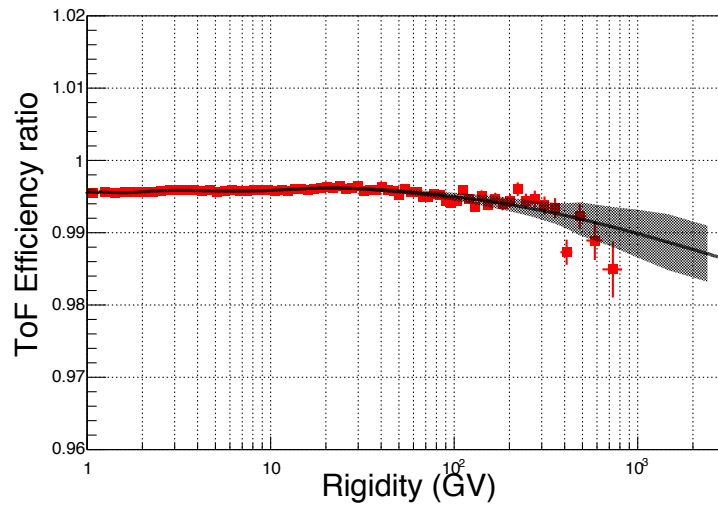
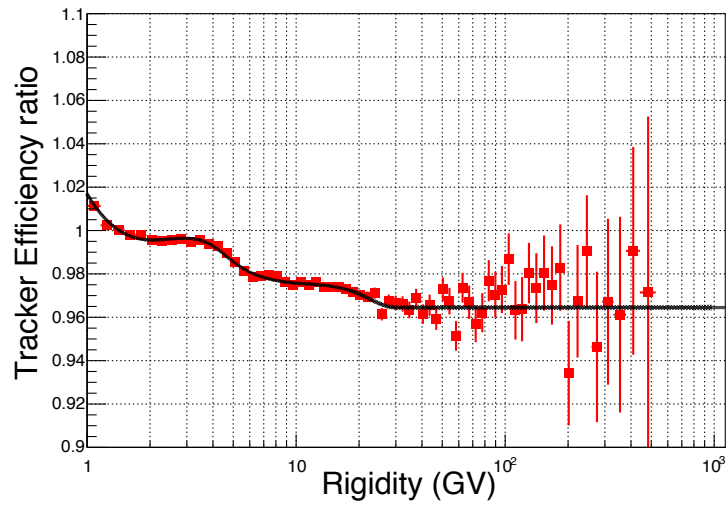
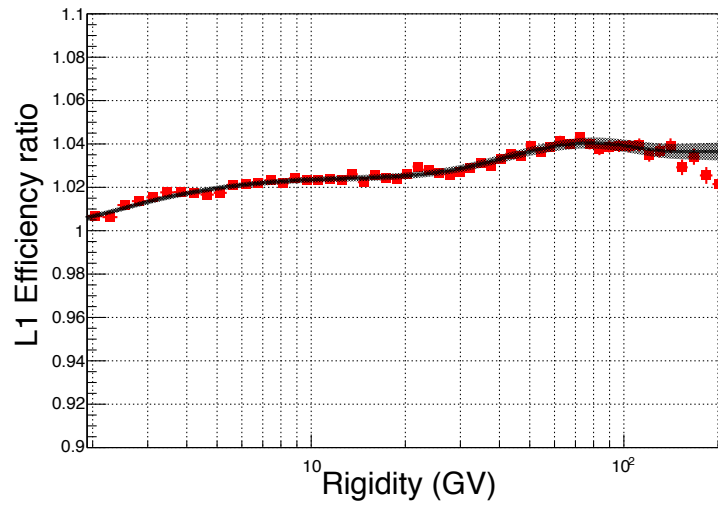


Figure 3.27 – *Parametrized ToF efficiency ratio.*

Figure 3.28 – *Parametrized inner tracker efficiency ratio.*Figure 3.29 – *Parametrized L1 efficiency ratio.*

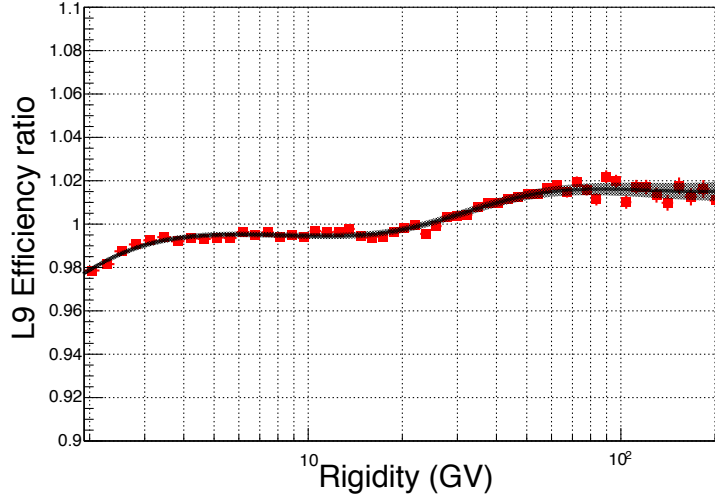


Figure 3.30 – *Parametrized L9 efficiency ratio.*

parametrization. Once we multiply them we end up with the correction factor presented in Figure 3.31. Now, we just have to apply this factor to the acceptances.

The final folded acceptance is shown in Figure 3.32 and the final unfolded acceptance is shown in figure 3.33. We clearly see the difference between the folded and the unfolded acceptances. This difference occurs especially at high rigidity, the number of events in the last bins being higher for the folded acceptance than for the unfolded one. This effect needs to be carefully taken into account to correct the true final flux and correct for this bin-to-bin migration. Several options are available to correct this folding effect, we choose one of them for this analysis and we are going to describe this unfolding procedure in the next section.

### 3.6 Unfolding Procedure

The purpose of this unfolding procedure is to correct the flux that we have obtained for the migration effects that appear at low and high rigidity. Indeed, this effect can be described by the following Equation:

$$N_{obs}(R_{obs}) = \int_{-\infty}^{\infty} N(R)S(R_{obs} - R)dR \quad (3.6)$$

with  $N_{obs}(R_{obs})$  the number of observed events as a function of the observed rigidity,  $N(R)$  the true number of event as a function of the true rigidity,  $S(R_{obs} - R)$  the resolution function. Among the different methods that can be used we chose the method that unfolds the acceptance iteratively. This method, called the *folded acceptance method* is using a reweighting of the shape of the generated MC spectrum for several iterations in order to reproduce the observed rigidity distribution.

The procedure is made of five steps that we will repeat as often as we need it in order to converge. The first step consists in computing the weights we need to apply to the generated MC production

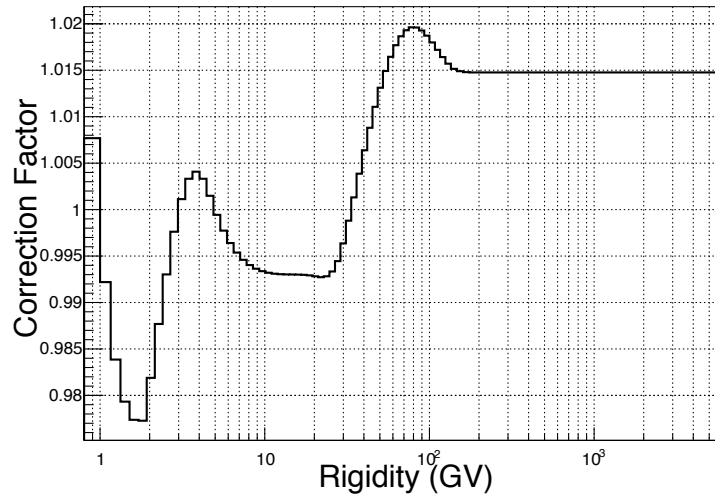


Figure 3.31 – *Correction factor from the efficiency ratios.*

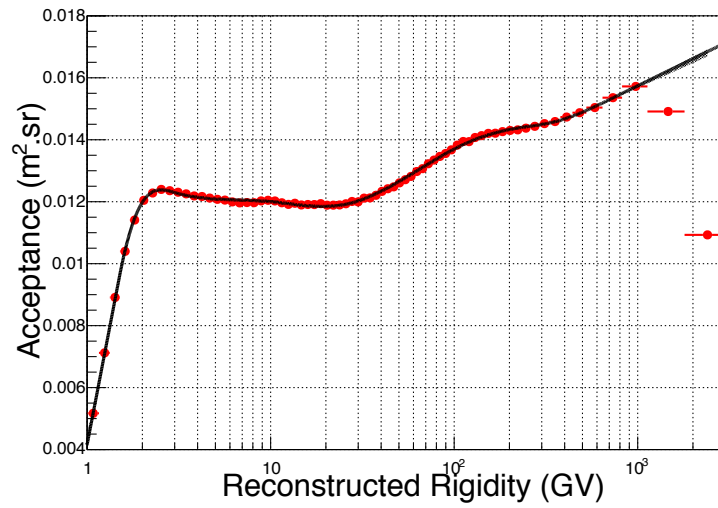


Figure 3.32 – *Folded acceptance with respect to the reconstructed rigidity.*

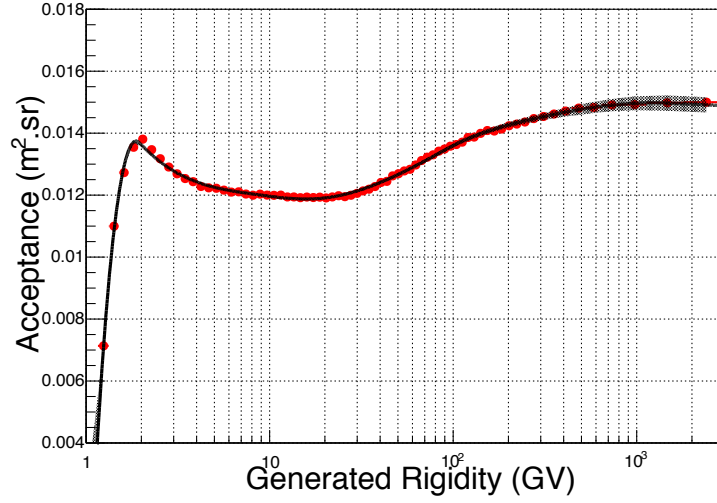


Figure 3.33 – *Unfolded acceptance with respect to the generated rigidity.*

to make it correspond to the folded flux. For the second step, we reprocess the MC analysis applying this weight to each event. Once the MC is reprocessed, the third step is to reparametrize the efficiency ratios between data and new MC. The forth step consists in computing the new folded acceptance and to correct it with the new correction factor found at the previous step. The last step is the calculation of the new unfolded flux.

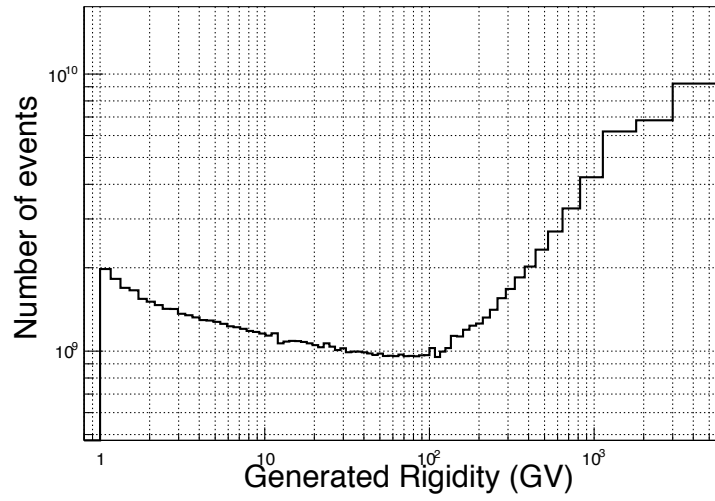
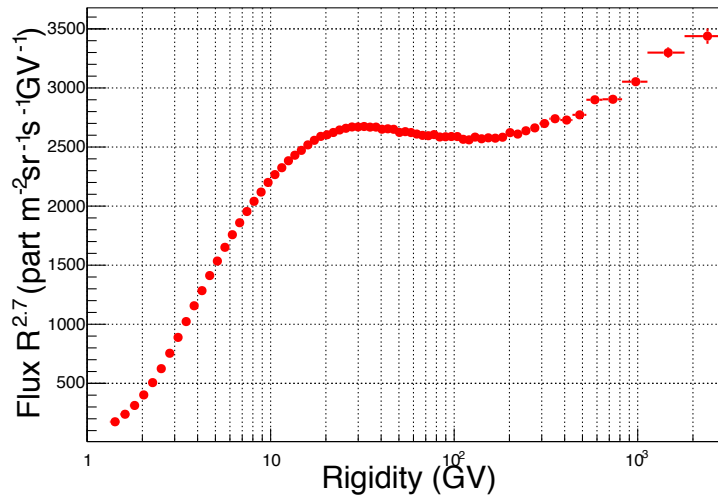
### Iteration Zero

The iteration zero is a preliminary calculation of the flux because we need an input flux to start the procedure and to give the correct shape to our MC spectrum. Indeed, if we take a look at the MC spectrum, Figure 3.34, we can see that this production is not following a power law spectrum but rather a flat distribution in momentum, which gives this shape for the rigidity distribution using a changing binning. The purpose here is to have a distribution that will give the best approximation of the true flux that should be used as the input MC production, that is why we are going to use the flux computed from this analysis using the Equation 3.1. Since we used the folded acceptance which is parametrized the flux is folded as well. Figure 3.35 shows the first folded flux. A factor  $R^{2.7}$  is applied to the flux in order to see its shape above few hundred of GV. Indeed, we can see the rise at high rigidity which corresponds to the bin-to-bin migration we want to correct. We can now start the unfolding procedure.

### First Iteration

Now, we are going to follow all the five steps of the procedure to unfold the acceptance a first time. First of all, we need to calculate the weights that will be applied to the MC spectrum. To do so, we first normalize the folded flux and the MC production. Then we compute the weights for each



Figure 3.34 – *Distribution of the generated rigidity.*Figure 3.35 – *First computation of the folded flux.*

rigidity bin  $i$  with the Equation :

$$w_i = \frac{\phi_{i,norm}}{MC_{i,norm}} \quad (3.7)$$

with  $\phi_{i,norm}$  the normalized flux for the bin  $i$  and  $MC_{i,norm}$  the normalized generated MC events for the bin  $i$ . Next, we parametrize this weight distribution and finally we normalize this parametrized weight distribution to obtain the final weight to apply to the MC generated distribution. Figure 3.36

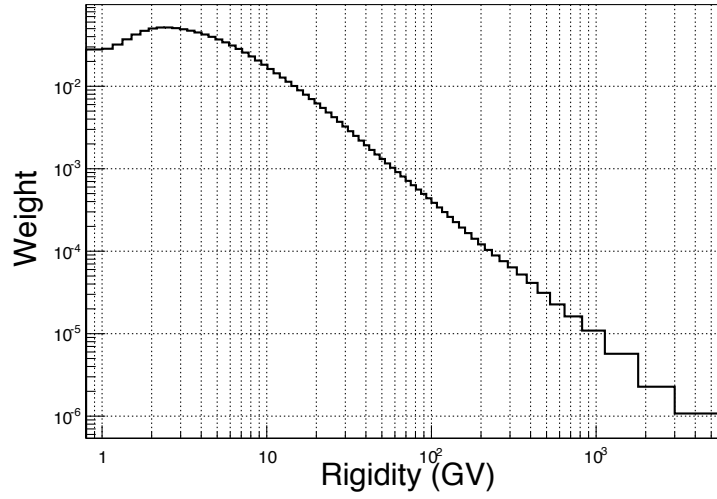


Figure 3.36 – *Distribution of the calculated weights.*

gives the distribution of the weights in rigidity bins.

The second step consists in reprocessing the MC production with the obtained weights to reproduce all the results but with an updated estimate of the generated rigidity distribution. Once we have done that, we get new results for the efficiencies and the acceptances. In step three, we parametrize the four ratios between data and MC efficiencies to get a new correction factor for the acceptance as seen in the previous section. At this stage of the procedure, we can already compare the previous folded acceptance with the new one, see Figure 3.37, and we can notice that the new acceptance is already higher in the last bins than previously which will tend to correct the folded flux when we will compute it at the next step.

Finally, now that we have all the ingredients we can compute the new flux. From the comparison of the new and the previous flux, see Figure 3.38, we can see the effects of this unfolding procedure at high energy. Indeed, the flux is depleted from one iteration to another which means that the bin-to-bin migration has been corrected.

We are going to carry on with this procedure by making several more iterations until we are satisfied of the results.

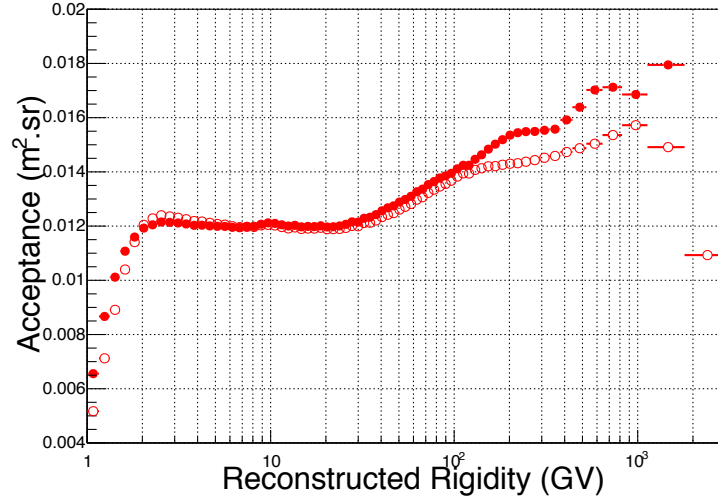


Figure 3.37 – Acceptance for iteration 1 (full circle) compared to the previous folded acceptance (open circle).

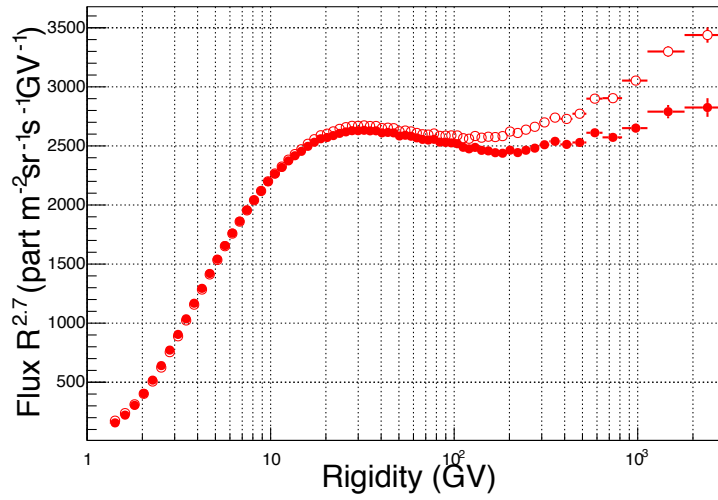


Figure 3.38 – Flux for iteration 1 (full circle) compared to the previous folded flux (open circle).

### Last Iteration

To be sure that we stop the procedure at the right moment, we are going to define a criteria that will ensure us that we reach the best correction that we could get for the unfolding. We define:

$$\epsilon_{n_{iter}} = \sum \frac{(A_{n_{iter},i} - A_{n_{iter}-1,i})^2}{A_{n_{iter}-1,i}} \quad (3.8)$$

which means that we compare the last iteration to the previous one by summing the bin-per-bin difference. To stop the iteration loop we require  $\epsilon_{n_{iter}} < 10^{-4}$ . As we can see in the figure 3.39, this

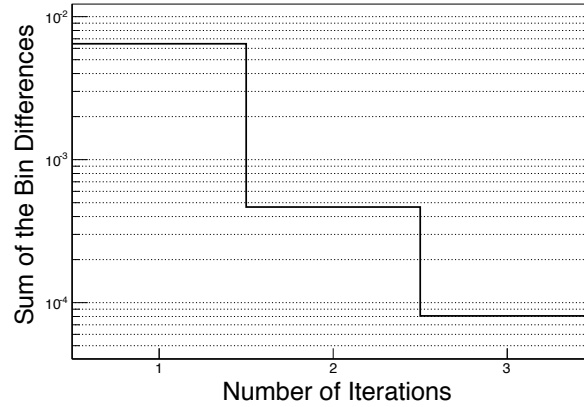


Figure 3.39 – Comparison criteria with respect to the number of iterations.

condition is already reached for the third iteration.

Figure 3.40 show the folded acceptances for all the iterations, that becomes less and less folded with the number of iteration. However, at high rigidities we have fluctuations that tend to amplify with the unfolding procedure. The unfolding procedure is now over and we have the final result for the acceptance that we can use in the Equation 3.1 to compute the final flux.

## 3.7 Systematic Errors

This last section concerns the errors that we are going to associate to the flux, more precisely the systematic errors. These systematic errors are the errors on all the corrections which we apply, reflecting uncertainties in the MC parameters and other input to the flux calculation. For what concerns the statistical errors, they are really easy to compute by summing quadratically the statistical errors of all the ingredients needed to compute the flux, we will not talk any longer about them, especially because they tend to be small compared to the systematic errors because the statistic is high for the number of detected helium nuclei. However, the systematic errors need more attention.

We identified five sources of systematic error: the trigger efficiency, the acceptance, the unfolding procedure, the rigidity scale and the survival probability. We are going to comment on these errors

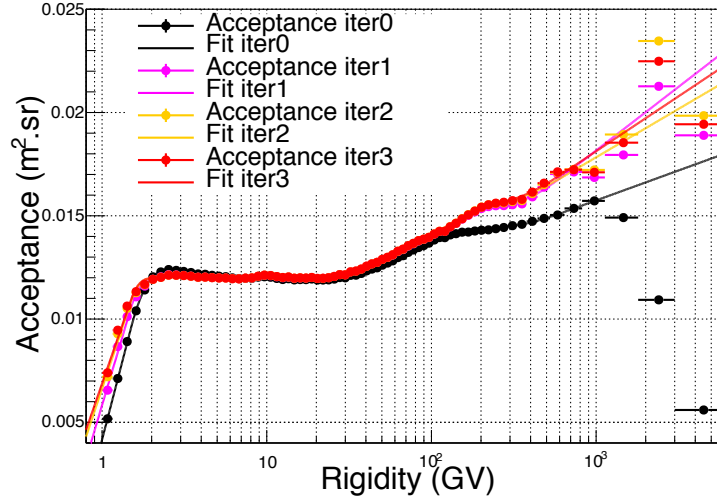


Figure 3.40 – Comparison of acceptances from all the iterations.

one by one and give the details of their computation.

### 3.7.1 Trigger Efficiency Errors

The trigger efficiency systematic errors come from the fact that when comparing the efficiencies of data and MC we observe a small difference between them. To compute the error associated we use the ratio  $\frac{\epsilon_{data}}{\epsilon_{MC}}$  for the trigger efficiencies that we parametrize and find the associated errors. These associated errors are computed bin by bin by taking the average error over five bins around the studied bin (including this bin), for example for the  $i^{th}$  bin the error on the ratio  $\Delta r_i$  is calculated with the following Equation:

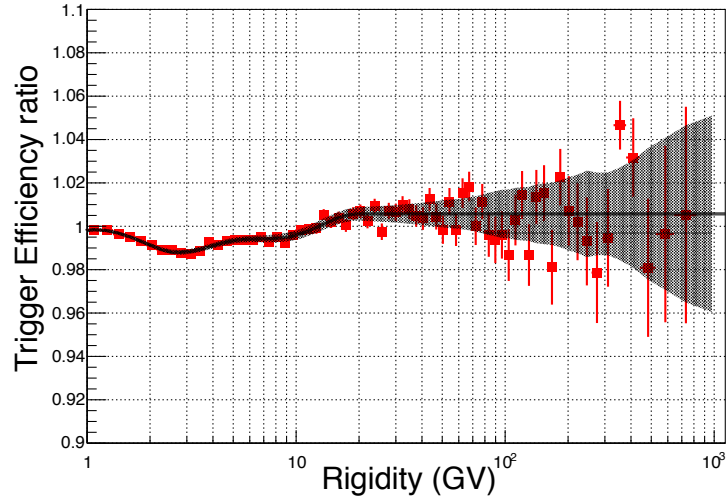
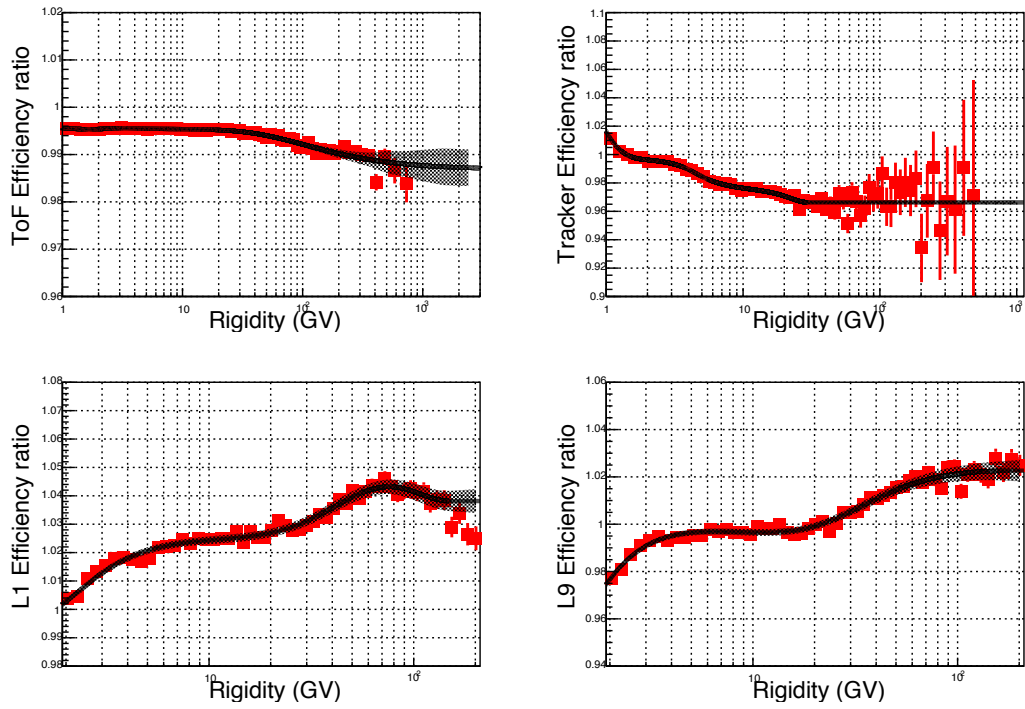
$$\Delta r_i = \frac{\sum_{j=i-2}^{i+2} \Delta r_j}{5} \quad (3.9)$$

Figure 3.41 shows the parametrized ratio with the errors associated. The percentage of errors for this ratio represent the percentage of errors we are going to use for the trigger efficiency systematic error.

### 3.7.2 Acceptance Errors

For the acceptance, we can distinguish two sources of errors: the error that comes from the parametrization of the acceptance itself and the error associated to the correction factor. As seen in a previous section, the acceptance has been corrected by the differences that occur between the efficiencies for data and MC using the ratio of the two efficiencies for the ToF, the inner tracker and the two external layers. These ratios have been parametrized, thus the resulting errors will be the quadratic sum of the four errors that come from these parametrizations, calculated with the Equation 3.9.

We can see the parametrization of the four efficiency ratios with the associated errors in Figure 3.42.

Figure 3.41 – *Parametrized trigger efficiency ratio.*Figure 3.42 – *Parametrized efficiency ratios for the ToF, the inner tracker, the L1 and the L9.*

A quadratic sum of the two error sources is used to compute the acceptance error. Figure 3.43 shows

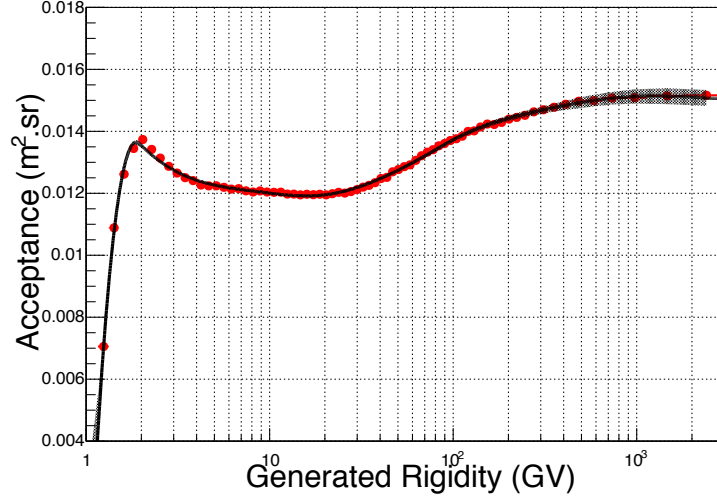


Figure 3.43 – *Parametrized acceptance with final errors associated.*

the final parametrized acceptance with its errors.

### 3.7.3 Unfolding Errors

For the error that comes from the unfolding procedure, we need determine what kind of errors we are going to consider. It seems clear that the errors can only come from the iterative procedure. A good measure of the error is the difference between the last iteration result and the previous iteration result. More simply the following Equation is used to compute the error per rigidity bin  $i$  :

$$\Delta_{unfolding,i} = \frac{A_{n_{iter},i} - A_{n_{iter-1},i}}{A_{n_{iter},i}} \quad (3.10)$$

with  $A_{n_{iter},i}$  the acceptance of the last iteration and  $A_{n_{iter-1},i}$  the acceptance for the previous iteration.

### 3.7.4 Rigidity Scale Errors

The rigidity scale errors have been previously calculated by the collaboration for the published helium flux. Two sources of errors contribute to it the residual tracker misalignment and the magnetic field map measurement and its temperature [34]. We will use the same calculated error by the collaboration. This error due to the rigidity scale is below 0.6% until 100GV and reaches 6% for the last rigidity bin.

### 3.7.5 Survival Probability Errors

The survival probability error, as explained previously, comes from the fact that for the two external layers the ratios between data and MC efficiencies do not agree as they should do if their discrepancy comes from the amount of material and the interaction cross-sections in the MC. This disagreement needs to be taken into account. The systematic errors is the difference between the two ratios. To compute the errors we will use the Equation per rigidity bin  $i$  :

$$\Delta_{survivalprob,i} = \frac{r_{L1,i} - r_{L9,i}}{2 \cdot r_{L1,i}} \quad (3.11)$$

with  $r_{L1,i}$  the efficiency ratio of L1 for bin  $i$  and  $r_{L9,i}$  the efficiency ratio of L9 for bin  $i$ . Obviously, these efficiency ratios are parametrized before being used in the previous equation, Figure 3.44 shows

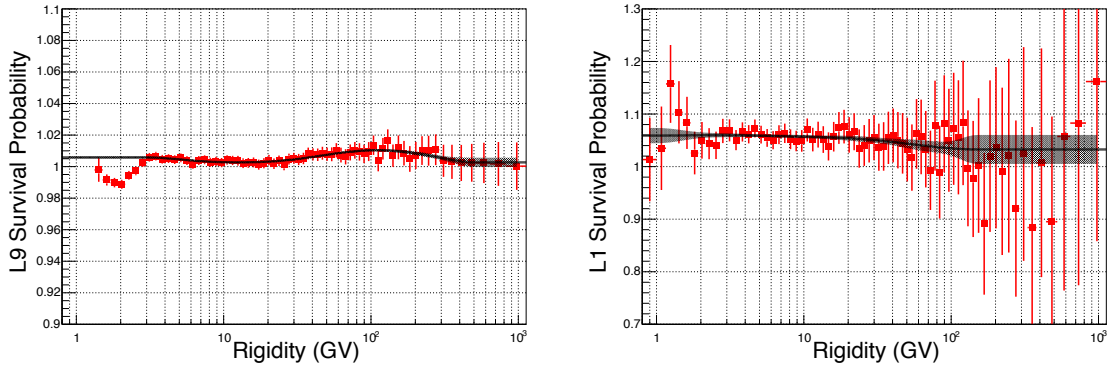


Figure 3.44 – *Parametrized survival probability ratios for L1 and L9.*

these parametrization.

Figure 3.45 resumes all errors in percentage. We can see that at low rigidity the survival probability errors dominates but tends to decrease above 30GV. The rigidity scale errors dominate at very high rigidity as expected. The acceptance errors are quite stable over the whole rigidity range. The trigger efficiency error and the unfolding error show a similar shape, low at the beginning but going up with the rigidity.

The final error is computed as the quadratic sum of all the six independent sources of errors. It is never higher than 3% at low rigidity, decreases slightly after 20GV, but goes up above 100GV until reaching approximately 9% for the last bin.

Through this chapter we have seen all the details of the helium analysis performed for this work starting from the selection that ensure us we correctly picked up the helium nuclei to the calculation of the systematic errors associated to the production of such a flux. We have introduced different problematics that arise for this kind of analysis such as the unfolding or the effect of the disagreement between the data and the MC efficiency results. Now that all the steps for the analysis have been done, we can move to the final calculation of the helium flux.



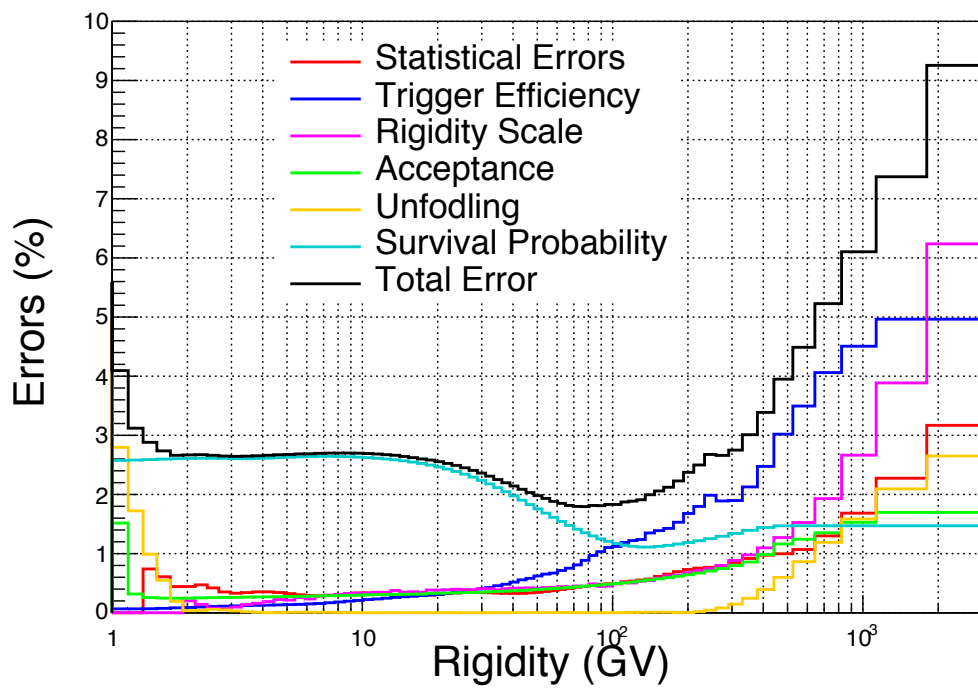


Figure 3.45 – *The statistic and systematic errors and the total errors.*



## Chapter 4

# RESULTS ON THE HELIUM FLUX

This chapter is dedicated to the results we obtained on the helium flux with this analysis. In the literature, the helium spectrum has been represented in energy, in rigidity, in energy per nucleon or in momentum. Even though these units are different they all stem from the same two characteristics: the kinetic energy from calorimeters and the magnetic rigidity from spectrometers. All the other quantities can be derived if the mass is known. We have decided to compute our fluxes in rigidity because we have this measurement directly from the tracker, but we can easily switch to the momentum using the charge.

Through this chapter, we will give a detailed computation of the fluxes and the first results we got for the restricted data set. Next, we will compare to the published results for the helium flux. Finally, we will present the results obtained for the extended range of data. Indeed, more data are available for the analysis than the restricted set that has been used for the publication, so that we can produce the helium flux with larger statistics. However, the analysis stays the same. We will compare the results obtained for this extended data set with the collaboration's published results. This way we can check the expectation that improved statistics only improves the result in a marginal way. The end of the last section will be dedicated to a few observations concerning the results.

### 4.1 First Results

The flux represents the number of particles detected per unit of surface per unit of time per unit of rigidity, it is given as the number of particles·m<sup>-2</sup>·sr<sup>-1</sup>·s<sup>-1</sup>·GV<sup>-1</sup>. It includes the ingredients we described in the previous chapter and will recall in this section. To end up with a coherent result, one needs to understand the efficiencies, the acceptance and the data-MC adjustment, as well as in the bin-to-bin migration due to the power law shape of the flux via the rigidity resolution.

#### 4.1.1 Flux Calculation

The flux calculation requires four important factors: the number of selected events, the time during which the detector collected the data, the geometrical acceptance and the efficiency of the detector. In this work we choose to combine the geometrical acceptance with the efficiencies, this is

made possible by the good quality of the MC. Only few corrections have to be applied to the results in order to take into account the small differences we see when comparing data and MC results. The equation we have used for our flux computation is the following :

$$\phi_{He} = \frac{N_{He}}{\Delta T \cdot A_{corrected} \cdot \epsilon_{Trigger} \cdot \Delta R} \quad (4.1)$$

$N_{He}$  represents the raw number of helium nuclei selected with the analysis process, it can be seen in figure 3.10.  $\Delta T$  is the exposure time calculated when the detector was collecting data, see figure 3.11.  $A_{corrected}$  is the corrected acceptance, including the data-MC efficiency ratio corrections from the ToF, the inner tracker, the L1 and the L9. This acceptance also includes the bin-to-bin migration correction, as we have seen in the previous chapter, so we are taking the last iteration acceptance here. Figure 4.1 show this final acceptance.  $\epsilon_{Trigger}$  is the trigger efficiency which we have parametrized as

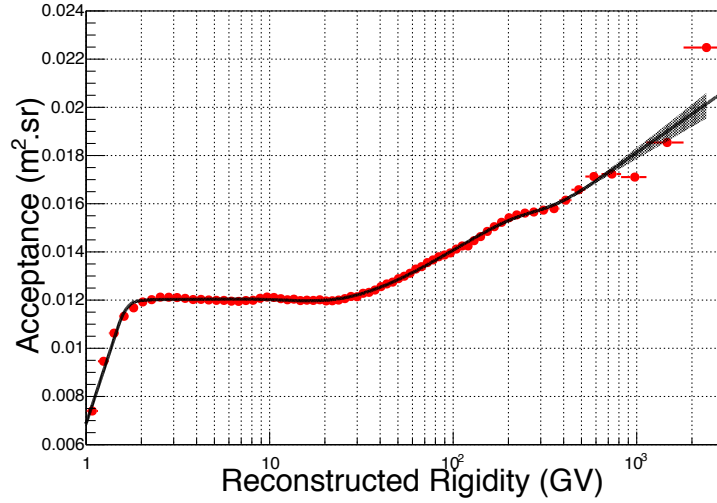
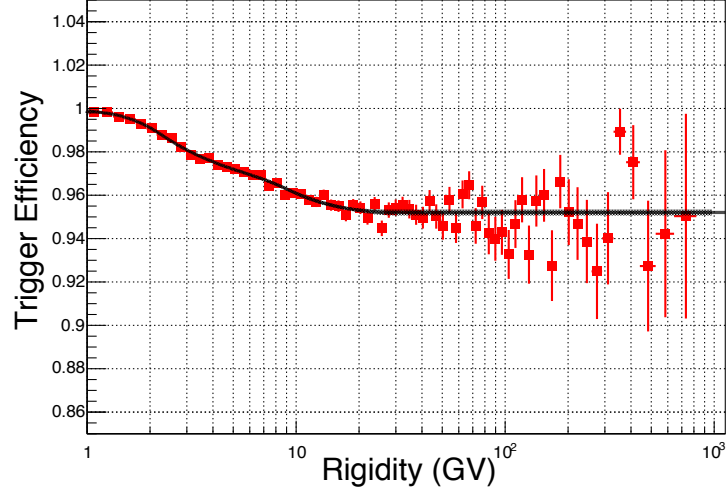
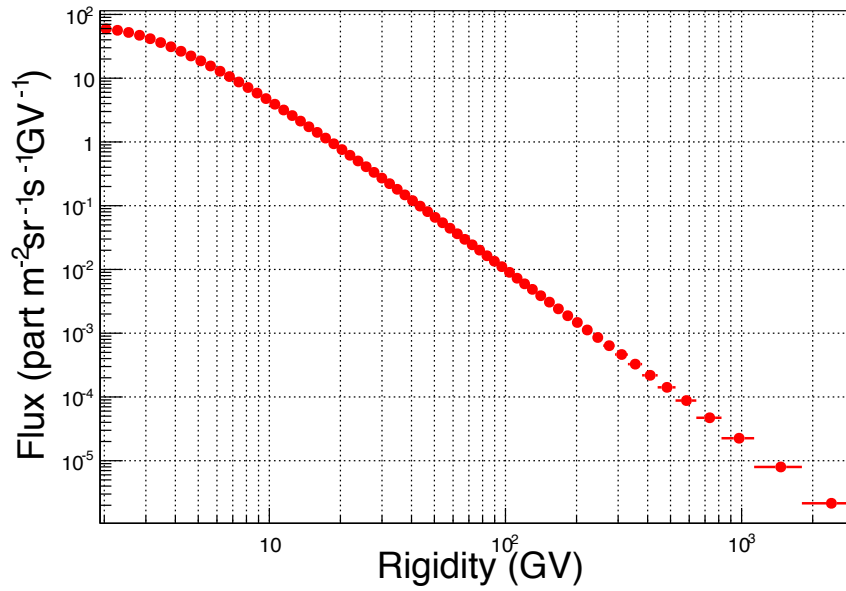


Figure 4.1 – Parametrized folded acceptance  $A_{corrected}$  from the last iteration of the unfolding procedure.

explained in section 3.3, Figure 4.2 show this efficiency with the applied parametrization.  $\Delta R$  is the width for each rigidity bin.

#### 4.1.2 Flux results

The helium spectrum for this analysis, in the publication time range, can be seen in Figure 4.3. As expected, above about 10GV this spectrum follows an approximate power law. At 2GV the flux is approximately of 60 particles·m<sup>-2</sup>·sr<sup>-1</sup>·s<sup>-1</sup>·GV<sup>-1</sup> and drops to 10<sup>-2</sup> particles·m<sup>-2</sup>·sr<sup>-1</sup>·s<sup>-1</sup>·GV<sup>-1</sup> when reaching 100GV. We have seen in the first chapter that, according to previous AMS-02 results on the proton flux, the spectral index was changing with rigidity. In this Figure we cannot really see how the spectral index behaves as a function of the rigidity. In order to detect such a change in the slope of the spectrum, we have multiplied the flux by a factor  $R^{2.7}$ . The result is shown in the Figure 4.4. Indeed, we can have a better look at what happens with the spectral index value over the rigidity

Figure 4.2 – *Parametrized trigger efficiency.*Figure 4.3 – *Helium flux for the restricted data set.*

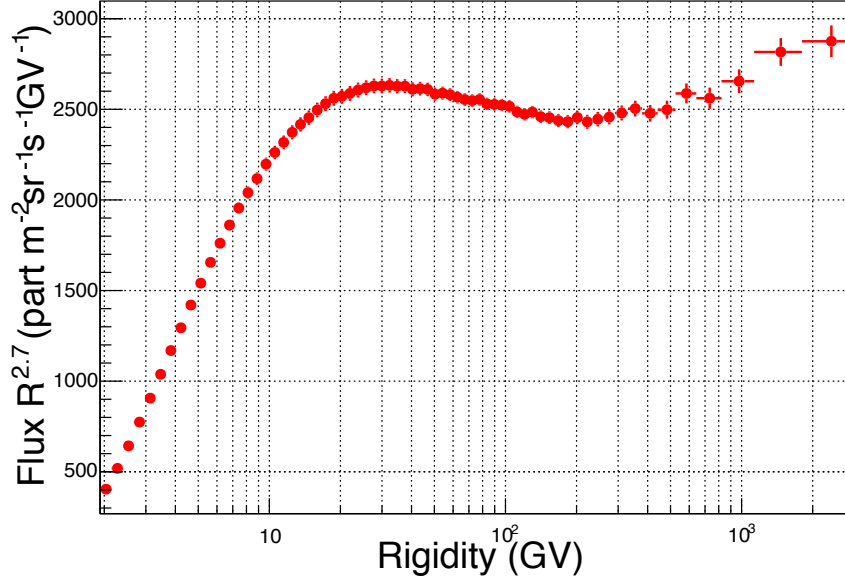


Figure 4.4 – *Helium flux for restricted data set multiplied by a factor  $R^{2.7}$ .*

range, and we can conclude that there is a significant change in the slope of the spectrum at about 200GV.

The next step now is to compare our result for the Helium spectrum with the one published at the end of 2015 by the AMS-02 collaboration in order to validate the methods used in this analysis.

## 4.2 Comparison with the Collaboration results

In 2015, the AMS-02 collaboration released a paper about the helium flux measurement with the AMS-02 detector [1]. All the details of this analysis can be found in the paper. The analysis performed for the work presented in this thesis is based on methods similar to the one performed by the collaboration. The quality cuts applied by the collaboration are slightly different, but the charge selection is the same. Consequently, the effective acceptances are different and we cannot compare them. The unfolding procedures are not similar, as we used an iterative procedure on the folded acceptance, the collaboration used two methods, a forward unfolding procedure as well as an iterative procedure that gave compatible results.

In order to get a fair comparison between the collaboration results and our results we can only compare the final helium flux measurement as well as the final total errors. Figure 4.5 represents the two helium spectra from the publication of the AMS-02 collaboration and from the work presented in this thesis, as well as the ratio between them. As we can see they are in good agreement. They do not differ by more than 2% all along the rigidity range. The ratio is quite stable over the whole rigidity range and the maximum discrepancy is at very low and high rigidity. The error comparison is presented in the Figure 4.6. As for the flux, the errors do not show big discrepancy. However, our total errors

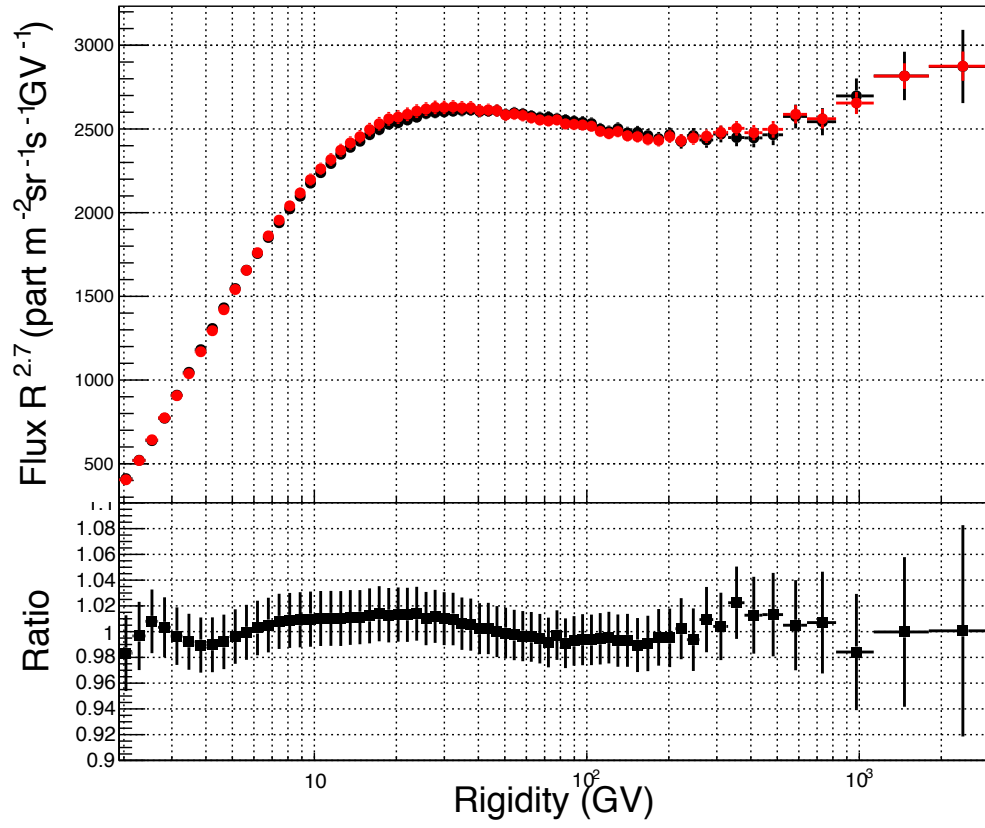


Figure 4.5 – Comparison of the helium spectra from this analysis (red) and from the published analysis (black) on the same data set and the ratio of the two.

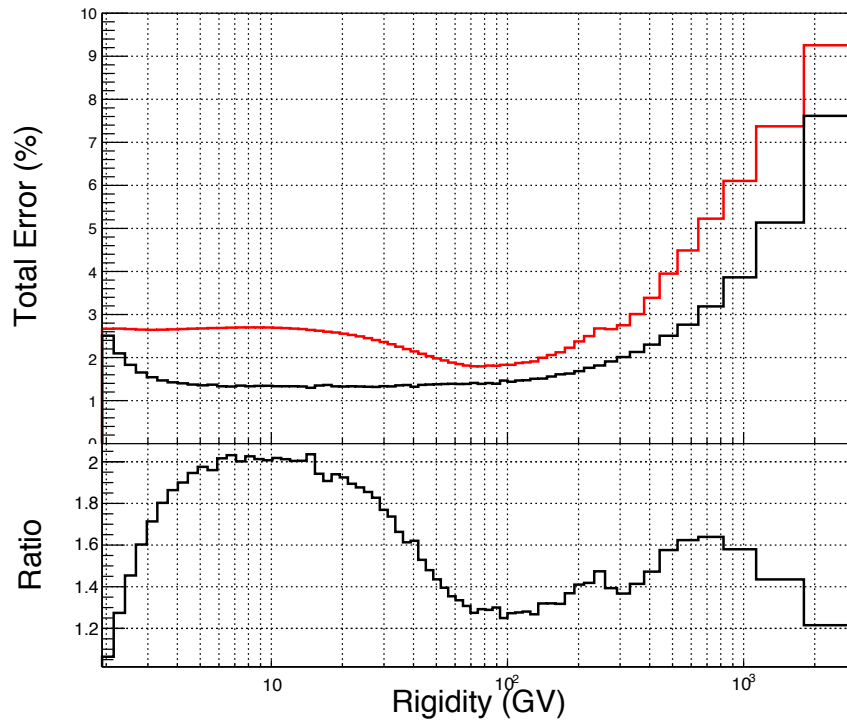


Figure 4.6 – Comparison of the total errors from this analysis (red) and from the published analysis (black) on the same data set (top) and the ratio of the two (bottom).



are always larger than the total errors from the published results. Nevertheless, this difference never exceeds 2.5%. The discrepancy around 10GV comes from the survival probability systematic error. At high rigidity, the trigger systematic error is the one that dominates right after the Rigidity scale systematic error explaining the discrepancy around 1TV.

From these results, we can conclude that the work presented in this thesis, for the restrained publication range of time, is fully compatible with the published AMS-02 results.

### 4.3 Extended Analysis and Final Results

As seen previously, the data set we have been using until now is a restricted one in order to analyze the same amount of data than for the published results. The data set can be increase to perform the analysis on all available reconstructed data. This data set extends the first data set until the run number 1432686053 which correspond to adding 19 months of data to the amount we already have.

All the analysis needs to be done again, but it is the exact same analysis we performed for the first data set. We will need to go through all the different steps we saw in the previous chapter in order to get all the factors presented in the equation 4.1 to compute the flux. Then we will compare the new computed flux to the published one to check if an improvement can be obtained by simply increasing statistics.

#### 4.3.1 Analysis

The analysis process is the same and all the cuts presented in the previous chapter are respected. This process leads us to a final number of selected helium of  $5.5 \cdot 10^7$ . This means an increase in the statistic by more than 50%. Figure 4.7 show the distribution of the number of selected helium nuclei as a function of the rigidity.

The exposure time shown in Figure 4.8, is about 50% higher than for the previous data set as expected. Going further with the analysis, we produce the efficiency and more importantly the efficiency ratios between data and MC for the ToF, the tracker, the L1 and the L9 in order to get the correction factor for the acceptance as explained in Chapter 3. The four parametrized ratios are presented in Figure 4.9. We also go through the unfolding iterative process to get the final acceptance which is used for the computation of the flux. The last iteration result for the acceptance with all the corrections applied is shown in Figure 4.10. Next, we compute the trigger efficiency and parametrize it as we can see in the Figure 4.11. The survival probability for L1 and L9 are measured in data as well as their data-MC ratios. Without any surprise there is still a discrepancy between the L1 and L9 ratio which means that we need to include this in the systematic errors.

Finally, all the systematic errors described in the previous chapter are computed again. We can see the individual errors as well as the total errors in the Figure 4.12. As expected, the statistical errors are slightly lower than for the reduced data set, which induces a reduction in the total error. This total errors have the same shape as previously but end up at approximately 8.4% for the last bin instead of 9%.

Now that we have completed the analysis we are going to use the already defined equation 4.1 to compute the helium flux. As for the previous results, we are multiplying the flux by a factor  $R^{2.7}$ . The final result is presented in the Figure 4.13. At first glance, the shape of the flux seems to be the

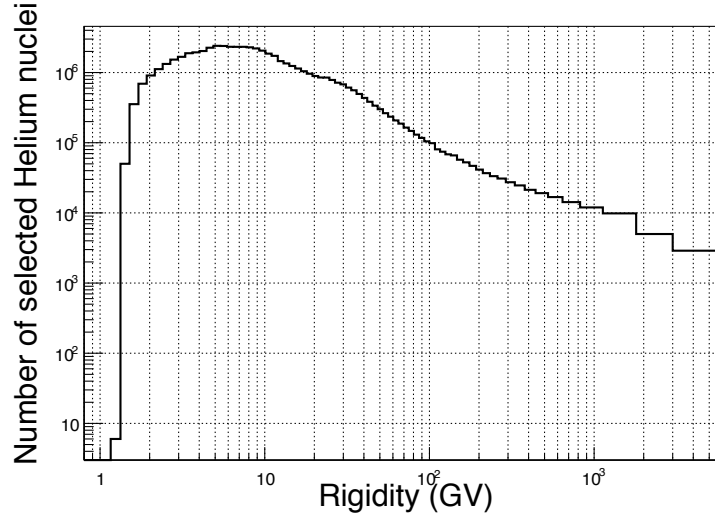


Figure 4.7 – *Distribution of the number of selected helium nuclei as a function of the rigidity for the extended data set.*

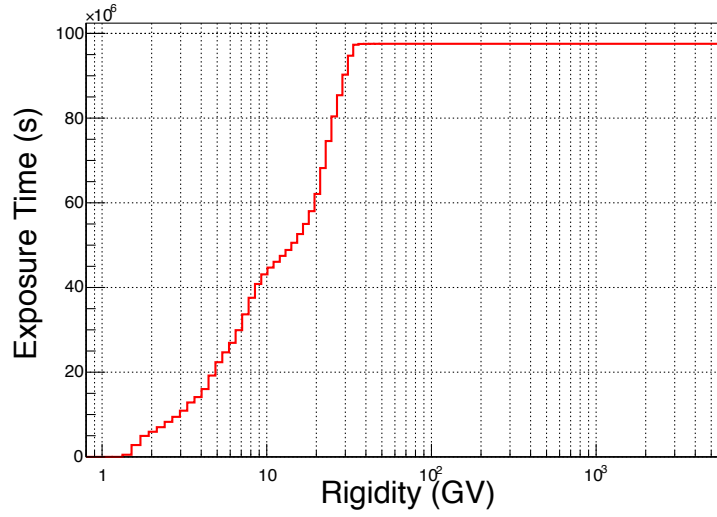


Figure 4.8 – *Exposure time for the extended data set.*

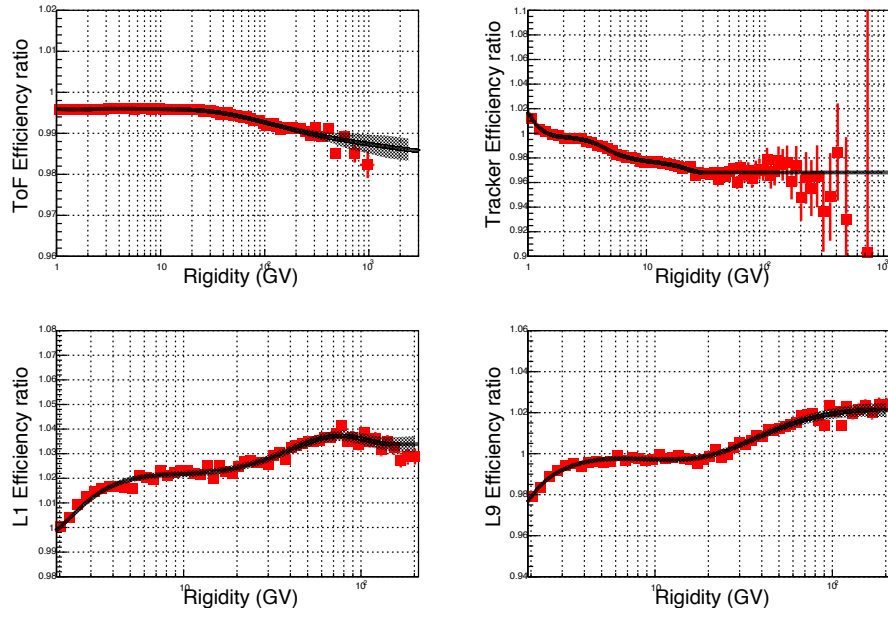


Figure 4.9 – Parametrized efficiency ratios for the ToF, the tracker, the L1 and the L9 for the extended data set.

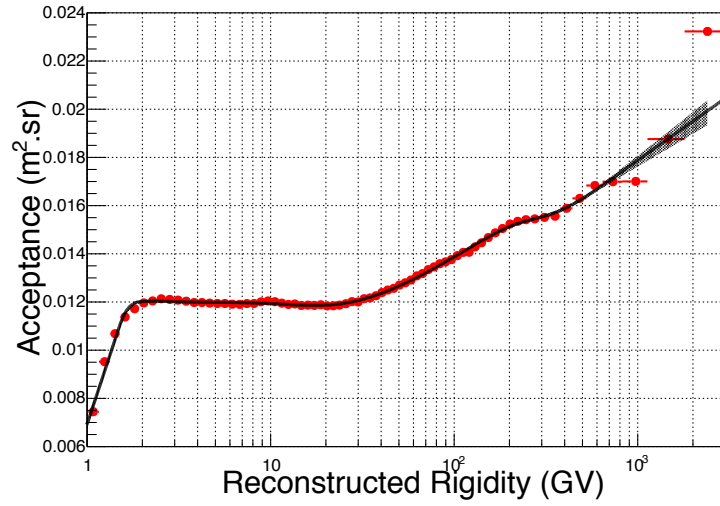


Figure 4.10 – Parametrized folded acceptance for the last iteration of unfolding procedure for the extended data set.

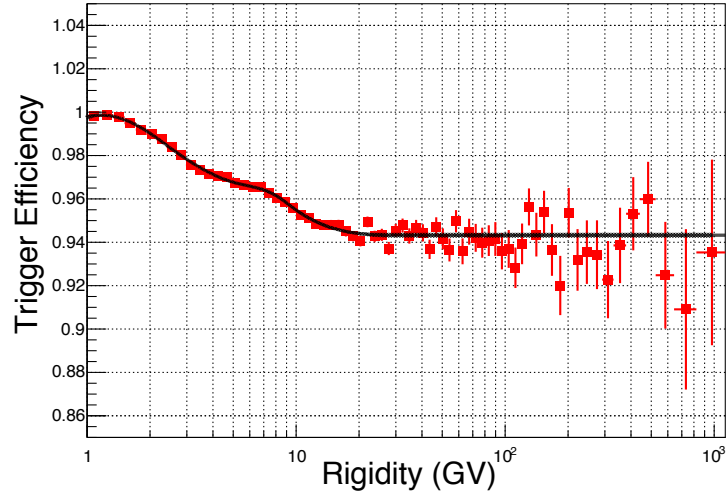


Figure 4.11 – *Parametrized trigger efficiency for the extended data set.*

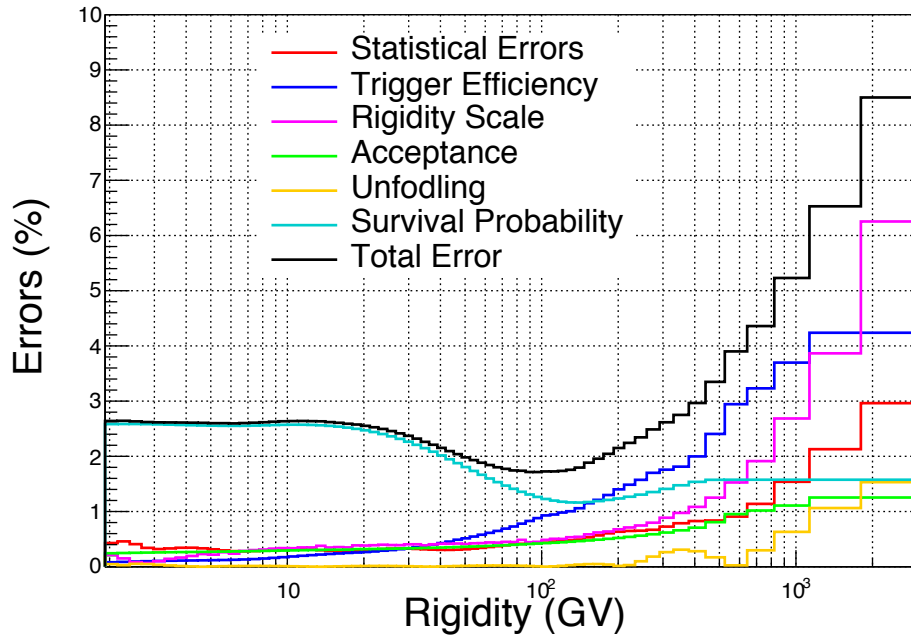


Figure 4.12 – *The statistic and systematic errors and the total errors for the extended data set.*

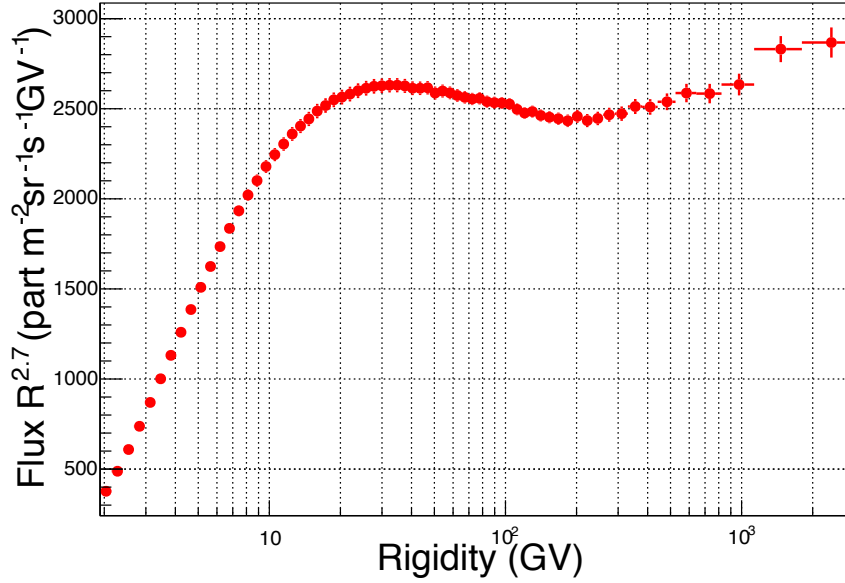


Figure 4.13 – Helium flux multiplied by a factor  $R^{2.7}$  for the extended data set.

same as the flux we produced with the restricted data set which is what we expect. To get a more detailed comparison we are going to compare this new spectrum to the collaboration published one.

#### 4.3.2 Comparison with the published results

We compare the spectrum produced with the extended range of data to the collaboration published spectrum obtained with the restricted data set. The two spectra are compared in Figure 4.14 and the ratio is also shown. The errors are compared in Figure 4.15.

We can conclude that the two results agree within 3% above 10GV. Which is, as for the previous results, enough to validate our analysis. However, we can see that at rigidity below 10GV the discrepancy between the two fluxes is higher. This effect is fully understood, it is a consequence of the solar modulation. Indeed, the solar cycle has reached its maximum in 2013 which means that since then the flow of particles coming from the Sun is decreasing with time. At low rigidity, solar activity influences the spectrum near Earth in a major way as seen in the first chapter. That explains why the average flux for the extended data set is lower than for the average flux of the collaboration publication below 15GV.

#### 4.3.3 Interpretation

Now, we are going to give few observations concerning on the last helium spectrum result. The purpose here is not to give a full interpretation of the result, theoreticians are better than us to do that, but we just want to give few explanations about what we computed and how such a result is

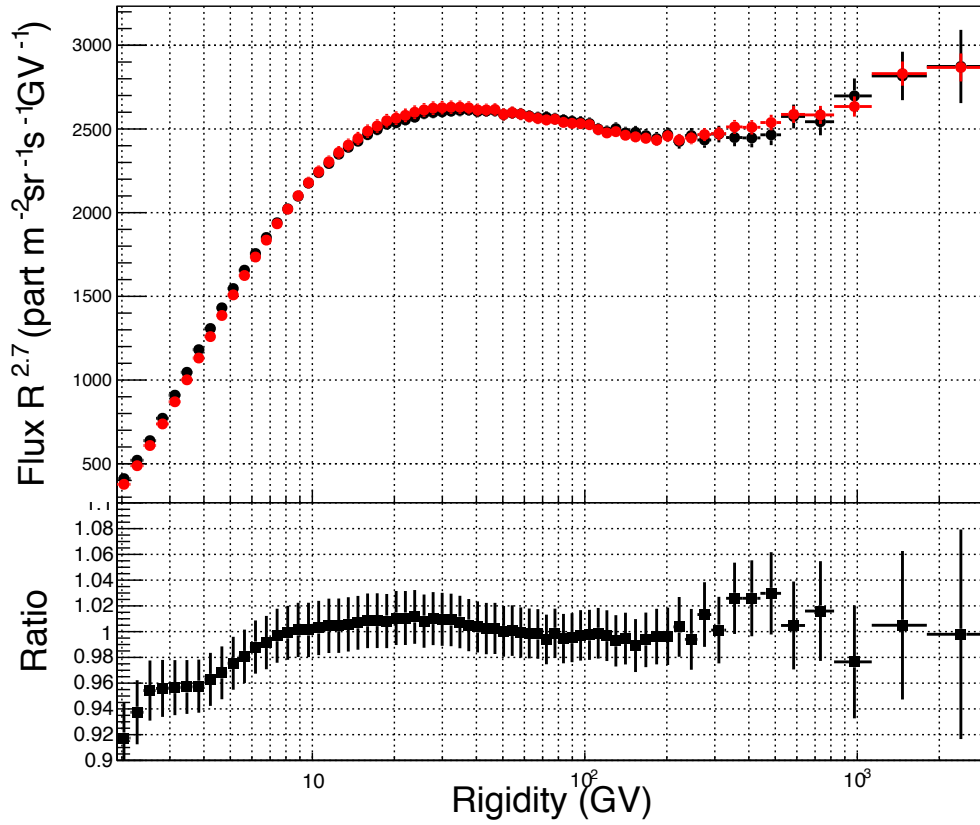


Figure 4.14 – Comparison of the helium spectra from this analysis for the extended data set (red) and from the published analysis (black) and the ratio of the two.

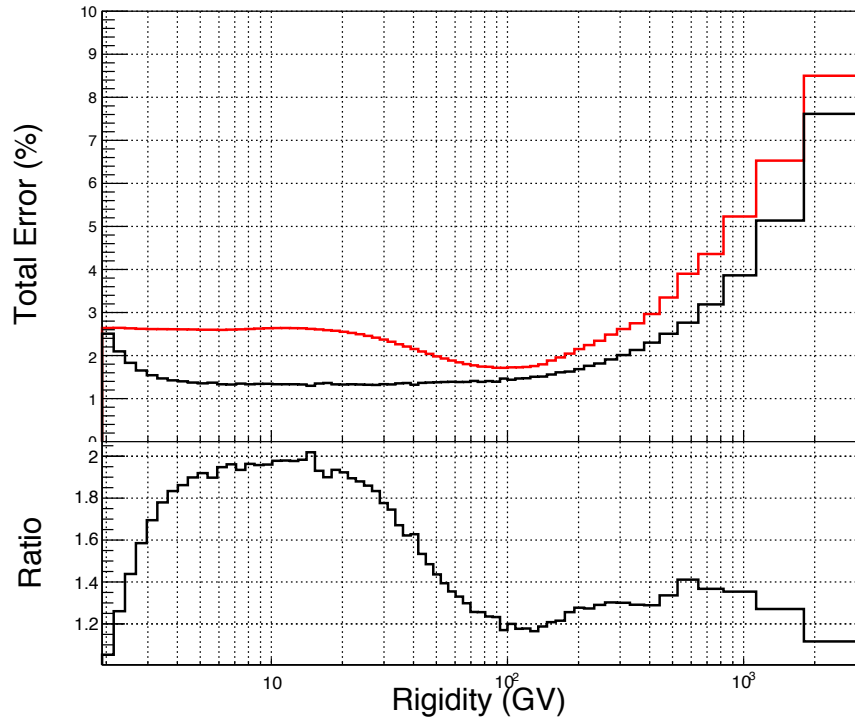


Figure 4.15 – Comparison of the total errors from this analysis for the extended data set (red) and from the published analysis (black) and the ratio of the two.

important for the study of cosmic rays.

First of all, the spectrum obtained is completely compatible with the AMS-02 collaboration published helium spectrum. In this way, we get to validate our analysis but also give support to the published results. The only discrepancy that appears at low rigidity has been understood, it comes from solar modulations. The errors we reached are low and do not exceed 9% even for the last bins which makes this spectrum very accurate. The AMS-02 experiment has achieved a precision in the helium flux measurement that no other experiment has reached until now and the time range of data taking is such that it allows us to have very small errors on the final results especially because the statistical errors do not dominate the total errors. However, despite the fact that the statistics of this measurement is 50% higher than the published sample, our results does not improve on the published one. This confirms the expectation that without major improvements in the systematics, the published results can be regarded as final.

Moreover, the increased statistics at high energies gives us the chance to see the behavior of the helium spectrum above few hundreds of GV, confirming the conclusion that there is a break in the slope. Indeed, the spectral index changes around 200GV. A single spectral index fit has been performed and is incompatible with the spectrum above 45GV at the 99.9% C.L. [1].

These results could lead to a new understanding of the production and/or the propagation of the cosmic rays and need to be put in correlation with the similar results found for the proton flux measurement [34] and the electron and positron results [33].



## Chapter 5

# A FIRST LOOK AT ANTIHELIUM

The helium spectrum gives important knowledge about the production and the propagation of the astroparticles through the Universe. But another very interesting subject can be studied as well using the same kind of analysis: the antihelium search. Antinuclei heavier than antihelium have never been observed in the past. Once the helium spectrum has been computed, we can use this analysis to search for antihelium, the same way we searched for helium nuclei since the only characteristics that differentiate them is the sign of the charge.

The purpose of this Chapter is to get a preliminary count of the antihelium candidates we can have with a simple analysis in order to compute an antihelium to helium ratio. Due to the important amount of helium nuclei we have detected, our results should be competitive with the latest published limits.

The first section will be dedicated to the actual status of the antihelium search and what has been done in the past to look for these antiparticles. We will introduce the most recent limit set for the antihelium to helium ratio. Then, we will describe the simple process followed for this work to define antihelium candidates. Finally, we will comment on the results for this analysis and the antihelium to helium ratio limit we have found.

### 5.1 Status of the Antihelium Search

It is natural to assume that the Big Bang created particles and antiparticles in equal proportion. However, 13.82 billion years later, the solar system, our galaxy as well as the cluster it belongs to, contain basically only matter and very little, if any, antimatter. The conditions for a dynamical process making antimatter disappear for the profit of matter have been formulated by Sakharov [53]. Part of these conditions go beyond today's Standard Model of particle physics. Consequently, the composition of galactic cosmic rays is completely dominated by matter particles with two notable exceptions. Antiprotons and positrons are observed in proportions which appear to be compatible with secondary production by primary cosmic rays, astrophysical processes in nearby sources or dark matter self-annihilation.

Antinuclei heavier than antiproton are almost impossible to produce in known reactions of primary cosmic rays with the interstellar medium. Any significant observation of antihelium or heavier antinucleus would thus indicate the existence of a sufficiently large antimatter bubble inside our galaxy and

demonstrate that cosmic antimatter has survived.

Several experiments have already looked for antihelium without success, but allowed to determine a upper limit on the antihelium to helium ratio. Most of these experiments where Balloon-Borne experiments except for PAMELA [54] and AMS-01 [55]. The most recent results come from the BESS-Polar balloon flights [56]. During these flights no antihelium nucleus has been found but due to a large amount of data the lowest limit has been set for the antihelium to helium ratio at rigidities up to 10GV. These results can be seen in the Figure 5.1.

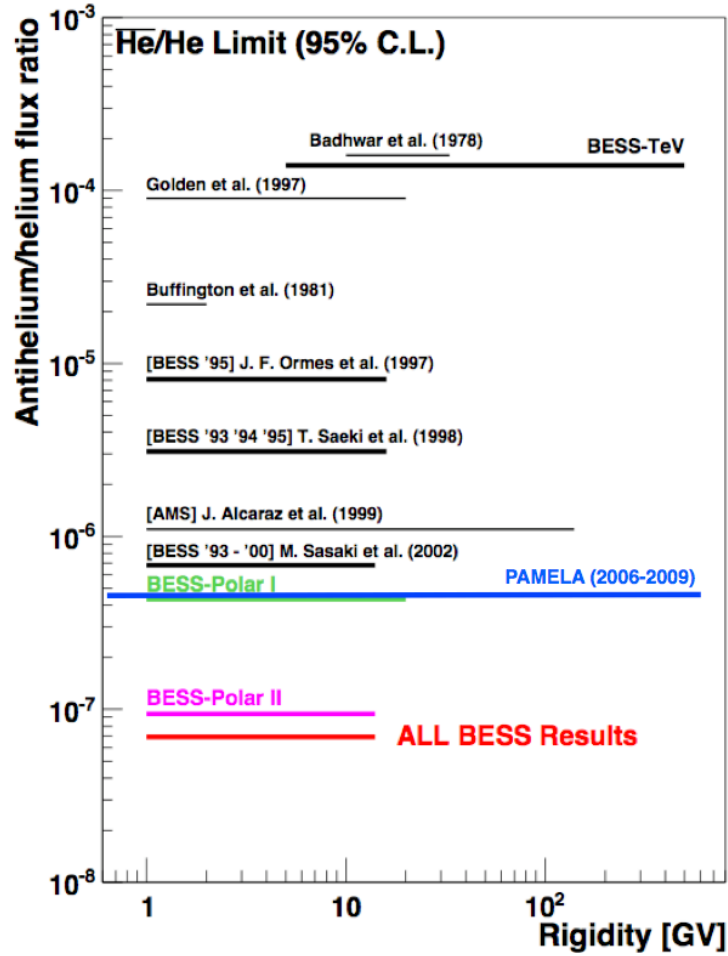


Figure 5.1 – Upper limits on the antihelium to helium ratio [56].

The most recent results have reached the lowest limit at  $0.7 \cdot 10^{-7}$  in the rigidity range from 1.6 to 14 GV by combining the two flights of BESS-Polar I and BESS-Polar II [56]. The PAMELA results set a higher limit at  $4.7 \cdot 10^{-7}$  but for a larger rigidity range from 0.6 to 600 GV [54].

## 5.2 Antihelium Analysis

The antihelium analysis is not going to be much different than the helium analysis. When analyzing particles with the AMS-02 detector the only characteristic that changes from a particle to an antiparticle is the sign of the measured rigidity. Indeed, the track of a negatively charged particle is going to bend to the opposite direction under the action of the magnetic field than the track for a positively charged particle. This explains why we perform the same analysis than for the helium but looking at negative rigidity tracks this time. Since we did not apply any restriction on the rigidity sign, we are going to use the same selection process and all the cuts described in the first section of Chapter 3 are respected. The selection of the absolute value of the particle charge remains the same as well. Once we have our selected events they can be either helium or antihelium particles. Starting from this sample for the antihelium search, we will restrict the sample further to suppress backgrounds of wrongly measured charge signs.

### 5.2.1 Inverse Rigidity Study

The best way to visualize the distribution of the rigidity without any requirement on the sign is to look at the inverse rigidity distribution. Such a distribution can be seen in the Figure 5.2. Since

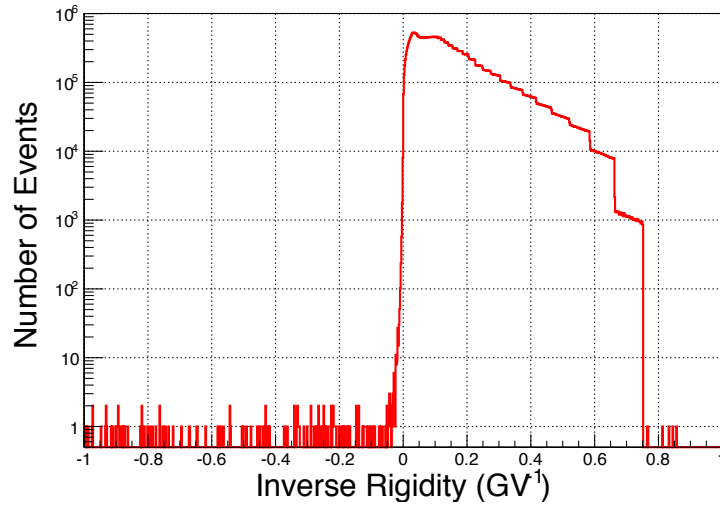


Figure 5.2 – *Distribution of the inverse rigidity.*

this is the inverse of the rigidity, the closer an event is to zero, the higher is the rigidity. What is important to notice here it is that around zero the sign of the rigidity is not reliable. Indeed, as seen previously, the MDR of a helium particle is 3.2TV for a full span pattern which means that above this value the error on the rigidity is greater than 100% so the sign cannot be trusted. For a perfectly Gaussian distribution of measured rigidities, more than 16% will have the wrong charge due to resolution. The idea here is to define a cut that will rule out all the events with rigidity resolution that is not good enough. We decided to cut all the events with  $-0.005 < \frac{1}{R} < 0.005$ . At the corresponding rigidities below 200GV, the relative rigidity resolution is below 20%. Figure 5.3 shows a zoom of the

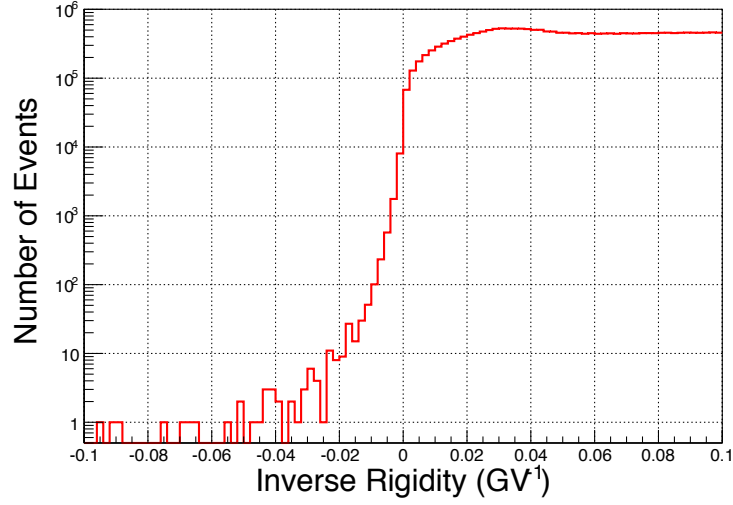


Figure 5.3 – *Distribution of the inverse rigidity zoomed near zero.*

inverse rigidity distribution near the region we are cutting. We can have now two separate samples: one for positively signed rigidity tracks we will name helium sample and the other one for negatively signed tracks we will name antihelium sample. This last one contains the antihelium candidates we are looking for but also tracks for which the charge sign is wrongly determined, e.g. due to large angle scatters or wrongly associated hits. In the helium sample we have  $5.49 \cdot 10^7$  events, in the antihelium sample 959 events.

On an other hand, the number of events in the antihelium sample is quite high. One way to be sure that this is just background is to compare with the MC. Indeed, the MC spectrum contains only helium from the beginning which means that the antihelium detected will be just background. We have compared the data and MC inverse rigidity distributions in Figure 5.4, these two distributions have been normalized for a better comparison. We can see from the Figure that the events we observed in the negative rigidity region near zero for the data are compatible with the bad reconstructed events we observe in the same region for the MC, this means we can prove that these antihelium candidates are not real candidates.

### 5.2.2 Track Quality Check

After the selection of the antihelium sample and since most of them are likely background, we need an effective way to cut these badly reconstructed events. Since the sign of the rigidity comes from the track, we cut harder on the track quality. We have already several cuts that check the track quality: there must be at least one  $Y$  side hit of the reconstructed track on each plane of the tracker (external planes included) and the fit of the track must succeed for the inner pattern as well as for the full span pattern with a  $\chi_Y^2 < 10$ .

We are going to define two new quantities that will give us more information on the quality of the track. The first quantity is the asymmetry between the inner upper half fitted track and the inner lower half fitted track. This is made possible because during the reconstruction an option of the fit

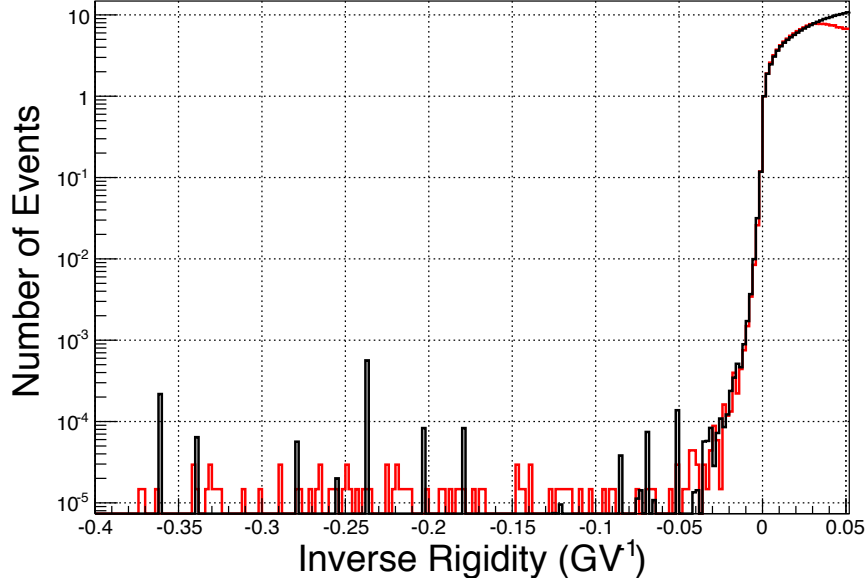


Figure 5.4 – Distribution of the normalized inverse rigidity for data sample (red) and for the MC sample (black).

corresponds to the pattern in which we want the fit to be performed, several options are possible including the two previous ones. The following Equation is used:

$$Asym_{Up,Down} = \frac{R_{Upper\ half} - R_{Lower\ half}}{R_{Upper\ half} + R_{Lower\ half}} \quad (5.1)$$

This asymmetry is represented in Figure 5.5 for both helium and antihelium samples. First, we can notice that it looks like a Gaussian distribution in the central region with high tails. The tails in the antihelium sample are much more populated, supporting the hypothesis that most of these events are mismeasured due to nuclear interactions. From the helium sample distribution we determine a cut that we apply to the antihelium sample. For that, we fit the peak of the distribution with a Gaussian as shown in Figure 5.6. The mean of the Gaussian is approximately 0 and the  $\sigma = 0.1048$ . We set the cut at  $1\sigma$  which means  $-0.1048 < Asym_{Up,Down} < 0.1048$ .

The second quantity we define is the asymmetry between the Inner+L1 fitted track and the Inner+L9 fitted track. As seen previously, such patterns are fitted during the reconstruction process. We are using the following Equation to define the asymmetry:

$$Asym_{L1,L9} = \frac{R_{Inner+L1} - R_{Inner+L9}}{R_{Inner+L1} + R_{Inner+L9}} \quad (5.2)$$

The distribution of this asymmetry for both the helium and the antihelium sample is presented in Figure 5.7. Again pronounced tails are observed for the antihelium sample. As for the previous asymmetry, we fit the peak with a Gaussian as we can see in the Figure 5.8. The mean of the Gaussian is approximately 0 and the  $\sigma = 0.0076$ . We set the cut at  $1\sigma$  which means  $-0.0076 < Asym_{L1,L9} < 0.0076$ .

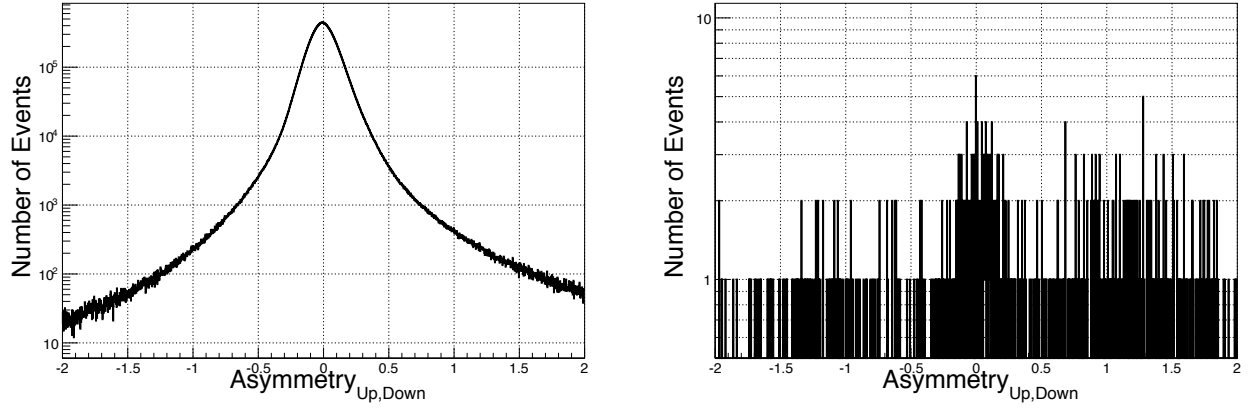


Figure 5.5 – Distribution of the asymmetry $_{Up,Down}$  for the helium sample (left) and for the antihelium sample (right).

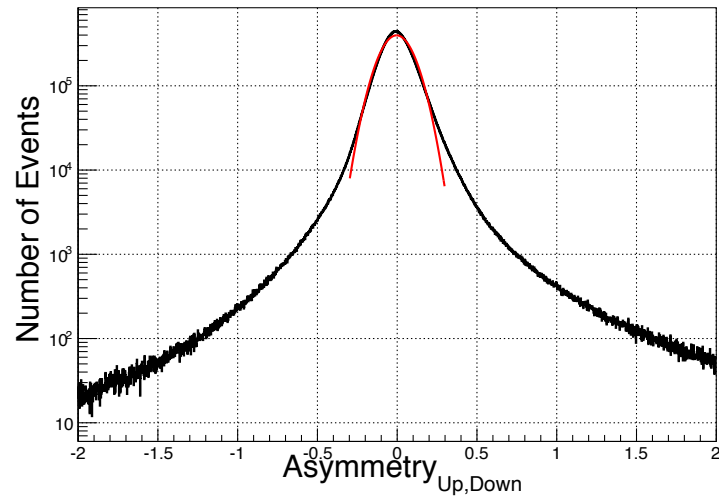


Figure 5.6 – Distribution of the asymmetry $_{Up,Down}$  for the helium sample together with the fitted Gaussian (red line) in the central part of the distribution.

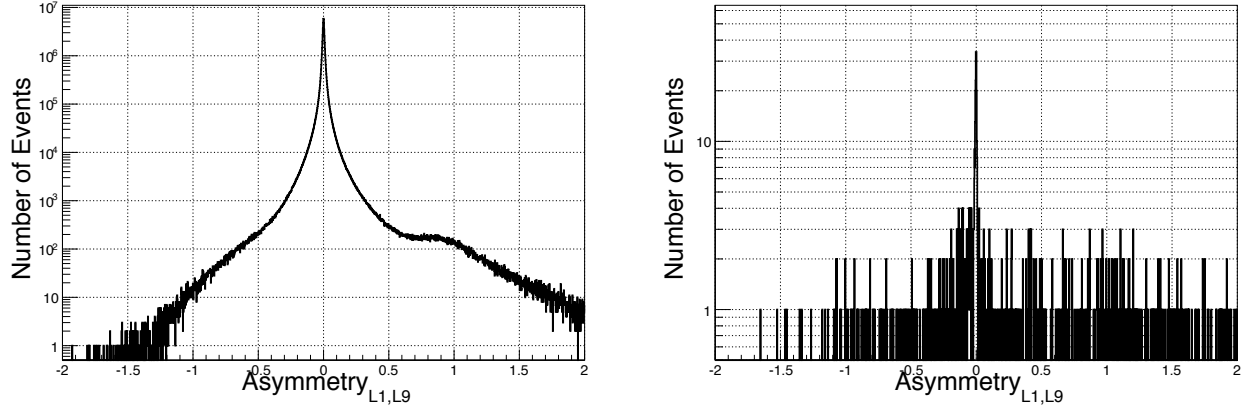


Figure 5.7 – Distribution of the  $\text{asymmetry}_{L1,L9}$  for the helium sample (left) and for the antihelium sample (right).

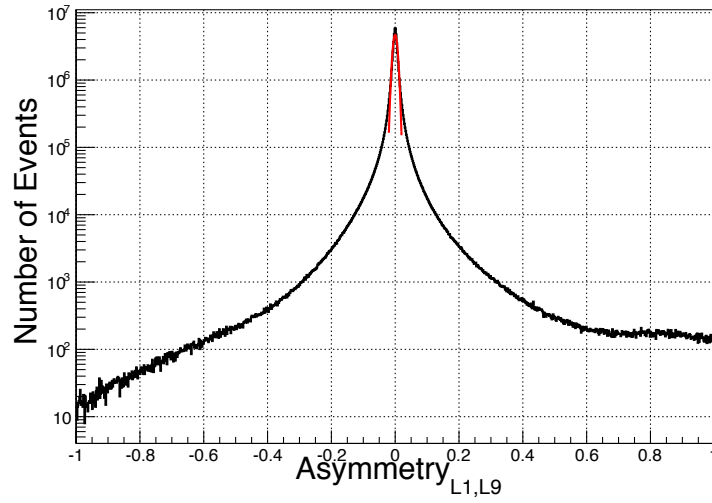


Figure 5.8 – Distribution of the  $\text{asymmetry}_{L1,L9}$  for the helium sample together with the fitted Gaussian (red line) in the central part of the distribution.

The purpose of these two asymmetry cuts is to avoid the selection of any particle that could have interacted with the material present in the detector. We also want to be sure that all the selected hits belong to the fitted track of one particle and background hits do not lead to errors on the measurement of the rigidity.

Once we have applied these two new track quality cuts we end up with 118 events in the antihelium sample and  $4.089 \cdot 10^7$  events for the helium sample.

### 5.2.3 ToF $\beta$ check

Since the ToF system is used in this analysis, we can test the compatibility of rigidity and  $\beta$ . If we look at the distribution of  $\beta$  as a function of the rigidity in Figure 5.9 we can see that

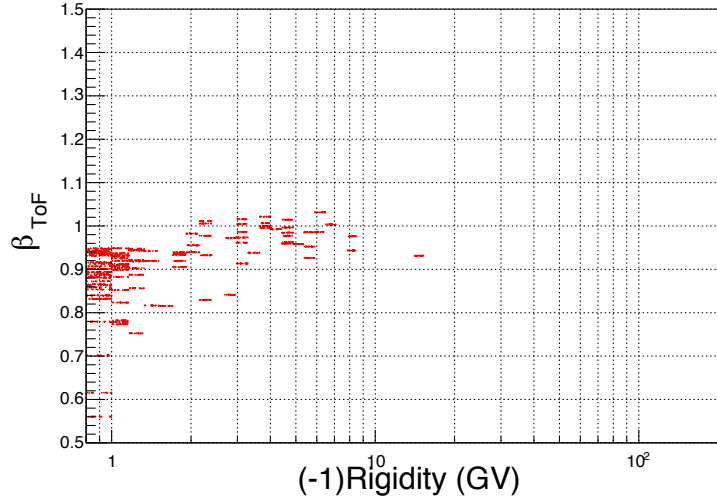


Figure 5.9 – *Distribution of the  $\beta$  with respect to the rigidity for the antihelium sample.*

some antihelium candidates appear in regions where the relation between the  $\beta$  and the rigidity is not respected, especially at very low rigidities. To cut out such candidates we define a  $\beta$ -based cut for each rigidity bins. These cuts are defined from the helium distribution of  $\beta$  as a function of the rigidity, see Figure 5.10. From this Figure we can see the relation linking the rigidity and the  $\beta$  through the Equation:

$$\beta_{ToF} = \frac{1}{\sqrt{1 + \left(\frac{m_{He}}{2 \cdot R}\right)^2}} \quad (5.3)$$

with  $m_{He} = 3.727$  GeV. The idea is to create an interval of selection around this theoretical relation. To do so, we treat each rigidity bins one by one fitting the  $\beta$  distribution with a Gaussian. The range of selection will be within  $1\sigma$ . We start from 1.51GV (bin 5) and stop at 10.1GV (bin 23). Before bin 5 we are cutting all the events. After bin 23 we are keeping all the events because the relation becomes flat. For the other bins we are fitting the  $\beta$  distribution with a Gaussian, examples for bins 5, 10, 15 and 23 are shown in Figure 5.11. Once we have performed the fit, we define the selection range at  $1\sigma$ . The results of these fit are presented in Table 5.1.



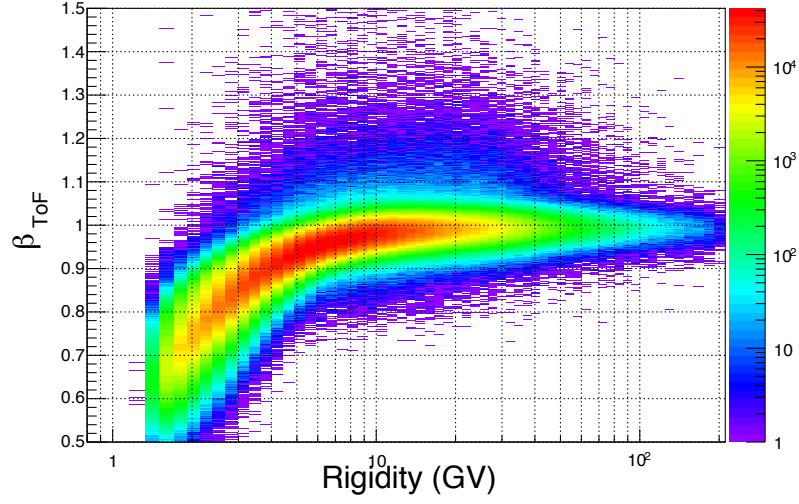


Figure 5.10 – *Distribution of the  $\beta$  with respect to the rigidity for the helium sample.*

BIN NUMBER	Rigidity Range (GV)	MEAN	$\sigma$
5	1.51 - 1.71	0.678	0.052
6	1.71 - 1.92	0.716	0.049
7	1.92 - 2.15	0.750	0.044
8	2.15 - 2.4	0.782	0.041
9	2.4 - 2.67	0.812	0.038
10	2.67 - 2.97	0.838	0.037
11	2.97 - 3.29	0.861	0.033
12	3.29 - 3.64	0.882	0.030
13	3.64 - 4.02	0.899	0.028
14	4.02 - 4.43	0.914	0.026
15	4.43 - 4.88	0.927	0.024
16	4.88 - 5.37	0.938	0.022
17	5.37 - 5.9	0.947	0.021
18	5.9 - 6.47	0.955	0.021
19	6.47 - 7.09	0.961	0.020
20	7.09 - 7.76	0.967	0.020
21	7.76 - 8.48	0.971	0.019
22	8.48 - 9.26	0.975	0.019
23	9.26 - 10.1	0.978	0.019

Table 5.1 – *Results of the fitted  $\beta$  distributions for bin 5 to bin 23.*

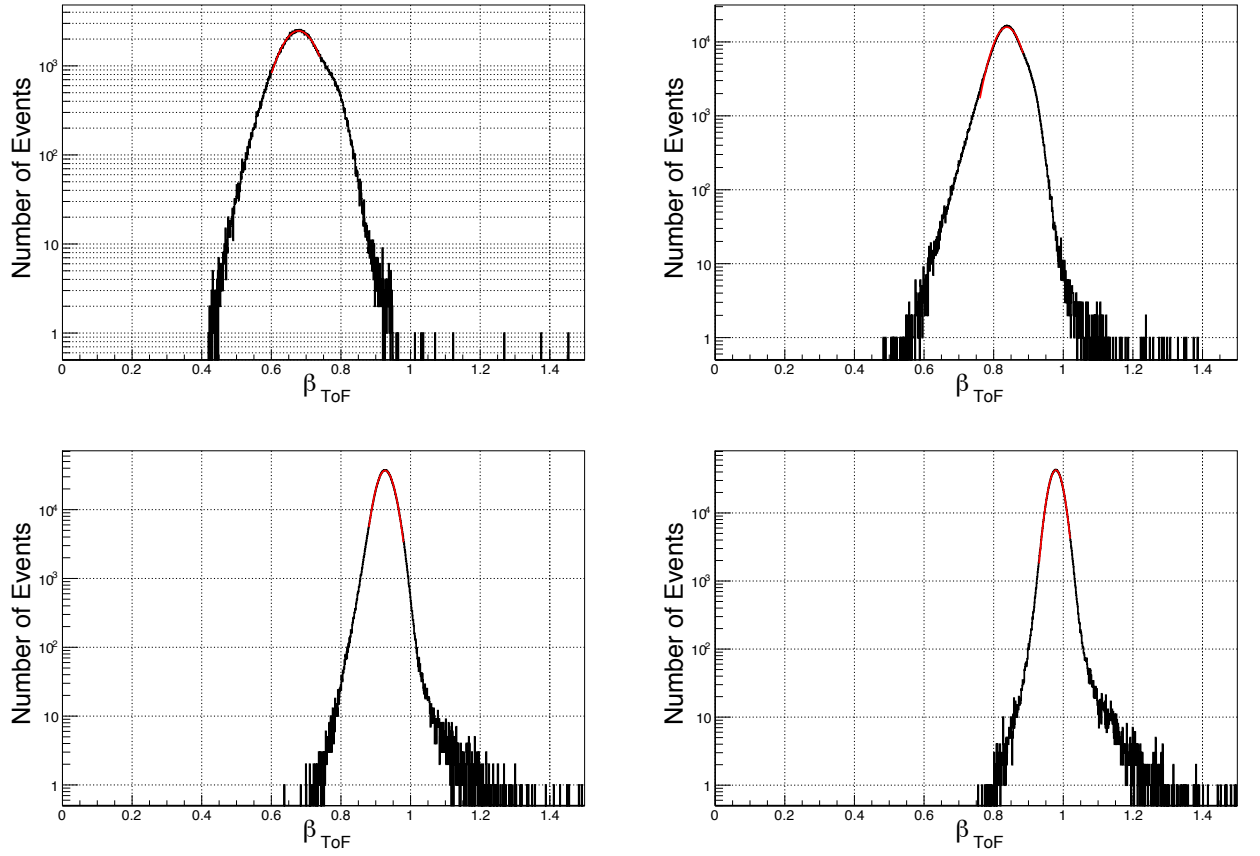


Figure 5.11 – Distribution of the  $\beta$  for the helium sample for the rigidity bin 5 (upper left), 10 (upper right), 15 (lower left) and 23 (lower right) .

The antihelium candidates selected after this process are presented in the Figure 5.12, we end up with

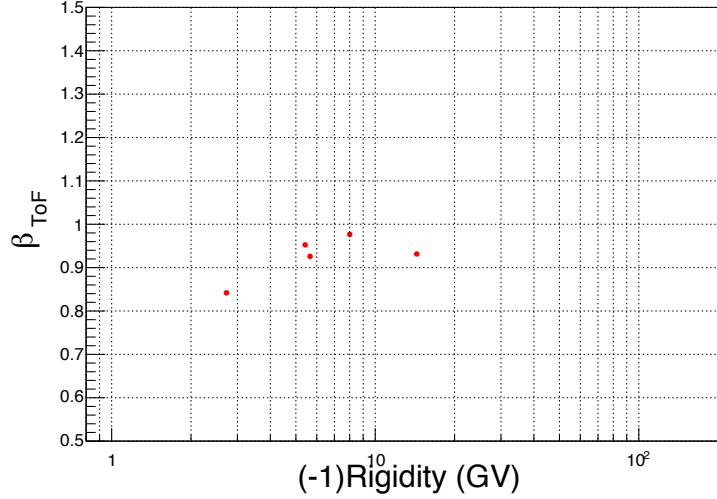


Figure 5.12 – Distribution of the  $\beta$  with respect to the rigidity for the last candidates of the antihelium sample.

5 candidates and  $2.857 \cdot 10^7$  events in the helium sample.

We can now take a look at these five candidates in details. To do so, we are using the event display that shows us how the reconstructed events look like and can potentially highlight some bad reconstruction or interactions in the detector. After looking at the display, we can already eliminate three of them because we can clearly see interactions inside the detector, their displays are shown in Figure 5.13. This finding support the assumption that the remaining events are dominated by background. For the two left candidates no signs of interaction are observed. However, the one shown in Figure 5.14 has no signal in the RICH detector. In the other one, shown in Figure 5.15, the particle misses the ECAL. This means that both events miss redundant information and are consistant with background. The first candidate, which display can be seen in Figure 5.14, has a rigidity of  $-2.756$  GV, a  $\beta$  from the ToF of 0.841, a total deposited energy in the ECAL of 915.02 MeV but no RICH event even if the track crosses this subdetector. The second candidate, which display can be seen in Figure 5.15, has a rigidity of  $-5.533$  GV, a  $\beta$  from the ToF of 0.927, a  $\beta$  from the RICH of 0.967 but there is no ECAL event since the track does not cross its fiducial volume. For both of these candidates the charge is compatible with  $Z = 2$  for the TRD, the four layers of the ToF separately and the nine layers of the tracker separately. We can also notice that both of these events show a very clean reconstructed track.

### 5.3 Antihelium Results

The purpose of this analysis on antihelium candidates is to define a limit on the antihelium to helium ratio conservatively assuming that those remaining candidates are due to background. In order to get a fair comparison between the helium and the antihelium samples and to compute the right ratio, we are going to apply the exact same cuts we previously performed on the antihelium

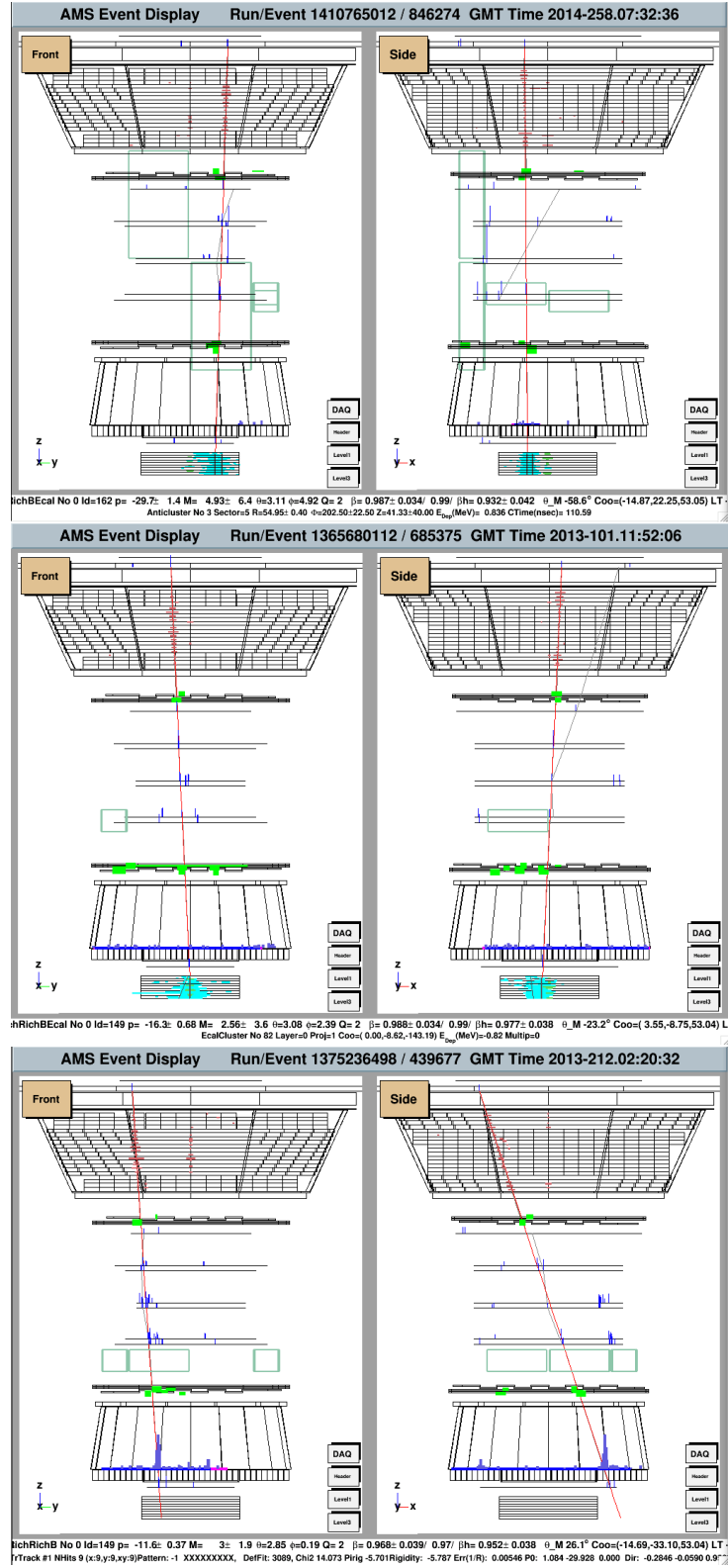


Figure 5.13 – Display of the three eliminated events due to interactions in the detector.

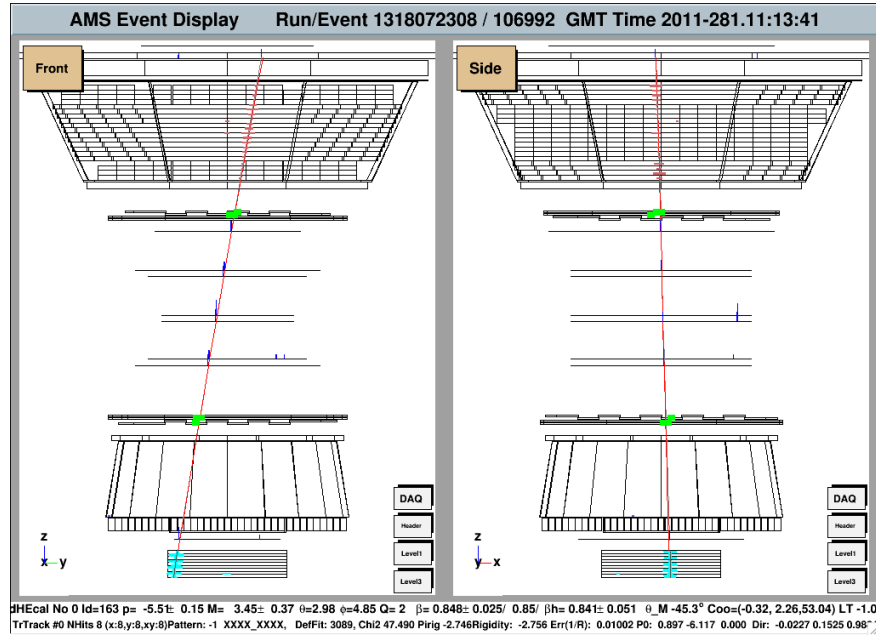


Figure 5.14 – Display of the first antihelium candidate.

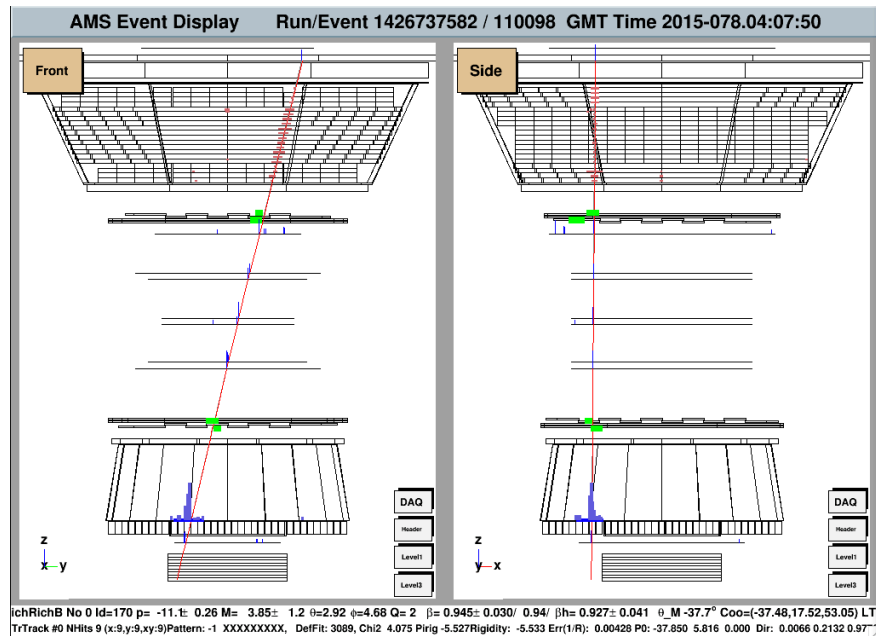


Figure 5.15 – Display of the second antihelium candidate.

candidates, to the helium sample.

After the track quality cuts, the helium sample contains  $4.089 \cdot 10^7$  nuclei. Once we apply the cut on the ToF  $\beta$ , the number of selected helium is  $2.857 \cdot 10^7$ . We use the following Equation:

$$\overline{He}/He < \frac{N_{\overline{He}} + \epsilon_{N_{\overline{He}}}}{N_{He}} \quad (5.4)$$

with  $N_{\overline{He}} + \epsilon_{N_{\overline{He}}} = 6.30$  at a 95% C.L. [57]. The computed upper limit on the antihelium to helium ratio is thus  $2.21 \cdot 10^{-7}$  at a 95% C.L. for a rigidity range from 1.7 GV to 200 GV. Quoting a global limit assumes that the spectral shape of a hypothetical antihelium flux would be the same as the one of helium. To go beyond this upper limit and to determine if the remaining two candidates correspond to a valid antihelium would require a careful inspection of each event as well as further statistical and systematic tests. They go beyond the scope of this thesis.

The final result presented in this work is competitive to what has been found in the recent past as we can see in Figure 5.16. Indeed, the lowest limit on the antihelium to helium ratio has been found at  $0.7 \cdot 10^{-7}$  from the BESS-Polar combined data. However, the result we should compare our result with is the antihelium to helium ratio from PAMELA because the rigidity ranges correspond. PAMELA gives a ratio of  $4.7 \cdot 10^{-7}$  which we were able to improve with this analysis.

The results presented here are just preliminary and a more advanced study can be performed. To do so, we would have to check more precisely the characteristics of each candidate in order to find criteria that would correspond or not to a true antihelium nucleus. The AMS collaboration continues and refines this search and extends it to heavier nuclei.

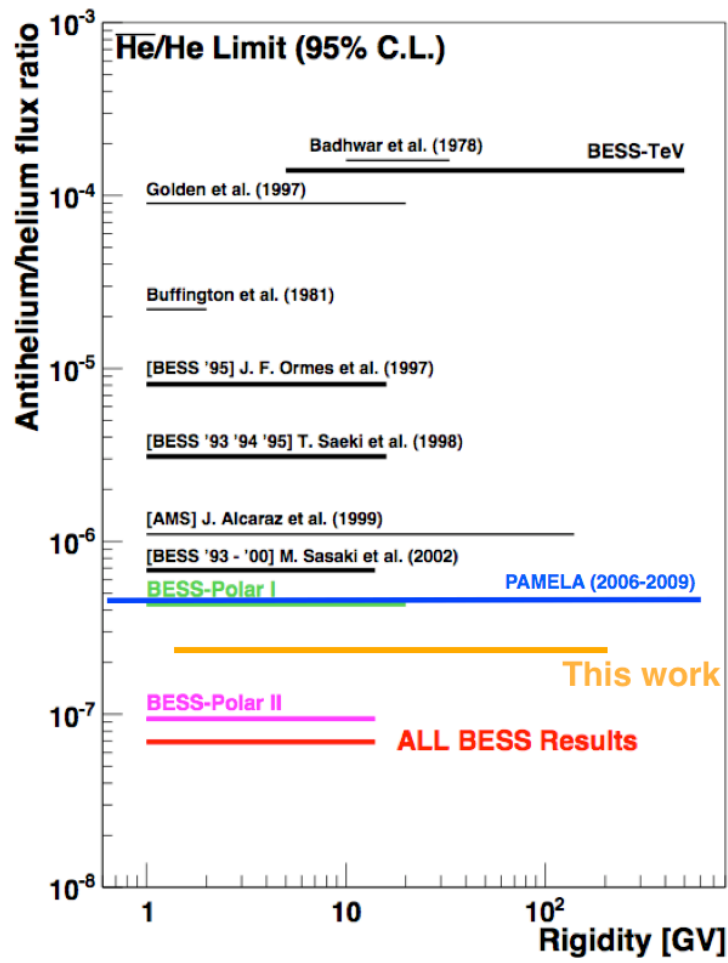


Figure 5.16 – Limits on the antihelium to helium ratio with the result from this work [56].





# CONCLUSION

Through this work, we presented two results: the helium spectrum and a conservative upper limit on the antihelium/helium ratio. Both of them provide important knowledge on cosmic rays. Indeed, the obtained precision in the helium spectrum allow to gain more information about the cosmic ray propagation through the spectral index and the change in the slope around 200 GV. The upper limit on the antihelium/helium ratio is the first step in the search of antihelium.

The main purpose of this work was to compute the helium flux. First for the same data set as the publication result, then, for an extended data set that adds more than 50% to the restricted data set statistic. The comparison of the first result with the published one allowed to validate our analysis, the discrepancy between the two being less than 2.5% over the whole rigidity range and fully compatible with systematic differences in the analysis. The comparison between the extended data set result and the published result shows a discrepancy lower than 3% above 10 GV. For what concerns the low rigidity part, the increasing discrepancy with decreasing rigidity is understood as solar modulation effects. The total errors are not significantly different from the previous results which leads us to conclude that the result on the helium flux can only be improved by reducing the systematic errors not by increasing the statistics.

The second purpose of this work was a preliminary search for antihelium nuclei. We computed the antihelium/helium ratio and found an upper limit at  $2.21 \cdot 10^{-7}$  at a 95% C.L. for a rigidity range from 1.7 GV to 200 GV. This result improves the previous result from PAMELA which was the lowest limit extending on a rigidity range above 10 GV. We ended up with two antihelium candidates. The next step in the antihelium search beyond this simple analysis would be to study these candidates in more details to see if one of them persists as a good antihelium nucleus.

The future of helium study with AMS-02 would be an improvement in the systematic understanding, which is the only way to reduce the errors above 100 GV. For what concerns antihelium, an increase in the statistics will allow to reduce the antihelium/helium ratio limit or to discover an antihelium nucleus, which is one of the main goals of the experiment. In any case, the next few years are going to be decisive for the antihelium search with AMS-02.



# Bibliography

- [1] M. Aguilar et al. Precision measurement of the helium flux in primary cosmic rays from rigidity 1.9 gv to 3 tv with the alpha magnetic spectrometer on the international space station. *Phys. Rev Lett.*, 115:211101, 2015.
- [2] V.F. Hess. Über beobachtungen der durchdringenden strahlung bei sieben freiballonfahrten. *Physik. Zeitschr.*, 13:1084–1091, 1912.
- [3] W. Kohlhörster. *Physik. Zeitschr.*, 14:1153, 1913.
- [4] P. Carlson and A. De Angelis. Nationalism and internationalism in science: the case of the discovery of cosmic rays. *Eur. Phys. J.*, 35:309–329, 2010.
- [5] J. Clay P.M. Van Alphen and C.G.T Hooft. Results of the dutch cosmic ray expedition 1933. *Physica*, 1:829–838, 1934.
- [6] C. Störmer. Twenty-five years’ work on the polar aurora. *Terrestrial Magnetism and Atmospheric Electricity*, 35:193–208, 1930.
- [7] E. Fermi. On the origin of the cosmic radiation. *Phys. Rev.*, 75:1169–1174, 1949.
- [8] S.H. Neddermeyer and C.D. Anderson. Note on the nature of cosmic-ray particles. *Phys. Rev.*, 51:884–886, 1937.
- [9] C. Lattes H. Muirhead G. Occhialini and C. Powell. Process involving charges mesons. *Nature*, 159:694–1174, 1947.
- [10] R.L. Golden et al. Evidence for the existence of cosmic-ray antiprotons. *Phys. Rev. Lett.*, 43:1196–1199, 1979.
- [11] W.D. Apel et al. Ankle-like feature in the energy spectrum of light elements of cosmic rays observed with kascade-grande. *Phys. Rev. D*, 87:081–101, 2013.
- [12] K. Greisen. End to the cosmic-ray spectrum? *Phys. Rev. Lett.*, 16:748–750, 1966.
- [13] G. Zatsepin and V. Kuz’min. Upper limit of the spectrum of cosmic rays. *Soviet Journal of Experimental and Theoretical Physics Letters*, 4:78, 1966.
- [14] M.S Potgieter. Solar modulation of cosmic rays. *Living Rev. Solar Phys.*, 10:3, 2013.
- [15] E.W. Cliver. History of research on solar energetic particle (sep) events: the evolving paradigm. *Universal Heliophysical Process Proceedings IAU Symposium*, 257:401–412, 2008.
- [16] P.Biasi. The origin of galactic cosmic rays. *Astro. Astrophys. Rev.*, 21:70, 2013.
- [17] E. Fermi. Galactic magnetic fields and the origin of cosmic radiation. *The Astrophysical Journal*, 119:1–6, 1954.
- [18] T. Wibig and A.W. Wolfendale. At what particle energy do extragalactic cosmic rays start to predominate? *J.Phys.*, G31:255–264, 2005.

- [19] J. Abraham et al. Measurement of the energy spectrum of cosmic rays above  $10^{18}$ ev using the pierre auger observatory. *Phys. Lett. B*, 685:239–246, 2010.
- [20] P. Sokolsky for the HiRes Collaboration. Final results from the high resolution fly’s eye (hires) experiment. *XVI International Symposium on Very High Energy Cosmic Ray Interactions*, 2010.
- [21] N.Nakamura and al. Particle data group. *Review of Particle Physics*, 2014.
- [22] K. Yoshimura et al. The second antarctic flight of bess-polar experiment: Flight summary and detector performance. *Proceedings of the 31<sup>st</sup> ICRC*, 2009.
- [23] <https://www.mpi-hd.mpg.de/hfm/HESS/>.
- [24] <https://www.auger.org>.
- [25] Abbasi et al. Study of ultra-high energy cosmic ray composition using the high resolution fly’s eye. *Astroparticle Physics*, 64:49–62, 2015.
- [26] Menn et al. The pamela space experiment. *Advances in Space Research*, 51:209–218, 2013.
- [27] Adriani et al. Pamela measurements of cosmic-ray proton and helium spectra. *Science*, 332:69–72, 2011.
- [28] S. Ting. The alpha magnetic spectrometer on the international space station. *Nuclear Physics B*, 243-244:12–24, 2013.
- [29] <http://dpnc.unige.ch/dampe/>.
- [30] D.F Smart and M.A. Shea. A review of geomagnetic cutoff rigidities for earth-orbiting spacecraft. *Advances in Space Research*, 36:2012–2020, 2005.
- [31] International Association of Geomagnetism and Aeronomy. International geomagnetic reference field: the eleventh generation. *Geophys. J. Int.*, 183:1216–1230, 2010.
- [32] J.R Heitzler. The future of the south atlantic anomaly and implications for radiation damage in space. *Journal os Atmospheric and Solar-Terrestrial Physics*, 64:1701–1808, 2002.
- [33] M. Aguilar et al. Electron and positron fluxes in primary cosmic rays measured with the alpha magnetic spectrometer on the international space station. *Phys. Rev. Lett*, 113:121102, 2014.
- [34] M. Aguilar et al. Precision measurement of the proton flux in primary cosmic rays from rigidity 1 gv to 1.8 tv with the alpha magnetic spectrometer on the international space station. *Phys. Rev. Lett.*, 114:171103, 2015.
- [35] M. Aguilar et al. The alpha magnetic spectrometer (ams) on the international space station: Part 1 results from the test flight on the space shuttle. *Physics Reports*, 366:331 – 405, 2002.
- [36] M. Aguilar et al. Relative composition and energy spectra of light nuclei in cosmic rays: results from ams-01. *Astrophysical Journal*, 724:329–340, 2010.
- [37] M. Capell, E. Cortina, and AMS-02 Collaboration. AMS-02 Electronics. In *International Cosmic Ray Conference*, volume 4 of *International Cosmic Ray Conference*, page 2173, July 2003.
- [38] <http://www.ams02.org>.
- [39] Th. Kirn and Th. Siedenburger. The ams-02 transition radiation detector. *Nucl. Instr. and Meth. in Physics Research A*, 535:165–170, 2004.
- [40] D. Casadei et al. The ams-02 time of flight system. *Nuclear Physics B*, 113:133–138, 2002.
- [41] V. Bindi et al. Calibration and performance of the ams-02 time of flight detector in space. *Nuclear Instruments and Methods in Physics Research A*, 743:22–29, 2014.

- [42] G. Ambrosi et al. Ams-02 track reconstruction and rigidity measurement. *33<sup>rd</sup> ICRC, Rio de Janeiro 2013*, 2013.
- [43] P. Saouter. *Nuclei Identification with the AMS-02 Silicon Tracker and Measurement of Cosmic Ray Nuclei Fluxes*. PhD thesis, Université de Genève, 2014.
- [44] J. van Es et al. Ams-02 tracker thermal control system (ttcs) design, model and breadboard results. *SAE Technical Paper*, 2004.
- [45] G. Ambrosi et al. Alignment of the ams-02 silicon tracker. *33<sup>rd</sup> ICRC, Rio de Janeiro 2013*, 2013.
- [46] T. Bruch and W. Wallraff. The anti-coincidence counter shield of the ams tracker. *Nucl. Inst. and Methods in Physics Research A*, 572:505–507, 2007.
- [47] [http://dpnc.unige.ch/ams/ams\\_beta/Welcome\\_New.shtml](http://dpnc.unige.ch/ams/ams_beta/Welcome_New.shtml).
- [48] M. Aguilar-Benitez et al. In-beam aerogel light yield characterization for the ams rich detector. *Nucl. Inst. and Methods in Physics Research A*, 614:237–249, 2010.
- [49] R. Pereira on the behalf of the AMS RICH collaboration. The ams-02 rich detector: Performance during ground-based data taking at cern. *Nucl. Inst. and Methods in Physics Research A*, 639:37–41, 2011.
- [50] F. Cadoux et al. The ams-02 electromagnetic calorimeter. *Nuclear Physics B*, 113:159–165, 2002.
- [51] C. Lin. Trigger logic design specification. *Internal Note*, 2005.
- [52] <https://geant4.web.cern.ch/geant4/>.
- [53] A.D. Sakharov. Violation of cp invariance, c asymetry, and baryon asymmetry of the universe. *JETP Lett.*, 5:24–27, 1967.
- [54] A.G. Mayorov et al. Upper limit on the antihelium flux in primary cosmic rays. *JATP Lett.*, 93:628–631, 2011.
- [55] J. Alcaraz et al. Search for antihelium in cosmic rays. *Physics Letters B*, 461:387–396, 1999.
- [56] K. Abe et al. Search for antihelium with the bess-polar spectrometer. *Phys. Rev. Lett.*, 108:131301, 2012.
- [57] <http://pdg.lbl.gov>.